UNIVERSITY OF UDINE - ITALY

Department of Physics

Ph.D. Thesis

MAGIC γ-RAY OBSERVATIONS OF DISTANT AGN AND A STUDY OF SOURCE VARIABILITY AND THE EXTRAGALACTIC BACKGROUND LIGHT USING $FERMI$ AND AIR CHERENKOV TELESCOPES

Supervisor:

Prof. ALESSANDRO DE ANGELIS

Co-supervisors:

Dr. MASSIMO PERSIC

Dr. BARBARA DE LOTTO

Dr. FABRIZIO TAVECCHIO

Candidate:

NIJIL MANKUZHIYIL

Doctorate of Philosophy in Mathematics and Physics

XXII cycle AY 2009/2010

Outline

MAGIC is a telescope devoted to the detection of gamma-rays of astrophysical origin in the energy region above 30 GeV (Very-High-Energy). It is located at the Observatory of Roque de Los Muchachos, in the Canary Island of La Palma.

During my thesis I worked for a period of three and a half years within MAGIC. I mostly contributed along three lines:

1. Data taking shifts. I spent four periods of 28 days each at the observatory taking data acquisition shifts; since the last period I have been shift leader.

2. Software for the experiment. In particular I am responsible of the analysis software for the automatic check of the quality of data.

3. Physics analysis. In particular my contribution was devoted to the study of Active Galactic Nuclei. Most of my thesis (apart from a section dedicated to the software for data analysis, point 2.) is devoted to this.

Active Galactic Nuclei (AGN) are considered to be sources of the highest-energy cosmic rays. It is believed that AGN are supermassive black holes (with mass in the range of 10^6 to $10^9\,M_\odot$) in the core of galaxies, and the radiated power is produced by mass accretion. Some AGN display relativistic outflows (jets), which are considered to be the site of particle acceleration and generate high energy photons. If a relativistic jet is viewed at a small angle relative to its axis the observed emission from the jet is amplified by the relativistic beaming effect; such sources are called blazars, and they are the dominant class of high-energy photon emitters among the observed AGN in γ-ray astronomy. In 1992, TeV emission was discovered from a blazar, Mkn421, which was established as the first extra-galactic TeV photon emitter. Electromagnetic emission from this class of sources can be observed from radio up to TeV energies.

The signal of γ-rays emitted by AGN in the TeV region is attenuated by photon-photon interactions during the journey from the sources of emission to the Earth. The energy of the background photons relevant for the absorption lies in the optical-near infrared band, and it is called the Extragalactic Background Light (EBL). Such an attenuation increases with the energy of the emitted γ-rays and with the distance of the source.

An outlook of this thesis follows.

In Chapter 1 I give a brief introduction on cosmic rays. I discuss γ-ray astrophysics at very-high energy, introducing the possible sources of emission.

In Chapter 2 I discuss blazars, and their different classes. I investigate the physics involved in the photon emission by blazars.

In Chapter 3 I give a brief introduction on the Cherenkov imaging technique and I introduce the MAGIC telescope.

In Chapter 4 the analysis techniques of the data from Cherenkov telescopes (MAGIC in particular) are described.

In Chapter 5 I describe the analysis and interpretation of the data from the blazar 3C 454.3, which is one of the farthest sources observed by MAGIC. Even though we just obtained an upper limit on the emission flux, this can constrain theoretical models. Part of this work has been published as an article by MAGIC.

In Chapter 6 the analysis and interpretation of multiwavelength observations of the AGN PG 1553+113 by MAGIC, AGILE and by various X-rays and optical instruments is described. This has been the first ever broadband (from the X-ray band to the TeV region) campaign on blazars; I have been the principal investigator for this analysis, from which an article has been published by MAGIC.

In Chapter 7 I investigate the relation between SSC parameters and the variability of sources. I choose objects which underwent more than one simultaneous multiwavelength campaign: Mkn 421, Mkn 501 and PKS 2155-304. The results will be part of the upcoming article co-authored with S. Ansoldi, M. Persic and F. Tavecchio.

In Chapter 8 I propose a novel method to measure the EBL density using simultaneous multiwavelength observations of blazars. As a case study I choose the AGN PKS 2155-304 at a redshift $z = 0.12$, and I model the attenuation for this source. A phenomenological article co-authored with M. Persic and F. Tavecchio has been taken from this work.

Acknowledgments

To start with, I would like to thank Prof. Alessandro De Angelis for offering me the opportunity to work on this thesis and introducing me the MAGIC sky of γ-rays. This work would not have been possible without his constant support and advice.

I express my immense gratitude to Dr. Massimo Persic for his guidance, discussions, patience and the positive energy that he provided during my student life in Udine and making it a memorable experience.

I would like to express my sincere gratitude to Dr. Barbara De Lotto for a lot of useful suggestions and discussions, and for the homely environment at work.

Many thanks to Dr. Fabrizio Tavecchio for his guidance and the hospitality at Brera observatory.

I would like to thank Dr. Stefano Ansoldi for all the help, especially for introducing me to this wonderful group.

I would like to acknowledge all my teachers, especially Dr. Ravi Menon who introduced me the fun of doing Physics.

Thanks to the young group in Udine, Vincenzo Vitale, Oriana Mansutti, Valeria Scapin, Luigi Cossio and Gessica De Caneva for the beautiful time.

Many thanks to Antonio Stamerra, Elena Pian, Daniela Dorner, Elisa Prandini, Igor Oya and Jose Luis Contreas for the collaboration works from which I learned a lot.

I would like to acknowledge the MAGIC collaboration, especially Prof. Masahiro Teshima, Oscar Blanch, Juan Cortina, Abelardo Morelajo, Daniel Mazin, Thomas Schweizer, Pratik Majumdar, Karsten Berger and Markus Garczarczyk for useful exchanges, and Konstancja Satalecka for a wonderful time during my first MAGIC shift.

Last but not the least, I would like to thank my parents and friends for their love and support.

Contents

1 Very High Energy γ-ray Astrophysics **1**

1.1 General Introduction . . . 1

1.2 Cosmic rays . . . 3

1.3 Neutrinos . . . 5

1.4 Photons . . . 7

1.4.1 Radio . . . 8

1.4.2 Infrared (IR) . . . 9

1.4.3 Optical . . . 10

1.4.4 Ultraviolet (UV) . . . 10

1.4.5 X-ray . . . 10

1.5 γ-ray Astronomy . . . 11

1.5.1 HE γ-ray . . . 11

1.5.2 VHE γ-ray . . . 13

1.6 VHE γ-ray sources . . . 13

1.6.1 Galactic sources . . . 14

1.6.2 Extra Galactic Sources . . . 16

2 Active Galactic Nuclei **19**

2.1 Introduction . . . 19

2.2 Classification of AGN . . . 20

2.3 Unification of AGN . . . 22

2.4 Blazar . . . 25

2.5 Emission mechanisms . . . 26

2.5.1 Thermal emission . . . 26

2.5.2 Non-thermal emission . . . 29

2.6 Models . . . 32

2.7 SSC model . . . 35
2.8 Summary of observed AGN in VHE range . . . 38

3 The MAGIC Telescope 41
3.1 Introduction . . . 41
3.2 Extended Atmospheric Showers (EAS) . . . 41
3.2.1 γ-induced showers . . . 41
3.2.2 Hadron-induced showers . . . 42
3.3 Cherenkov radiation from EAS . . . 43
3.4 Imaging technique . . . 46
3.5 The MAGIC Telescope . . . 49
3.6 Telescope structure and drive system . . . 49
3.7 Reflector and Active Mirror Control . . . 51
3.8 Camera . . . 52
3.9 Signal transmission . . . 54
3.10 Receiver, Trigger and Data acquisition . . . 54
3.11 Calibration . . . 55
3.12 MAGIC observation modes and Data . . . 57
3.13 Dailycheck . . . 57
3.13.1 Automatic dailycheck . . . 58
3.14 MAGIC stereo system . . . 60

4 Analysis of the MAGIC data 63
4.1 Introduction . . . 63
4.2 Charge and arrival time reconstruction . . . 63
4.3 Image cleaning . . . 65
4.4 Data selection . . . 65
4.5 γ/hadron separation . . . 67
4.5.1 Random Forest . . . 68
4.5.2 Signal extraction . . . 70
4.6 Skymap . . . 72
4.7 Energy spectrum . . . 75

4.7.1 Energy reconstruction . . . 75
4.7.2 Flux estimation . . . 76
4.7.3 Unfolding . . . 76
4.8 Light curve . . . 78

5 QSO: 3C 454.3 **79**
5.1 Introduction . . . 80
5.2 MAGIC observations . . . 80
5.3 Results . . . 81
5.4 Discussion . . . 82
5.5 3C 454.3 flare in 2009 . . . 88

6 HBL: PG 1553+113 **91**
6.1 Introduction . . . 92
6.2 Observations . . . 93
6.2.1 Optical and Near Infrared (NIR) data . . . 93
6.2.2 X-rays: RXTE/ASM Observations . . . 94
6.2.3 γ-ray data . . . 94
6.3 Results . . . 96
6.4 Discussion . . . 98

7 Variability in AGN **103**
7.1 Introduction . . . 104
7.2 χ^2 minimization of SSC model . . . 104
7.3 Source selection . . . 105
7.4 Results and conclusion . . . 107

8 Estimation of EBL density **113**
8.1 Introduction . . . 114
8.2 EBL absorption . . . 116
8.3 EBL absorption as an estimator of EBL density . . . 118
8.4 The proposed method . . . 119
8.4.1 Fitting tecnique: χ^2 minimization . . . 121

8.5 Results: application to PKS 2155-304 121
8.6 Discussion 127

A Appendix: Observation of Cassiopeia-A with MAGIC telescope 129
A.1 Introduction 130
A.2 Observation 130
A.3 Analysis 130

B Appendix: Dailycheck software 135
B.1 Automatic Daily check 136

C Appendix: Fux extrapolator in VHE range 139
C.1 Flux extrapolator 140

Bibliography 143

1

Very High Energy γ-ray Astrophysics

1.1 General Introduction

The ground for the discovery of cosmic radiation was prepared by the investigations of electrical conductivity of gases. C. T. R. Wilson (1900) and Ester and Geitel (1900) independently observed that electroscope in a vessel at earth potential gradually lost its charge even if they are very well insulated. It was shown that the loss of charge was due to gaseous ion. An ion current can only be maintained if the ions which are swept away by the electric field, are consistently replaced by new ones. The assumption that the ions are produced by some internal mechanism as, for example, by thermal agitation, was rejected as improbable, and it was concluded that the ionization must be due to some outside agency such as X-rays or γ-rays. C. T. R. Wilson tentatively suggested that the ionizing agency might be an extremely penetrating radiation of extra-terrestrial origin.

Later investigations showed that the ionization in a closed vessel is due to a penetrating radiation which emanates partly from the walls of vessel and partly from outside. That part of the radiation comes from outside was established by Rutherford and Cook (1903) and by McLennan and Burton (1903) by showing that the rate of ionization in a closed vessel decreases when the vessel is surrounded by a sufficiently thick layer of material.

A large number of investigations on the conductivity of gases and its cause followed. Wulf and Gockel (1909) as a result of the analysis of their own results and those of others came to the conclusion that the whole of penetrating radiation can be accounted for in terms of the γ-rays emitted by the radioactive substances present near the surface of the earth. This conclusion was not accepted by Pacini (1912) who observed simultaneous variations of the rate of ionization on mountains, over a lake and over the sea. Pacini

concluded that a certain part of the ionization must be due to sources other than the radioactivity of the earth or the air. The observations of Simpson and Wright (1911) showed a considerable rate of ionization over the sea. This also could not be accounted for by radioactivity, as sea-water contains only negligible amount of radioactive contamination. It was also noticed that the ionization in a closed vessel changed with the barometric pressure. In spite of these difficulties physicists were reluctant to give up the hypothesis of a terrestrial origin of the penetrating radiation. Wulf (1910) measured the rate of ionization on the top of Eiffel tower in Paris (300 m. above ground). He expected to find at the top of the tower a much smaller ionization than on the ground because of the absorption in air of the γ-rays emanating from the ground. The rate of ionization showed, however, too small a decrease to confirm the hypothesis of a terrestrial origin. Similarly Gockel (1911) ascending in a balloon up to 4000 m. above sea-level, found that the ionization did not decrease with height as expected on the hypothesis of terrestrial origin. Gockel's results were somewhat uncertain as he used an ionization vessel in which the pressure varied with the outside pressure and no correction was made for this factor.

The extra-terrestrial origin of at least part of the radiation causing the observed ionization was established during the next few years. In a number of balloon flights up to 5000 m. above sea-level Hess (1912) succeeded in showing that ionization, after passing through a minimum, increases considerably with height. Hess concluded that the increase of ionization with height must be due to a radiation coming from above, and he thought that this radiation was of extra-terrestrial origin.

The results of Hess were later confirmed by Kolhorster (1919) in a number of flights up to 9200 m. above sea level. An increase of the ionization up to ten times that at the sea level was found. The absorption coefficient of the radiation was estimated to be 10^{-5} per cm of air at N.T.P. This value caused great surprise as it was eight times smaller than the absorption coefficient of the air for most of the penetrating γ-rays known at that time.

The ionization curve was extrapolated from the heights where the ionization was certainly caused by cosmic radiation alone down to sea-level. It was estimated that the cosmic rays coming from above were responsible for the production of 1 to 2 ion pair per c.c. per sec. of the ionization near the ground, while most of the ionization, which amounted to 6 to 10 ion pairs per c.c. per sec., had to be attributed to the radioactivity of the ground.

The ionization over the sea is mainly due to cosmic rays.

After the publication of the first results by Hess and Kolhoster a violent controversy as to the existence of an extra-terrestrial radiation or cosmic radiation resulted, in which Millikan and his co-workers (1923), Hoffman (1925), Behounek (1926) took part. The original results were, however, maintained by Hess (1926) to be correct; they were fully confirmed somewhat later and the existence of cosmic radiation has been fully accepted since about 1926.

Before going into the details of cosmic photons, especially γ-rays, a short over view on cosmic rays and neutrinos is given.

1.2 Cosmic rays

Cosmic rays are highly energetic particles originate from outer space. It mainly consists of protons, heavy nuclei (upto Fe), electrons and positrons. Fig.1.1 shows the cosmic ray spectrum. The differential energy spectrum has been multiplied by $E^{2.7}$ to display the features of the steep spectrum. The steepening around 10^{15} - 10^{16} eV is known as the knee of the spectrum. The features around 10^{19} eV is called the ankle of the spectrum. Measurements with small air shower experiments in the knee region differ by as much as a factor of two, which indicates the systematic uncertainties in interpretation of the data. An unfolding procedure (Antoni2005 [50]) has been used to obtain the spectra of the individual components, giving a result for the all particle spectrum between 10^{15} and 10^{17} eV. Flourscence technique (Bird1994 [58]) is used in the energy range above 10^{17} eV, because the technique can establish the primary energy in a model independent way by observing most of the longitudinal development of each shower, from which E_0 is obtained by integrating the energy deposition in the atmosphere. The result however depends strongly on the light absorption in the atmosphere and the calculation of the detector's aperture.

Assuming the cosmic energy spectrum bellow 10^{18} eV is of galactic origin, the knee could reflect the fact that most cosmic accelerators in the galaxy have reached their maximum energy. Some types of expanding supernova remnants, for example, are estimated not to be able to accelerate protons above energies in the range of 10^{15} eV. Effects of propagation and confinement in the galaxy also need to be understood.

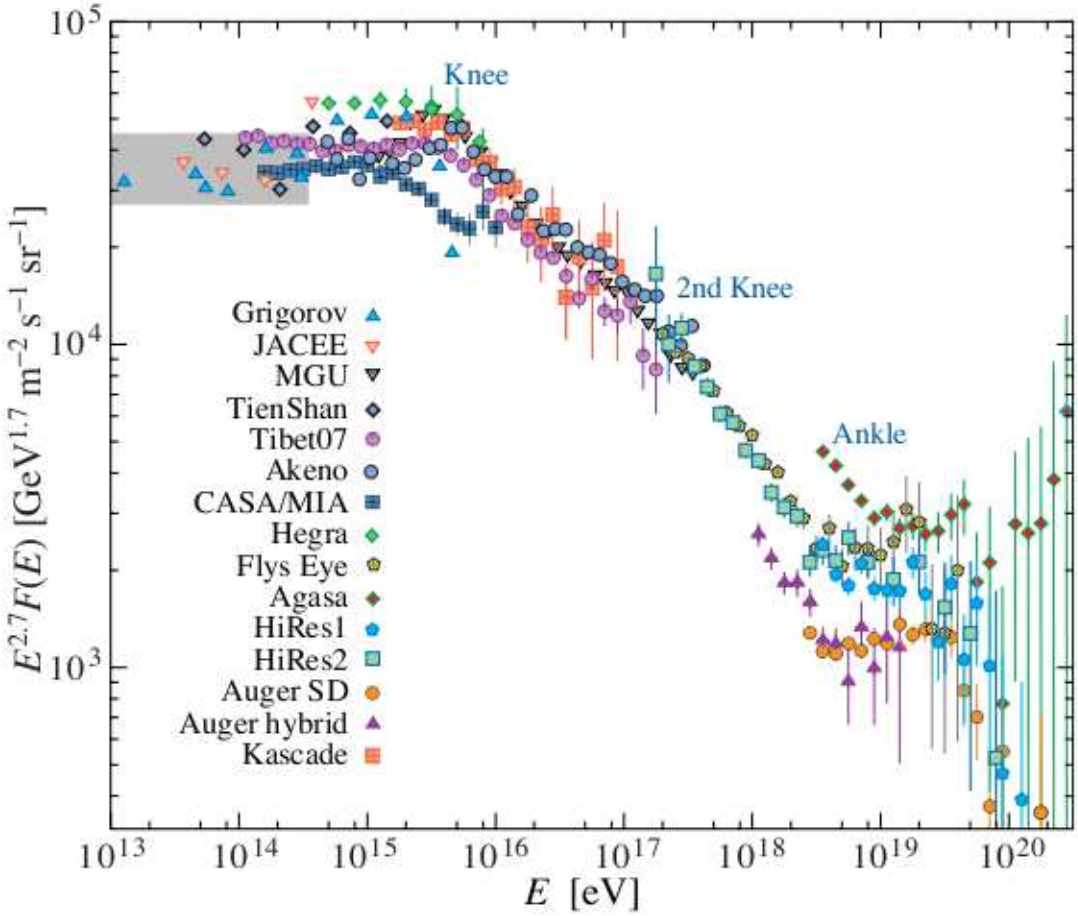

Figure 1.1: Cosmic ray spectrum measured by various experiments (Gaisser2009 [112]).

Concerning the ankle, one possibility is that it is the result of a higher energy population of particles overtaking a lower energy population, for example, an extragalactic flux beginning to dominate over the galactic flux (Bird1994 [58]). Another possibility is that the dip structure of the region of the ankle is due to $\gamma_p \rightarrow e^+ + e^-$ energy losses of extragalactic protons on the 2.7 K cosmic microwave radiation (CMB). This dip structure has been cited as a robust signature of both the protonic and extragalactic nature of the highest energy cosmic rays (Brezinsky2006 [71]). If this interpretation is right, then the end of the galactic cosmic ray spectrum would be at an energy lower than 10^{18} eV, consistent with the maximum expected range of acceleration by supernova remnants.

Energy dependence of the composition from the knee through the ankle holds the key to discriminate between these two view points. The HiRES and Auger experiments, however, present very different data on the UHECR composition from the observation of

the depth of shower maximum $X_{\max}$. The HiRES data is fully consistent with a cosmic ray composition getting lighter and containing only protons and helium above 10^{19} eV. Auger sees a composition getting lighter up to 2×10^{18} eV and becoming heavier after that to become intermediate between protons and iron at 3×10^{19} eV. This may mean that the extragalactic cosmic rays.

If the cosmic flux at highest energies is cosmological in origin, there should be a rapid steepening at the spectrum (GZK feature) around 5×10^{19} eV, resulting from the onset of inelastic interactions of UHE cosmic rays with CMB (Greisen1966 [130], Zatespin1966 [249]). Although all UHECR experiments have detected events of energy above 10^{20} eV, the spectral shape above the ankle is still not well determined. The AGASA experiment (Takeda2003 [222]) claimed 11 events above 10^{20} eV (even though a recent re-analysis has decreased that number), while HiRES (Abbasi2008 [3]) detected only two. The Auger observatory (Abraham2008a [4]) presented spectra based on its surface detector and on events detected with both the surface and the flourscence detectors. Both HiRES and Auger spectra show a significant steepening of the cosmic ray spectrum above 3-5 $\times 10^{19}$ eV which is consistent with the onset of inelastic interactions with astrophysical photon field, mostly the CMB.

Fig.1.2 gives an expanded view of the high energy end of the spectrum, showing only the more recent data, including the spectrum derived by HiRES in stereo mode. This figure shows that the differential flux multiplied by $E^{2.6}$ which the Auger observatory finds around 10^{19} eV. The two experiments are actually consistent in normalization if one takes quoted systematic errors in the energy scales into account. The continued power law type of flux beyond the GZK cut-off claimed by the AGASA experiment is not supported by HiRES and Auger data.

1.3 Neutrinos

The existence of neutrinos were postulated by Pauli in 1931 for making the β-decay consistent with the conservation laws of energy and momentum, and it was experimentally discovered in 1959. According to the standard model of particle physics, there are three neutrinos associated with three leptons - electron, muon and taon.

Neutrinos are detected indirectly. Neutrino telescopes usually contain a large volume

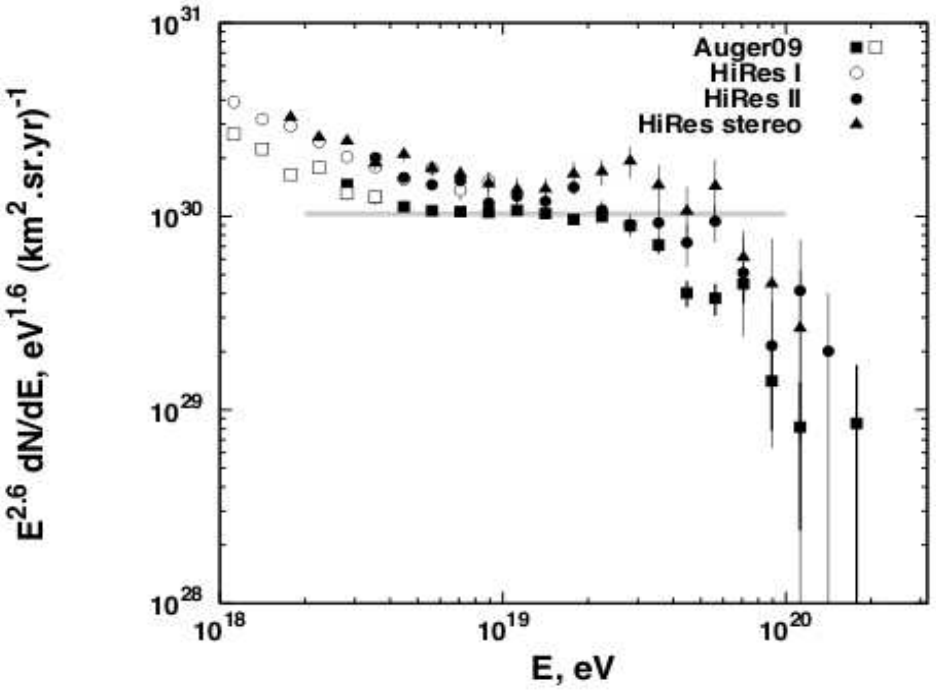

Figure 1.2: Measured UHECR spectrum (Gaisser2009 [112]).

of matter, like water or ice with an array of photo multiplier tubes (PMTs). Neutrino interacts in the large volume, and Cherenkov light produced by the resulting secondary particles (leptons) are detected by PMTs. The major goal of the current experimental projects like Ice cube is to study neutrinos in a range of 10^{11} - 10^{21} eV. There are several ongoing projects to construct next generation neutrino detectors (Halzen2007 [134]).

One half of the energy that UHECR photons lose in photoproduction interactions that cause GZK effects ends up in neutrinos. Measuring the cosmogenic neutrino flux above 10^{18} eV would help resolve the UHECR uncertainties. The magnitude of this flux depends strongly on the cosmic ray spectrum at acceleration, the cosmic ray composition, and the cosmological evolution of cosmic ray sources. In the case that UHECR have mixed composition only the proton fraction would produce cosmogenic neutrinos. Heavy nuclei propagation produces mostly $\overline{\nu_e}$ at lower energy from neutron decay.

The expected rate of cosmogenic neutrinos is lower than current limits obtained by RICE (Kravchenko2006 [156]), the Auger observatory (Abraham2008 [5]) and ANITA (Gorham2009 [129]) which are shown in Fig.1.4. together with a model of cosmogenic

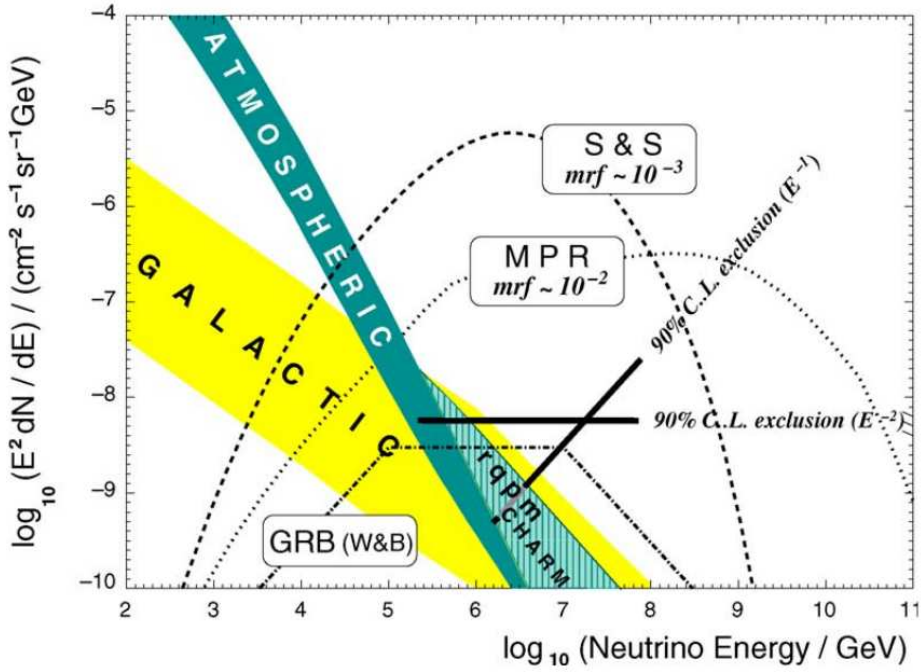

Figure 1.3: Diffuse Neutrino Flux vs. Energy for various models of sources contributing to the diffuse background. The IceCube sensitivity in three years is shown in dash-dotted line (Ahrens2004 [29]).

neutrino production (Engel2001 [92]), and an upper limit of neutrinos that can be accelerated at the cosmic ray sources (Waxman1999 [241]). One has to note that the limits are calculated in different ways. Those of ANITA and RICE are for all neutrino flavors, where the contribution of different flavor is energy dependent. The limit of Auger is only for ν_τ and $\overline{\nu_\tau}$ which should be about 1/3 of the total neutrino flux after oscillations on propagation.

1.4 Photons

Unlike charged cosmic particles or neutrinos with low cross section, high energy photons can provide more information on the universe because they retain information on their original direction. Though high energy photons are referred to as γ-rays - photons above 0.511 MeV - multi-λ photon observation is briefly described.

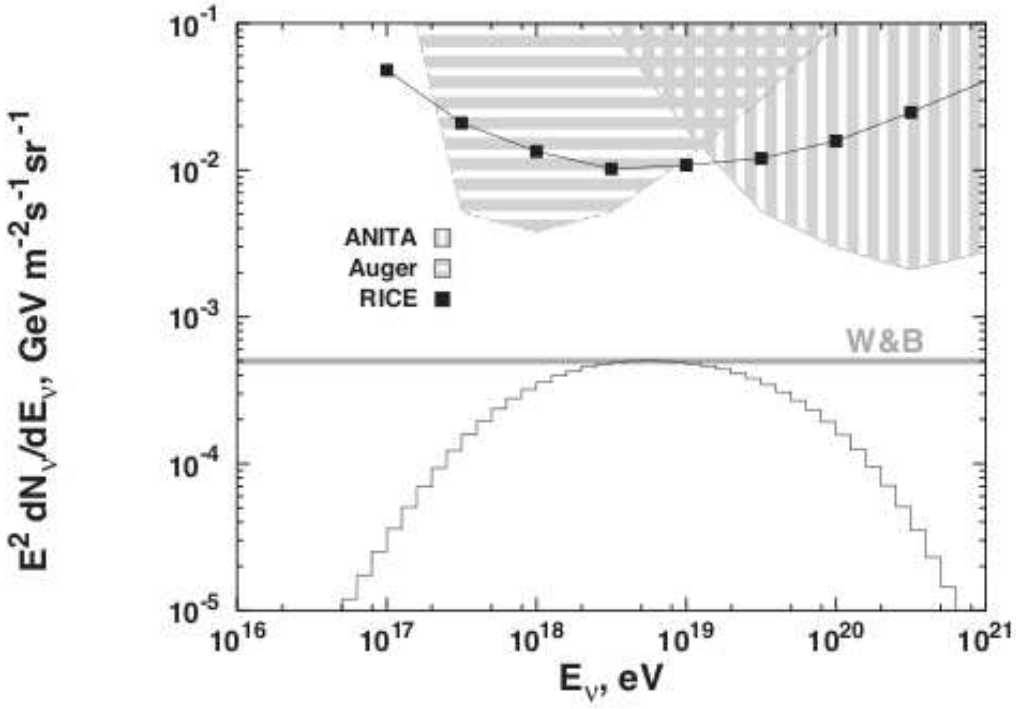

Figure 1.4: Limits on flux of cosmogenic neutrinos by neutrino experiments. The histogram shows sum of all three neutrino flavors (Gaisser2009 [112]).

1.4.1 Radio

Radio astronomy began with the Karl Jansky's detection of radio waves from the Milky Way (Jansky1933 [146]). Due to their large λ, radio waves undergo less scattering, hence radio sources can be viewed even through dust in the line of sight with less absorption in the atmosphere. As the angular resolution of the telescope is proportional to the wavelength ($\alpha = \frac{1.22\lambda}{D}$), large telescopes are needed for radio observation. However, this difficulty can be overcome by interferometry, in which many telescopes separated by a distance are used to observe the same object, hence effectively increasing aperture, D. Adding data from different telescopes using time information resemble data from a large area telescope. The Very Large Baseline Array (VLBA) of the National Radio Astronomy Observatory in the USA is the foremost example for the instruments of this category. Radio astronomy is important for both galactic and extra galactic objects. The cosmic microwave radiation was first understood by radio telescopes (Penzias1965 [183]).

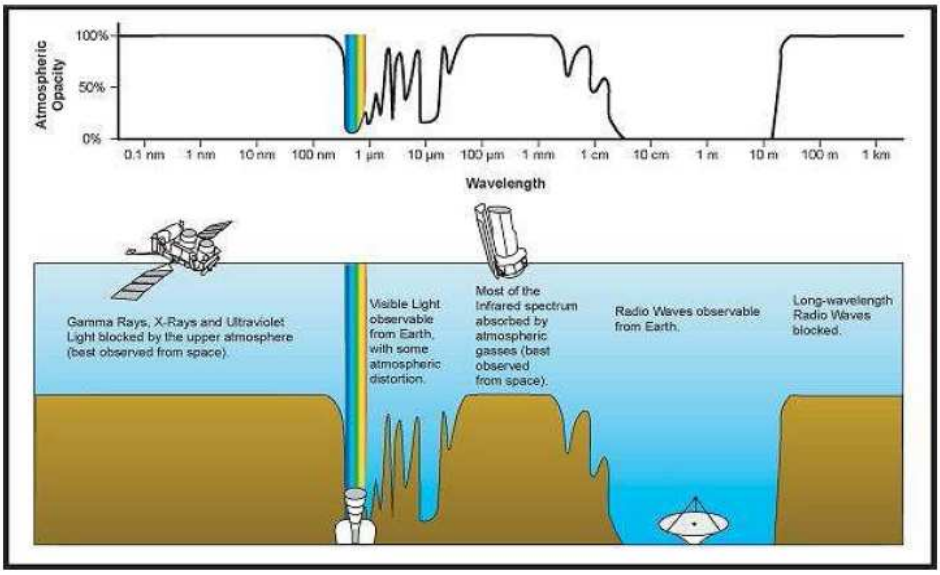

Figure 1.5: Opacity of the earth's atmosphere to the electromagnetic spectrum Dorner2008 [89].

1.4.2 Infrared (IR)

IR signal detection is strongly affected by water vapor in the atmosphere that can distract IR signal, and different objects of room temperature that emit IR radiation. Far Infrared (FIR) objects are not observed with ground based telescopes, but with aircrafts or balloons. The 2 μm all sky survey (2MASS) observed the whole sky at J (1.25μm), H (1.65μm) and K_s (2.17μm) wavelengths. More than 95% of sky survey was obtained with Infrared Astronomical Satellite (IAS), in both the MIR (Mid IR) and FIR region. IR observation of extra galactic objects like star-forming galaxies are crucial because most of the latter's radiation is emitted in the IR (8-1000μm) by warm molecular and dust clouds that are heated by the newly born stars that emit large amount of ultraviolet radiation. Once the later is absorbed by the surrounding clouds, the absorbed power is re-emitted in the IR. The IR activity is an immediate tracer of current star formation activity (Kennicut1998 [148]).

1.4.3 Optical

Optical frequency is the oldest window in the electromagnetic spectrum to observe the cosmos. In particular with the high energy phenomena, optical telescopes are important for γ-ray burst observation and to give alerts to γ-ray telescopes, and for Active Galactic Nuclei (AGN) studies as they are crucial to detect the synchrotron peak of the spectrum. For example, KVA telescope supports MAGIC telescope by photometric observations. They are also used as polarimetry studies of binary stars, inter stellar dust and magnetic field. The optical emission and absorption lines are used to determine the cosmological source redshifts.

1.4.4 Ultraviolet (UV)

In electromagnetic spectrum, the 10 - 380 nm wavelength range is the UV range. The 100 - 200 nm range is the Far UV (FUV) and 200 - 380 nm is Near UV (NUV). NUV observations can be performed by optical telescopes, whereas FUV can only be performed in space, due to the atmospheric absorption. The International Ultraviolet Explorer (IUE) from 1978 to 1996, and the UV instrument in Hubble Space Telescope have been two important instruments in this range. The observation of UV frequency, together with soft X-ray observation helps to determine the synchrotron peak of AGN flux distribution.

1.4.5 X-ray

X-ray astronomy is relatively new (since 1962; Giacconi1962 [121]) as the observations are performed by rockets or satellite experiments because of the atmospheric absorption of X-rays. It can be subdivided into hard (10-100 keV) and soft (0.1 - 10 k eV) X-rays. Uhuru, the first imaging X-ray telescope detected 339 X-rays sources in its sky survey in 1971. In 1990, The Rontgen Satellite (ROSAT) carried out a sky survey and detected more than 60,000 X-ray sources including extended objects (Voges1999 [238]). BeppoSAX (1996-2002) observed the X-ray sky between 0.1 keV and 300 keV with five instruments in different frequency range, resulted in a catalogue of 157 X-ray sources, including 84 spectral energy distributions of blazars (Giommi2002 [124]). The *Rossi* X-ray Timing Explorer (*R*XTE) was launched in 1995 to study the time variability of X-ray sources in a moderate spectral resolution. Two major satellites - ESA's XMM-Newton and NASA's

Chandra - were launched in 1999 and are still active. XMM-Newton has less spatial resolution than Chandra, but a larger collection area, hence a better spectral resolution. High resolution and sensitivity in higher X-rays help Chandra to study faint objects. $Swift$ is devoted to Gamma Ray Bursts. Burst Alert Telescope (BAT; 15 - 150 keV), in $Swift$ detects GRBs. Follow up observation of the afterglow are performed using X-ray Telescope (XRT) and Ultraviolet/Optical Telescope (UVOT). Suzaku contains a new generation X-ray spectrometer of a higher resolution. Monitor of All-sky X-ray Images (MAXI) is the latest instrument in X-ray astronomy. It consists of high sensitive X-ray slit Cameras in 0.5 - 30 keVs. The expected detectability of MAXI is $\sim$ 0.2 mCrab in two years (Matsuoka2009 [169]). The instrument will also be crucial in understanding the correlations in different energies in multi-λ observations of AGN, which is one of its main goal.

1.5 γ-ray Astronomy

γ-rays are defined as radiation where frequency exceeds the electron mass energy equivalent - 511 keV. Generally, γ-rays between 0.5 MeV - 30 MeV is the Low energy (LE) range, 30 MeV - 30 GeV is the High energy (HE) range, 30 GeV - 100 TeV is the Very High energy (VHE) range, 100 TeV - 100 PeV is the Ultra High Energy (UHE) range and 100 PeV - 100 EeV is the Extremely High Energy (EHE) range. Most of the known γ-ray sources produce γ-rays till VHE range. The past and current important experimental approaches in this region is described.

1.5.1 HE γ-ray

High Energy γ-ray experiment began with the cosmic γ-ray detection of above 70 MeV from the galactic plane by the Orbiting Solar Observatory (OSO-3; Kraushaar1972 [157]). The Small Astronomy Satellite (SAS-2) found evidence of γ-ray emission from single sources, the Vela pulsar and the Crab Nebula. In more recent times, the Compton Gamma ray Observatory (CGRO) (1991-2000) covered many sources in the MeV - GeV range. CGRO was equipped with Energetic Gamma Ray Experiment Telescope (EGRET). The sky surveys of EGRET is given in the third EGRET catalogue (Hartman1999 [135]), which includes cat-

alogue includes 70 blazars, 5 pulsars, 1 radio galaxy, 1 normal galaxy, and 170 unidentified sources.

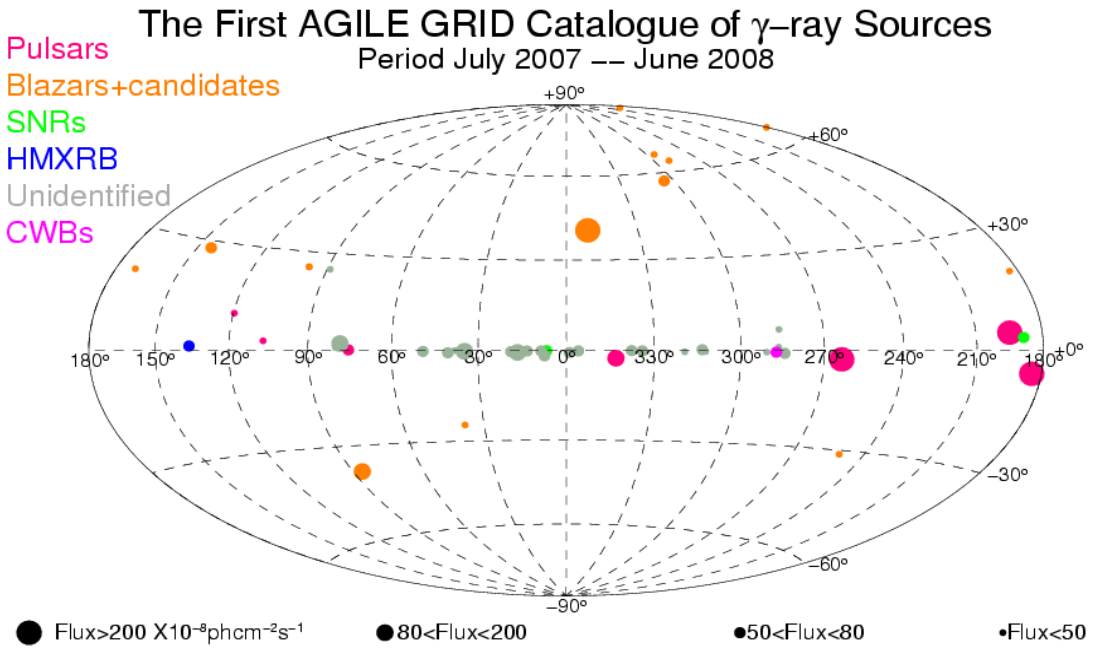

Figure 1.6: AGILE-GRID first catalogue of High energy Gamma ray sources in the period of July 2007 and June 2008 (Pittori2009 [188]).

Currently the most important instruments are ASI's AGILE (Astro-rivelatore Gamma a Immagini Leggero), and NASA's *Fermi* (formerly GLAST) Gamma ray satellite.

AGILE contains three instruments. Gamma Ray Image detector (GRID) is sensitive in the energy range of 30 MeV - 50 GeV. Hard X-ray Imager (Super AGILE) which is sensitive in 18 - 60 keV range, is placed on the top of GRID. A mini calorimeter acts as a third detector in 350 keV - 50 MeV band. The accessible field of view of AGILE is more than 1/5 th of the total sky. A number of γ-ray sources have been detected by AGILE by this time. The first AGILE-GRID catalogue (Pittori2009 [188]) of high energy Gamma ray sources is shown in Fig.1.6.

The *Fermi* γ-ray Space Telescope studies the cosmos in the photon energy range from 8 keV to 300 GeV. *Fermi* carries two instruments, the Large Area Telescope (LAT) and the GLAST Burst Monitor (GBM). The energy range of LAT is 30 MeV - 300 GeV. In particular, the LAT has high sensitivity above 10 GeV in order to give importance in this

range as our knowledge in $\sim$ 10 - 100 GeV is very limited. The field of view of LAT is 1/5 th of the sky, like AGILE's. The GBM can measure photon energy over a wide range, down to 8 keV and up to energies that overlap the LAT energy range. During the first three months of sky survey, LAT detected 132 bright sources including 2 radio galaxies, 104 blazars (57 Flast Spectrum Radio Quasars (FSRQs) and 42 BL Lac objects) and 5 AGN of uncertain classification (Abdo2009a [1]).

1.5.2 VHE γ-ray

This is one of the youngest branches of Astroparticle Physics. It is comparatively difficult to detect VHE γ-rays, because of complex detection techniques. VHE γ-ray astronomy became a reality after atmospheric Cherenkov imaging technique. In the next sections, I will briefly explain VHE γ-ray experiments and sources.

Two types of ground based detectors are used in VHE astronomy. Extensive Air Shower arrays (EAS) and Cherenkov telescopes. While Cherenkov Telescopes offer high sensitivity in the lower part of VHE region ($\sim$ 100 GeV), EAS detectors offers wide field of view at higher energies ($>$ 1 TeV). Currently, there are three main EAS detectors. ARGO-YBJ detector ($\sim$ 4000 m a.s.l) in Tibet was made of resistive plate chambers. The detector's angular resolution is $\sim 0.5^{\circ}$ while energy threshold is 0.5 - 1 TeV. MILAGRO's detector ($\sim$ 2630 m a.s.l) consists of a central water reservoir (area $\sim$ 4000 m^2) surrounded by 175 water tanks in which PMTs are attached, and is sensitive in an energy range of $\sim$ 250 GeV - 50 TeV. The Tibet AS-Gamma experiment ($\sim$ 4300 m a.s.l) uses 697 scintillation counters consisting of a plate of plastic scintillator attached to PMTs to obtain a threshold energy of 3 TeV. The Cherenkov telescope techniques are described in a dedicated chapter (See chapter 3).

1.6 VHE γ-ray sources

Discoveries of various VHE γ-ray sources are achieved after the Image Atmospheric Cherenkov Technique (IACT). Ground based γ-ray telescopes with large detection area is well suited for the detection VHE γ-rays. The lowest energy threshold before the new generation Cherenkov telescope's arrival was about 350 GeV, which limited the detection of new

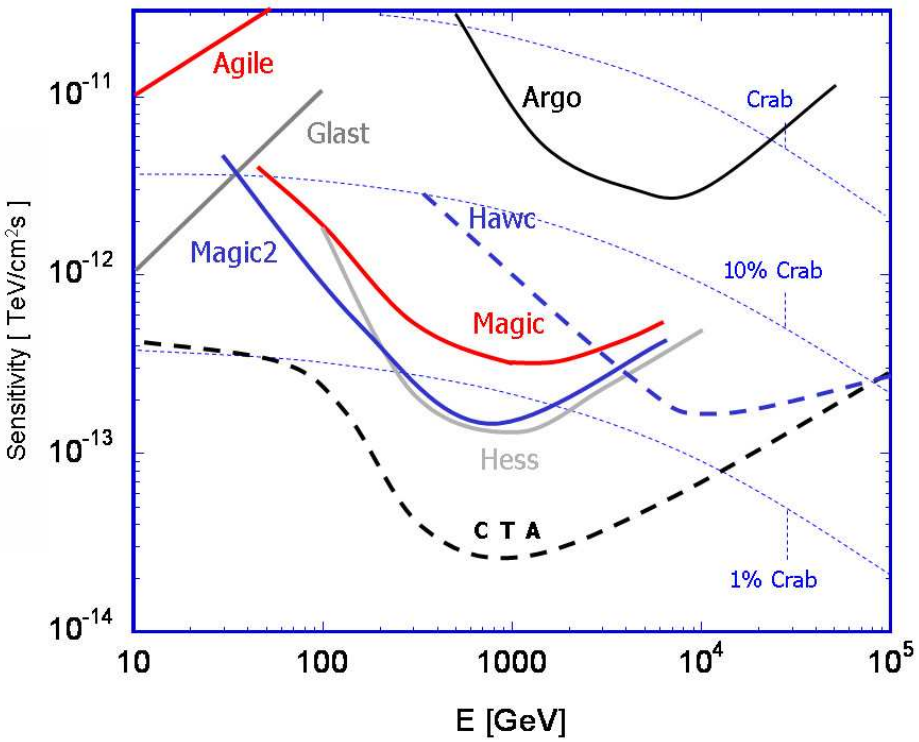

Figure 1.7: Sensitivity of current and future VHE experiments.

sources because of the generally steep spectra of γ-ray sources. Thanks to new IACT techniques, current Cherenkov telescopes reduced the lower energy threshold (MAGIC $\sim 25\,\mathrm{GeV}$, HESS $\sim 100\,\mathrm{GeV}$, VERITAS $\sim 100\,\mathrm{GeV}$) with high sensitivity. VHE γ-ray sources are divided into galactic and extra galactic sources.

1.6.1 Galactic sources

Supernova Remnant (SNR): A massive star ($> 8\,\mathrm{M}_\odot$) explodes at the final stage of its evolution to form a Supernova. Depending on the initial mass of the star, it forms to a neutron star or a black hole. SNR is the left over of a supernova explosion. SNR is believed to be the prime plea for galactic cosmic ray acceleration. The magnetic inequalities associated with the expanding waves make suitable situation for the Fermi-I acceleration mechanism to work. Depending on the morphology of the SNR, they can be divided in to shell type, crab-like or composite. Crab Nebula, the first detected TeV emitter (Weekes1989 [243]) is the strongest source of steady VHE emission in the Galaxy.

Pulsars: Neutron stars (NS) are formed after SN explosion of a massive star of 4 - 8

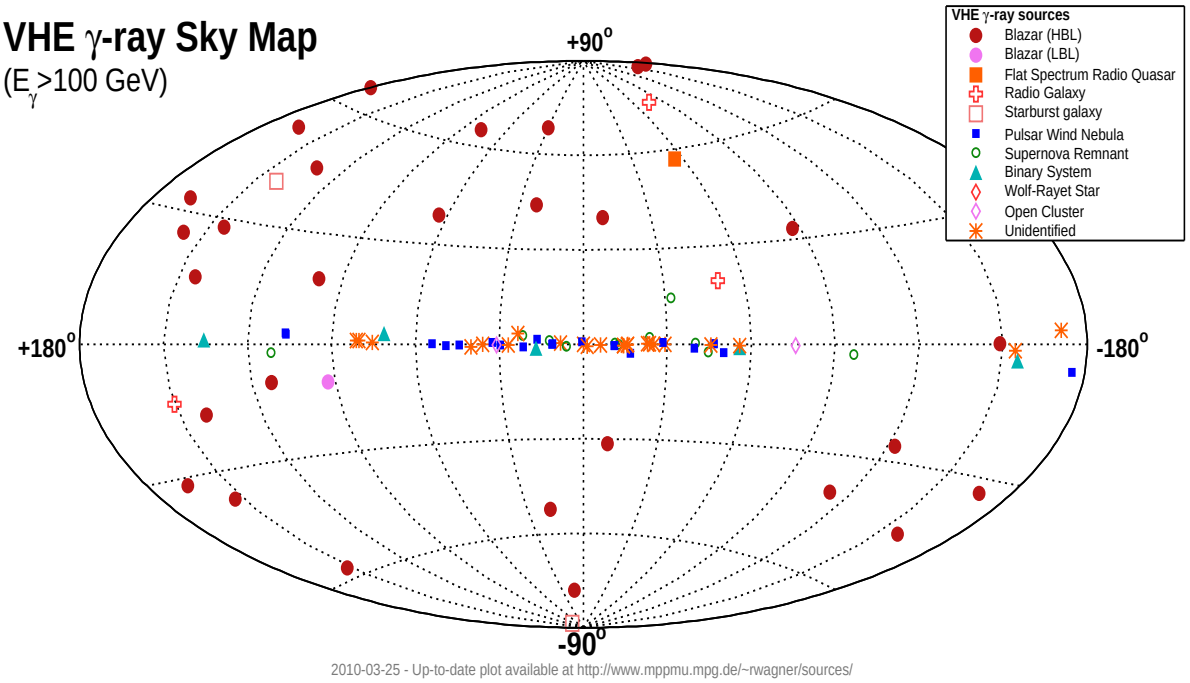

Figure 1.8: VHE γ-ray sky map, taken from Wagner2010 [242]

$M_{\odot}$. After the explosion, the central region starts collapsing towards the center because of the gravity and its constituent matter becomes neutronized. Pulsars are rotating neutron stars. The γ-ray production is believed to be due to the synchrotron-curvature radiation (Daugherty1982 [82]). It can be produced either near the magnetic pole (polar-cap model; Baring2004 [51]) or farther away from the magnetosphere (outer-gap model; Tang2008 [223]). A recent MAGIC observation (Aliu2008 [45]) of Crab pulsar supports the outer gap model.

Microquasars: Microquasars are accreting X-ray binary stars composed of a main sequence star and a compact (BH or a NS) object which produce relativistic jets perpendicular to both side of accretion disk. The compact object in the binary system receives material from its stellar companion. In order to conserve the angular momentum, the material forms an accretion disk around the compact object. In a not fully understood way the disk supplies the energy for the relativistic jets. The disk's temperature is high enough to thermally emit X-rays. A popular model of microquasars can be found in Mirabel1994 [175]. Other than the difference in scale, the Physics of quasars and mi-

croquasars are believed to be the same. The variations observed in microquasars in time scales of minutes correspond to a similar phenomena of quasars that would take thousands of years, because of the smaller size of microquasars. Microquasars has been detected by HESS (Aharonian2005 [14]) and MAGIC (Albert2006a [30]) in VHE band.

Galactic center: The galactic center, the most violent and active region in the Milky-Way is a difficult region for VHE astronomy. The region is rich of many possible astrophysical VHE γ-ray sources (not to mention the possibility of VHE emission from DM decay). The current VHE instruments do not have a resolution sufficient to gain a clearer view of this region. However, the galactic center has been observed by IACT instruments (Tsuchiya2004 [231], Aharonian2004a [11], Kosack2004 [154], Albert2006b [31]).

1.6.2 Extra Galactic Sources

Gamma Ray Burst (GRB)

GRBs are the brightest known phenomena in the universe. Such bursts occur approximately once a day, for a short time scale of a few seconds. Long after their mainstream discovery in 1973, the origin of GRBs is still under debate. Popular models say that, they are Hypernova (a specialized model of Supernova) explosions. The fireball model suggests that GRBs occur when the explosion produced relativistic outflow of optically thick plasma shell becomes optically thin (Rees1992 [196]). The detection of X-ray afterglow by the Beppo-SAX satellite was a break through in GRB studies (Costa1997 [78]). The afterglows typically lasting for weeks were detected in optical and radio frequencies. Afterglows also proved crucial in measuring the redshift and identifying host galaxies . The average of measured redshift of GRBs is 2.4, which makes GRB detection difficult in VHE range, as they can be absorbed by Extragalactic Background Light (EBL). However, nearer GRBs ($z < 1$) in principle can be detected by current VHE instruments. The MAGIC telescope is ideal for GRB observations because of its short slewing time (average of 30 s) and low energy threshold ($\sim$25 GeV). As of now, 47 GRBs has been observed by MAGIC, however no detection is reported. Details of GRB observation in the cycle 2005 - 2006 can be found in Albert2007 [39].

Active Galactic Nuclei (AGN)

AGN are believed to be the most powerful energy source in the universe. The current

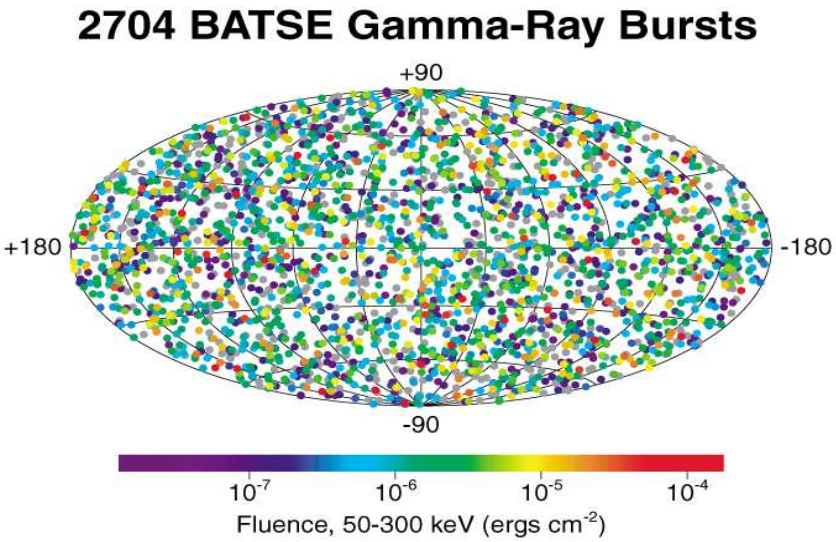

Figure 1.9: 2704 GRBs observed by BATSE shows the isotropy of GRBs on the sky

models assumes that there is a super-massive black hole (SMBH) at the center of all galaxies. 1% of these galaxies produce non thermal radiations and show high activity in their centers, are called AGN. According to the unified model of AGN, the SMBH which has a mass of 10^6 - $10^{10}\,M_\odot$, is surrounded by a disc of accreting material. Two plasma jets are expelled from both sides from the center of the galaxy, perpendicular to the disc, propagating in a range of kpc - Mpc (Begelman1984 [53]). Non-thermal emission from jets are variable in all frequencies. If the jet is pointed to a small angle to the line of sight of the observer, AGN are called blazars. Up to now, the great majority of AGN detected in VHE band are blazars. The overall spectral energy distribution (SED) of AGN shows two broad non-thermal continuum peaks. More on AGN can be found in Chapter 2.

2

Active Galactic Nuclei

2.1 Introduction

The observation of bright emission and absorption lines from NGC 1068, a spiral galaxy (Fath1909 [97]) can be considered as the beginning of AGN studies. It was found that the emission lines were spread over a wide range of frequencies. Similar emissions were noticed from NGC 4051, a spiral nebula (Hubble1926 [143]). Further details were revealed after Seyfert's studies on a set of galaxies with enhanced central surface brightness. The optical spectra of these objects were dominated by broad nuclear lines and broader hydrogen lines. The unresolved nucleus provided an average estimation of the size ($< 100\,\mathrm{pc}$) and the mass ($\sim 10^{9\pm1}\mathrm{M}_\odot$) of nucleus. Another breakthrough happened when a broad line emission was noticed in the spectra of 3C 48 and 3C 273 (Greenstein1964 [131]). These star-like objects were called quasi stellar sources or *quasars* (QSOs). A new model was proposed (Matthews1963 [171], Smith1963 [217]) to explain these observations, such that the central source of mass $10^9\mathrm{M}_\odot$ produce optical continuum, surrounded by an emission-line region, and with a larger radio emission region.

Only a few of the galactic nuclei are active and produce long jets. They are called AGN. It is believed that there exists a super massive black hole (SMBH) at the center of galaxies. One of the most promising examples of the existence of SMBH in AGN are based on the studies of rotation of central gas disks in nearby AGN like M 87 and NGC 4258 (Ghez2003 [115], Greenhill1995 [132]). Accretion on to the SMBH is considered to be the paradigm for the central engine of AGN (Salpeter1964 [201]). AGN produce electromagnetic radiation in a large span of wavelengths from radio to VHE γ-rays, and are believed to be one of the major sources of energetic cosmic rays.

2.2 Classification of AGN

Based on the observed phenomenology, AGN have historically been divided into different subgroups. This classification is not very precise due to the less statistics of AGN observations in all frequencies: it can be noted that some class of AGN overlap with another class.

Seyfert Galaxy: A Seyfert galaxies is usually a spiral galaxy with a bright nucleus at the center, which can even outshine the surrounding galaxy (Simkin1980 [215]). The variability in emission from these sources suggests that the emission region is comparatively smaller. Based on the relative width of emission lines in their optical spectra, Seyfert galaxies can be divided into two classes. Type 1 Seyfert galaxy (Sy I) have two sets of emission lines: (i) narrow forbidden lines ($\sim 100\,\mathrm{kms}^{-1}$), which is believed to be raised from narrow line region (NLR) with an electron density in order of $10^3 - 10^6\,\mathrm{cm}^{-3}$ and (ii) broader permitted lines ($\sim 10^4\,\mathrm{kms}^{-1}$) which comes from broad line region (BLR) with an electron density $\sim 10^9\,\mathrm{cm}^{-3}$. Type 2 Seyfert galaxy (Sy II) shows only narrow lines. Broad lines are either absent or very weak.

Quasar (QSO): The optical spectrum of QSO is similar to that of Sy I galaxy, with prominent broad lines and weak narrow lines. QSOs are found out to very high redshifts, $z \sim 5$. They are variable in all frequencies in time scales of months or even days. Only 10% of QSOs are radio loud (Ivezić2002 [145]), but all of them have substantial emission in IR, UV and X-ray to go along with their huge optical emission. A few of them have jets. Depending on the spectral slope Γ of the continuum spectrum at few GHz, radio-loud QSOs can be divided into Flat Spectrum Radio Quasar (FSRQ; $\Gamma \leq 0.5$) and Steep Spectrum Radio Quasar (SSRQ; $\Gamma > 0.5$).

Radio Galaxy (RG): A RG is usually giant elliptical galaxy with radio emission - even though some radio emission is also associated with QSOs. Like in the case of Seyfert galaxies, RGs can be divided into Broad-Line Radio Galaxy (BLRG) and Narrow-Line Radio Galaxy (NLRG), based on their optical spectra. Most of the RGs have jets. RGs can be divided in two types: Fanaroff Riley I (FR I) objects are center-bright, whereas Fanaroff Riley II (FR II) objects are lobe-bright (Fanaroff1974 [94]).

Low-Ionization Nuclear Emission Region (LINER): LINER is mostly found in spiral galaxies whose optical spectra resembles Sy II galaxies, but with weaker ionization

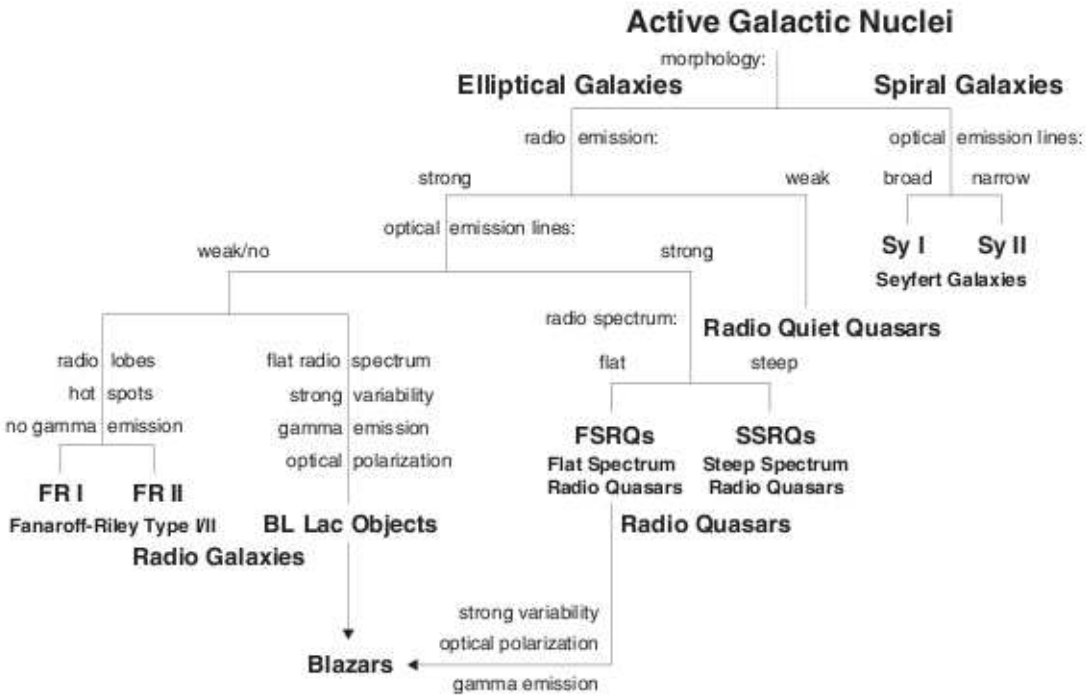

Figure 2.1: Classification of AGN(Böttcher1997 [69])

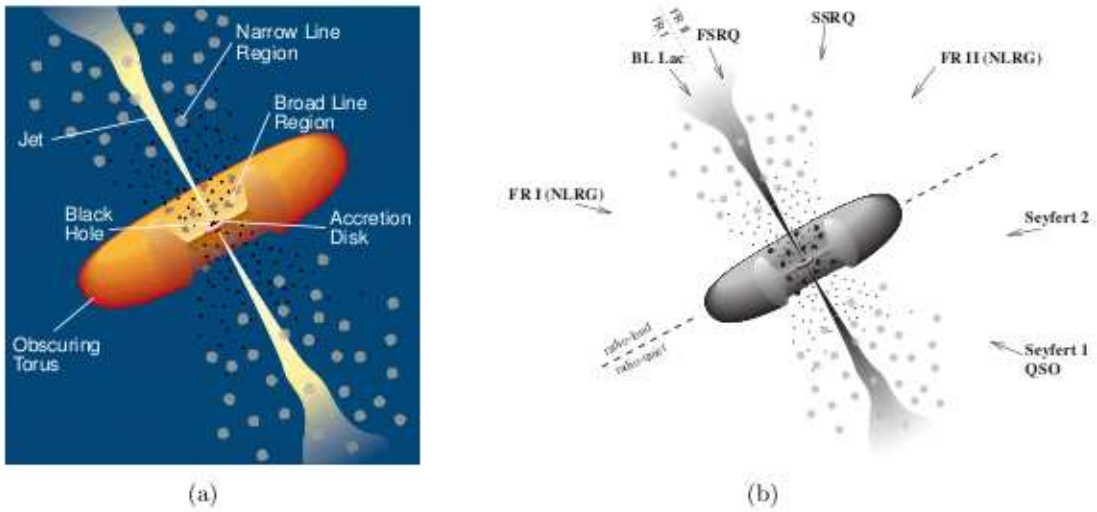

Figure 2.2: Schematic view of an AGN, taken from Urry1995 [232])

lines. The AGN connection to LINER is still not fully understood. A possibility is that LINERs are either low-luminosity AGN (Filippenko1984 [100]) or the result of thermal emission from massive star formation (Filippenko1992 [101]). However the presence of compact X-ray nucleus at the center supports the AGN nature of LINER.

OVVs and BL Lacs: Optically Violent Variable Quasars (OVVs) and BL Lacertae objects (BL Lacs) often show very rapid variability in all frequencies, and are strong radio sources. The difference between the two classes is based on their spectral properties. Compared to OVVs, BL Lacs have weak or no absorption lines. Based on their first peak (Synchrotron peak) of the double peaked SED, BL Lacs are classified as low peaked BL Lac (LBL; peak at IR or optical) and high peaked BL Lac (HBL; peak at UV or X-rays).

2.3 Unification of AGN

The unified model of AGN is a result of an attempt to explain all phenomenological classes of AGN as basically one same source observed from different lines of sight to the observer. According to these models (eg: Blandford1979 [59], Urry1995 [232]), AGN have a spinning SMBH at its center, which is surrounded by the disk that accrete onto the SMBH at approximately the Schwarzchild radius. It is believed that the accretion

mechanism leads to the jet flow: the spin of the SMBH induces twisted magnetic field inside jets (Blandford1977 [62]). Particles accelerate to ultra-relativistic energies inside jets. Different classes of AGN can be explained by the orientation of the AGN with respect to the observer, accretion rate and evolutionary status of the AGN.

According to accretion paradigm, AGN are powered by accretion onto SMBH (Blandford1991 [63]). The accretion rate ($\dot{m}$) determines the emission properties hence plays an important role in determining the class of the object. AGN with high accretion rate ($\dot{m} > 0.1$) produce thermal emission at optical frequencies (X-rays, if very high accretion rate), while low accretion matter results into emission in radio frequencies. This process ionizes the gas clouds closer to the SMBH which has high Doppler factor. This region acts as BLR. The molecular torus covers the BLR region when viewed from the equatorial direction. Gas clouds which are away from the SMBH (outside torus, and within polar cones) act as Narrow Line Region (NLR), due to the comparatively lower velocity of this region. If the jet is pointed towards the observer the AGN is called blazar. Sy II and NLRG are observer's equatorial view of an AGN, while Sy I and BLRG are intermediate view.

Three parameters - aspect, accretion rate and evolutionary status - have been suggested (Dopita1997 [87]) as the reasons of AGN appearance in different classes. When the line of sight to the observer is close to the torus, the BLR is obscured by the torus, hence only the NLR is visible: these AGN appear as Sy II galaxy. If the line of sight is close to the axis of the torus, the BLR is visible, and the AGN is called as Sy I galaxies. When the line of sight is on the jet axis, the intensity and the variability are boosted due to the beamed emission: the AGN are scene as blazars in this case. When the accretion to a BLR is very high, the accreting material is thick enough to obscure the radio jets: the AGN in this case radio quiet. This high accretion rate can not be maintained for a long time, which means the radio quiet condition changes into radio loud when the accretion rate slows down.

Even though SMBH are ubiquitous in AGN, QSOs are the most extreme cases, with BH masses ranging up to $6\times10^{10}M_{\odot}$. Binary black hole models have been confirmed only in the case of OJ 287 (Valtonen2008 [233]). Some authors (Wilson1995 [245], Blandford1999 [64]) relate the strength of radio jet with the spin of SMBH: the jet power could be proportional

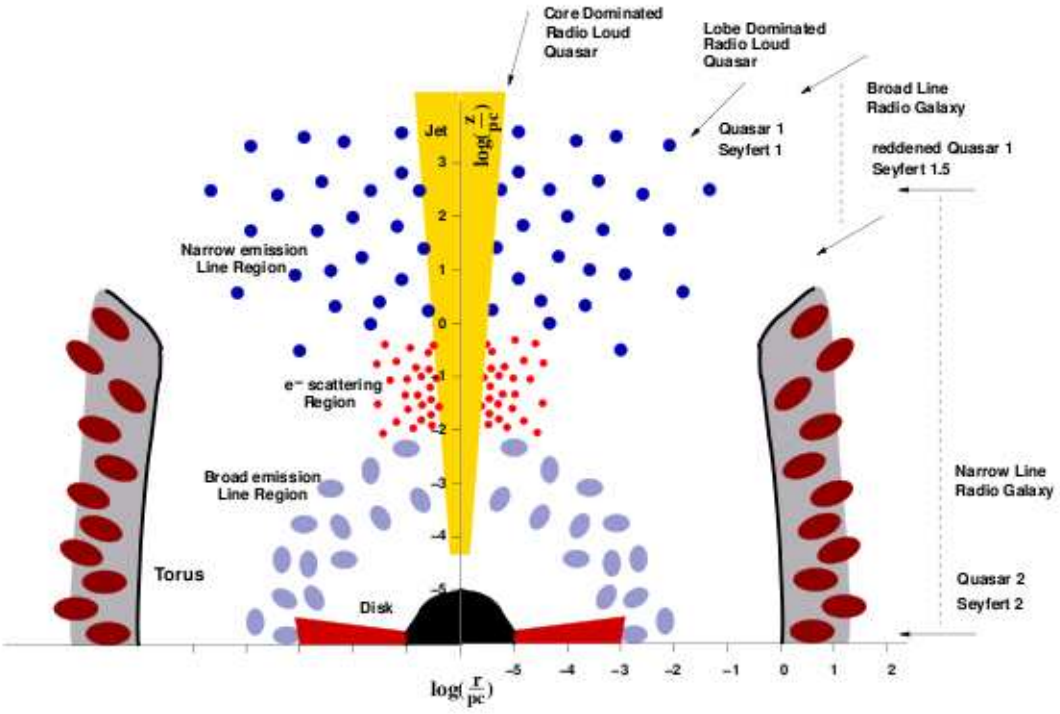

Figure 2.3: Morphology of AGN (Biermann2003 [57])

to the square of angular momentum of SMBH (Blandford1977 [62], Punsly1990 [192]). If so, this theory explains radio loud and radio quite jets.

2.4 Blazar

BL Lacs, FSRQs and OVVs are collectively called blazars. While FSRQ and OVV are characterized by emission lines, BL Lacs show very weak or no optical lines. The defining property of blazar is the existence of a jet in the line of sight to the observer. The major mechanism behind the origin of jets is believed to be Blandord-Znjek (BZ; Blandford1977 [62]) and Blandford-Payne (BP; Blandford1982 [60]) processes. In BZ process, the energy of jets is gained from the energy and angular momentum of the rotating black hole. In BP process, the jet energy is extracted from the disk matter by virtue of frozen poloidal magnetic field lines in the disk. The power carried by the relativistic jets and the power of accretion disk for a set of blazars has been studied (Maraschi2003 [168]). The results indicate that the power of jets and power of accretion disk is in the same order of magnitude for FSRQs, but the jet luminosity is higher than the disk luminosity in the case of BL Lacs. Blazars often show rapid variability: this can be explained by the comparatively smaller emission region.

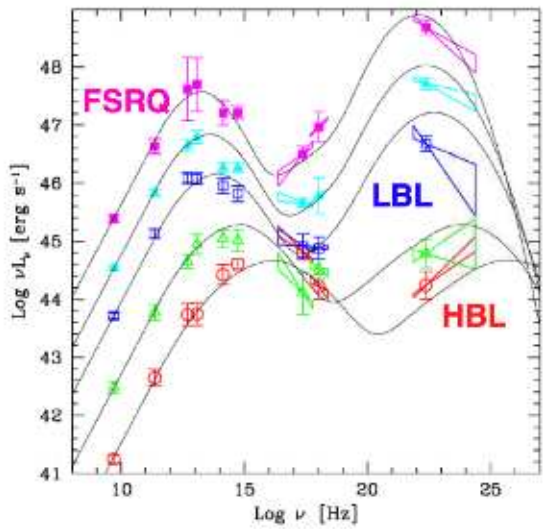

Figure 2.4: Blazar sequence (Ghisellini1998 [117]).

More SED characteristics have been revealed in the unification of the 126 observed

blazars SEDs (Fossati1998 [103]): (1) the low-energy bump of the blazar SED peaks at different frequencies, depending on the luminosity: more luminous objects peak at low frequencies; (2) there is a correlation between the low-energy peak and the high-energy peak of the SED; and (3) the luminosity ratio between the high and low-energy peaks increases with bolometric luminosity. However, according to Padovani2007 [180], there is no correlation between the low-energy peak of the SED and the luminosity: the correlation claimed by Fossati1998 [103] is a result of selection effect. The blazar sequence was modified theoretically by Ghisellini1998 [117]. This source model was later used by Costamante2002 [79] to predict the most probable sources to detect in VHE region. The current observation status of blazars agree with this prediction.

2.5 Emission mechanisms

In this subsection, I give a basic outline on fundamental radiation mechanisms in blazars. The radiations can be divided into thermal and non-thermal radiations. Thermal radiations plays an important role up to a few keV in the electromagnetic spectrum, while only non-thermal radiations contribute in higher energies.

2.5.1 Thermal emission

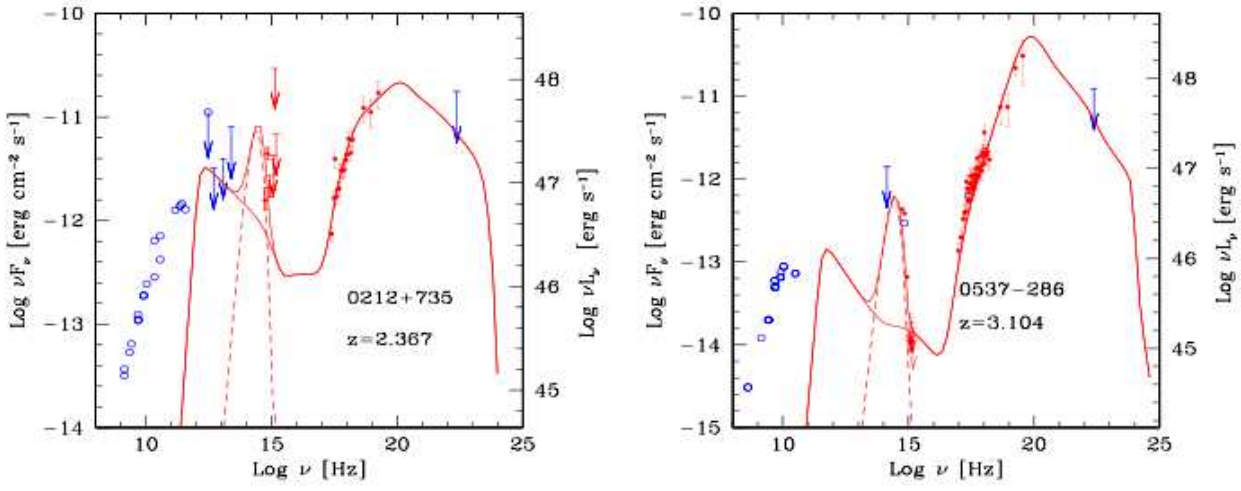

Figure 2.5: SED of two high redshift blazars, shows thermal emission component peaking at $\sim 3 \times 10^{14}$Hz (Sambruna2007 [204]).

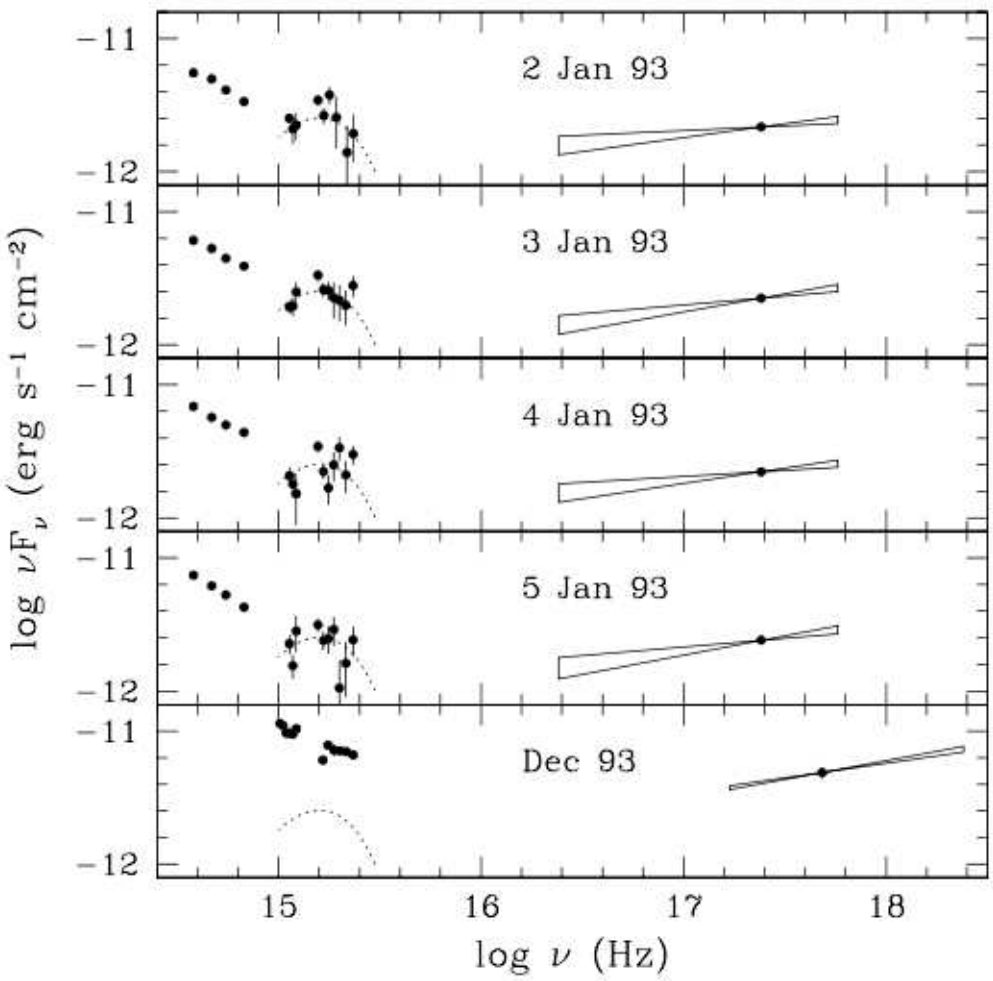

Figure 2.6: Simultaneous optical to X-ray SED of 3c 279 in different states. The dotted line shows the black body radiation model. This balckbody emission is clearly visible in the first four states, but it disappears in the fifth image when the non-thermal component of the SED goes to a higher state (Pian1999 [184]).

The radiation energy emitted thermally is characterized by black-body radiation. An ideal black body is an object which absorbs 100% of the radiation that impinges on it and does not reflect nor scatters any of it. The energy radiated in a particular temperature and frequency is given by Planck's formula

$$E(\nu, T) = \frac{8\pi\nu^3}{c^3} \frac{h}{e^{\frac{h\nu}{kT}} - 1}. \tag{2.5.1}$$

From this function, one can derive two properties of black body radiation. Upon integrat-

ing Planck's function over ν, the total power radiated from one surface unit of black body surface at a specific temperature.

$$P = \sigma T^4 \tag{2.5.2}$$

This is also called the Stefan-Boltzmann equation. Differentiating Plank's function gives,

$$\lambda T = \text{constant} \tag{2.5.3}$$

which is called Wien's displacement law. So, the thermal emission purely depends on the source temperature of the source. The effective blackbody temperature of high energy sources ranges from 3,000 K (red stars) up to 150,000 K (X-ray binaries); very hot objects produce thermal radiations up to a few keV in electromagnetic spectrum.

There are strong evidences of thermal emission in SEDs of AGN. Observation of AGN during the low state of emission will help to obtain clearer idea on thermal emissions from AGN. Thermal radiation peaking in the UV and optical band, is believed to emerge from the accretion disk, while the emission in IR band is believed to originate in the dusty molecular torus. The thermal emission component results in a narrow bump (mostly in UV band; Fig.2.5). Fe Kα line emission from two AGN (PKS 1136-135, PKS 1150+497) observed by *Chandra* satellite can be interpreted as thermal emission from an innermost stable orbits of the accretion disk (Sambruna2006 [203]). One of the strong evidences of the thermal emission is that the later's temporal variability pattern is entirely independent from the variability of the non-thermal emission: this is clearly visible when the source is in low state (Fig.2.6)

2.5.1.1 Thermal emission from accretion disk

Basic structure of AGN accretion disk has been provided by Blandford1985 [61] and Begelman1985 [54]. It is assumed that the luminous energy of AGN is provided by accretion, the energy of a particle at distance r from the central source is dissipated locally, and that the medium is optically thick. In this case the local emission can be approximated as blackbody. From virial theorem, half of gravitational potential energy is radiated away.

$$L = \frac{GM\dot{M}}{2r} = 2\pi r^2 \sigma T^4 \tag{2.5.4}$$

where T is the temperature, r is the radius of the disk and considering that the disk has two sides. This relation can be used to find the temperature,

$$T = \left(\frac{GM\dot{M}}{4\pi\sigma r^3}\right)^{\frac{1}{4}} \tag{2.5.5}$$

By considering that the energy is dissipated through viscosity, as the work is done by viscous torques,

$$T(r) \approx \left(\frac{3GM\dot{M}}{8\pi\sigma R_s^3}\right)^{\frac{1}{4}} \left(\frac{r}{R_s}\right)^{\frac{3}{4}} \tag{2.5.6}$$

When writing Schwarzchild radius (R_s) as $\frac{2GM}{c^2}$, and introducing the Eddington accretion rate, the above equation can be written as

$$T(r) \approx 6.3 \times 10^5 (\dot{M}/\dot{M}_E)^{1/4} M_8^{-1/4} \left(\frac{r}{R_s}\right)^{-3/4} \mathrm{K} \tag{2.5.7}$$

For a disk that is accreting at the Eddington rate, around a $10^8 \mathrm{M}_\odot$, the thermal emission frequency is maximized at $\nu_{\max} = \frac{2.8kT}{h} \approx 3.6 \times 10^{16}\,\mathrm{Hz}$, which corresponds at UV - soft X-ray band of the spectrum.

2.5.2 Non-thermal emission

Blazar emission is dominated by non-thermal mechanisms. In this section, I outline both leptonic and hadronic non-thermal processes.

2.5.2.1 Synchrotron mechanism

Relativistic charge particles produce synchrotron radiation while traversing a magnetic field B. The equation of motion of a single non-relativistic electron can be written as $\frac{\mathrm{d}p}{\mathrm{d}t} = qv \times B$, where $p = \gamma mv$. The correlated angular frequency of the charged particle is $\omega_B = \frac{qB}{c\,m}$. In relativistic case, the radiated power $P = \frac{2}{3}\frac{c^2\dot{v}^2}{c^3}$ (Larmor formula), can be written as:

$$P = 2\beta^2\gamma^2 c\sigma_T U_B < \sin^2(\alpha) > \tag{2.5.8}$$

where $U_B = \frac{B^2}{8\pi}$ is the magnetic energy density, σ_T is Thomson cross section and α is the angle between v and B, such that $< \sin^2\alpha >= \frac{2}{3}$. To find the total power radiated from an electron population described by a power law in energy

$$n(\gamma)\mathrm{d}\gamma = n_0\gamma^{-p}\mathrm{d}\gamma \tag{2.5.9}$$

one integrates the radiated power of a single electron over the electron population.

$$P_\nu = \int_1^\infty P(\nu) n(\gamma) \mathrm{d}\gamma \tag{2.5.10}$$

Combining Eq. 2.5.9 and Eq. 2.5.10 in Eq. 2.5.8 yields,

$$P_\nu = \int_1^\infty \frac{4}{3}\beta^2\gamma^2 c\sigma_T U_B \delta(\nu - \gamma^2\nu_L) n_0 \mathrm{d}\gamma \tag{2.5.11}$$

where, the δ-function shows that the electron with an energy γmc^2 blinks at a frequency $\gamma^2\nu_L$. Integrating the Eq. 2.5.11, we obtain the synchrotron luminosity.

$$P(\nu) = \frac{2}{3} c\,\sigma_T\, n_0 \frac{U_B}{\nu_L} \left(\frac{\nu}{\nu_L}\right)^{\frac{1-p}{2}} \tag{2.5.12}$$

Usually, in astrophysical environments, synchrotron radiation from electrons spans an energy range from radio to X-rays.

2.5.2.2 Inverse Compton mechanism

In the Inverse Compton (IC) scattering, relativistic electrons transfer part of their energy to photons by scattering. This is believed to be the major process in the production of γ-rays.

Let $\nu d\epsilon$ is the energy density of photons in an energy range $d\epsilon$. The total power radiated in electron's rest frame is,

$$\frac{\mathrm{d}E'}{\mathrm{d}t'} = c\sigma_T \int \epsilon_1^{'} \nu^{'} \mathrm{d}\epsilon^{'} \tag{2.5.13}$$

where $\nu^{'} d\epsilon^{'}$ is the energy density of incident photons in the rest frame. It can be assumed that the change in energy of the photon in the rest frame is negligible compared to the energy change in the lab frame, hence we can equate $\epsilon_1^{'} = \epsilon^{'}$. When converting the emitted power into observer's frame,

$$\frac{\mathrm{d}E}{\mathrm{d}t} = c\sigma_T\gamma^2 \int (1 - \beta\cos\theta)^2 \epsilon\nu \mathrm{d}\epsilon \tag{2.5.14}$$

Here we used $\epsilon^{'} = \epsilon\gamma(1-\beta\cos\theta)$. When applying the averaged value of $(1-\beta\cos\theta)^2$, which is $(1 + \frac{1}{3}\beta^2)$, we obtain,

$$\frac{\mathrm{d}E}{\mathrm{d}t} = c\sigma_T\gamma^2(1 + \frac{1}{3}\beta^2) U_{\mathrm{ph}} \tag{2.5.15}$$

where, $U_{ph} = \int \epsilon\nu \mathrm{d}\epsilon$ is the initial photon energy density. The rate of decrease of the total initial photon energy is

$$\frac{\mathrm{d}E}{\mathrm{d}t} = -\sigma_T C U_{\mathrm{ph}} \tag{2.5.16}$$

Thus the net power lost by the electron, and thereby converted into increased radiation is,

$$\frac{\mathrm{d}E_{\mathrm{rad}}}{\mathrm{d}t} = c\sigma_T U_{\mathrm{ph}} \left[\gamma^2 \left(1 + \frac{1}{3}\beta^2\right) - 1\right] \tag{2.5.17}$$

As $\gamma^2 - 1 = \gamma^2\beta^2$, we have

$$P_{\mathrm{Compton}} = \frac{4}{3} c\sigma_T \gamma^2 \beta^2 U_{\mathrm{ph}}. \tag{2.5.18}$$

To compute the total Compton power from a relativistic electron population $n(\gamma)$ one has to integrate the Compton power over $d\gamma$, as in the case of synchrotron radiation. If the electron population is described by $n_0\gamma^{-p}$ where $\gamma_{\mathrm{min}} < \gamma < \gamma_{\mathrm{max}}$ and we assume $\beta \sim 1$, the total power radiated can be written as,

$$P_{\mathrm{Compton}} = \frac{4}{3}\sigma_T c U_{\mathrm{ph}} N_0 (3-p)(\gamma_{\mathrm{max}}^{3-p} - \gamma_{\mathrm{min}}^{3-p}). \tag{2.5.19}$$

2.5.2.3 π^0 decay mechanism

When highly energetic protons interact with matter, they produce pions, which are the lightest mesons. Neutral Pions then mostly decay into γ-rays:

$$\pi^0 \rightarrow \gamma\gamma\,(99\%), \tag{2.5.20}$$

$$\pi^0 \rightarrow e^+ e^- \gamma\,(1\%). \tag{2.5.21}$$

Charged pions on the other hand eventually produce neutrinos:

$$\pi^{\pm} \rightarrow \mu^{\pm}\overline{\nu_\mu} \tag{2.5.22}$$

$$\mu^{\pm} \rightarrow e^{\pm}\nu_\mu\overline{\nu_e} \tag{2.5.23}$$

The differential spectrum of γ-rays in the annihilation of e^+ with Lorentz factor $\epsilon_p = E_p/m_e c^2$ on the ambient electrons of density n_e is described by:

$$q(\epsilon) = \frac{3{\sigma_T}^2 c n_e}{8\epsilon_p p_p} \left(\left(\frac{\epsilon_\gamma}{\epsilon_p + 1 - \epsilon_\gamma} + \frac{\epsilon_p + 1 - \epsilon_\gamma}{\epsilon_\gamma} \right) + 2\left(\frac{1}{\epsilon_\gamma} + \frac{1}{\epsilon_p + 1 - \epsilon_\gamma} \right) - \left(\frac{1}{\epsilon_\gamma} + \frac{1}{\epsilon_p + 1 - \epsilon_\gamma} \right)^2 \right.$$

(2.5.24)

where $\epsilon_p + 1 - P_p \leq 2\epsilon_\gamma \leq \epsilon_p + 1 + P_p$ and $P_p = \sqrt{{\epsilon_p}^2 - 1}$ is the dimensionless momentum of the positron.

For a power law spectrum of positrons $N_p \propto {\epsilon_p}^{\Gamma+1}$, the spectrum of annihilation radiation at $\epsilon_\gamma >> 1$ is basically a power law:

$$J_{ann}(\epsilon_\gamma) \propto {\epsilon_\gamma}^{-(\Gamma)} \left[ln\,(2\epsilon)_\gamma - 1 \right] \tag{2.5.25}$$

where Γ is the primary positron spectral index. So the spectrum of annihilation radiation is steeper than the spectrum of parent positrons.

2.6 Models

Remarkable systematic properties of AGN were noted in some early literature (Landau1986 [158], Sambruna1996 [202]). The SED of AGN is dominated by non-thermal continuum of jets. As the distribution is extended from radio to γ-rays, earlier observations were unable to provide a clear picture of SED, until the launch of EGRET satellite in 1991. EGRET provided crucial missing SED portions for several blazars. However, because of its relatively low sensitivity, EGRET was only able to detect blazars in high flaring state. So the results given by EGRET surveys are not homogeneous. However this issue was mildly solved by ordering the samples according to their radio luminosity (Fossati1998 [103]).

The SED of blazars generally contain two broad non-thermal continuum peaks. The high degree of polarization and spectral shapes indicate that the first bump arises from synchrotron emission. The second peak occurs in the multi-GeV band for HBLs and in the multi-MeV bands for LBLs. Even though there is a consensus that the first peak of SED arises from synchrotron radiation, there are variety of opinions on the nature of the second peak. Leptonic models favour IC up scattering of lower energy radiation by relativistic electron, while hadronic models prefer pion decay from pp interactions of energetic and ambient protons.

It is assumed that the low-energy peak of the SED is due to synchrotron radiation from a population of electrons moving in the local magnetic field, and the high energy peak is due to IC scattering of the synchrotron photons by the same population of electrons

(Maraschi1992 [167]). Fluctuations in parameters like magnetic field, Doppler factor or electron density can effect the synchrotron and IC fluxes. So the variations in low and high energy fluxes are correlated in most cases. Significant evidence of variability has been reported in the case of bright blazars like Mkn 421 (Buckley1996 [72]) and Mkn 501 (Catanese1997 [178]). However, uncorrelated spectral variability has also been observed in some blazars in a few cases (eg: orphan TeV flares and childless X-ray flares).

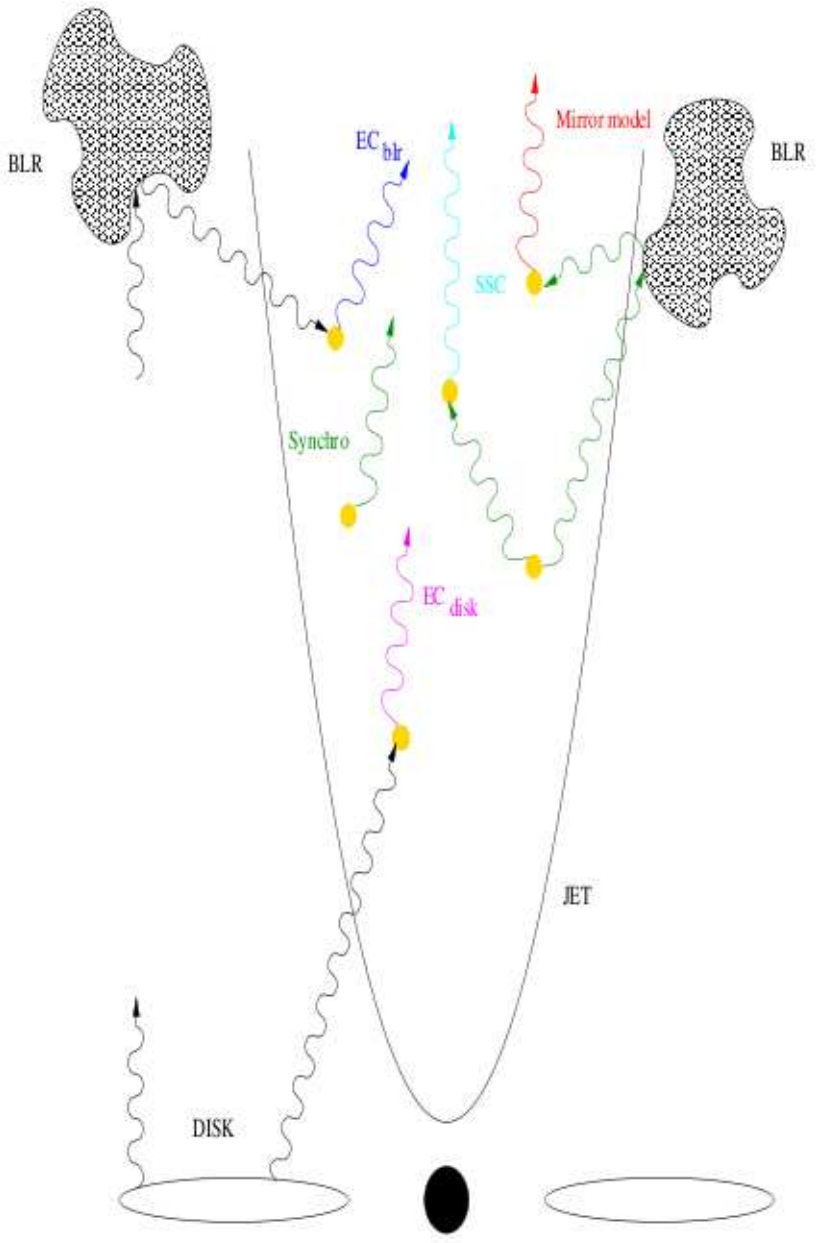

Figure 2.7: Sketch illustrating different leptonic emission models.

The difference between SSC and EC is based on the origin of photons available for IC scattering. According to EC models, these photons are external to the synchrotron-emitting region: they come from the central region of blazars, which are produced by the accretion disk or BLR region (Dermer1993 [84], Sikora1994 [214]). The direct emission of photons from the accretion disk to the central region of AGN, and undergo EC scattering is not very realistic because of the debeaming that the radiation would likely suffer, which would cause a strong depression in the reference frame of jets. However, the radiation from the disk towards the BLR, which can be reprocessed and beamed into the jet frame, can be an important contribution for EC. It was suggested that (Blazejowski2000 [67]) the NIR radiation emitted by the torus's dust could be an important IC contribution in the high energy processes in the 10 keV - 100 MeV band by EC process.

According to the Mirror model, the BLR is illuminated by the beamed jet emission provided that broad line clouds or scattering material exist in the vicinity of jet (Ghisellini1996 [116]). This beamed jet can be reflected back to the jet. The double change of frame provide a double beaming effect leading more than quadratic increase in γ-rays. The mirror model could be tested, even in the absence of VHE γ-ray observations, by monitoring the Lyα emission line from blazars. In principle, a limited number of clouds over a limited velocity range should respond simultaneously to the most rapidly varying (timescales of days) jet emission. However, no variations in the Lyα luminosity are seen in (IUE and HST data) spectra of 3C 279, as opposed to a large historical variability of the continuum, implying that a steady component, like an accretion disk rather than the jet beam, dominates the overall emission (Koratkar1998 [153]).

Relativistic hadrons undergo pp interaction with protons and pγ interaction with photons, which leads to the production of $e^{\pm}$ pairs or pions ($\pi^{\pm}$, π^0) and they decay into $e^{\pm}$, photons and neutrinos. $e^{\pm}$ can produce high-energy photons by synchrotron mechanisms, and the photons can undergo pair production, which again can produce photons. This mechanism is called Photon Induced Cascade (PIC). Electromagnetic cascades are initiated by photons from π^0 decay, $\pi^{\pm}$ decay, p-synchrotron photons and $\mu^{\pm}$-synchrotron photons. π^0 and $\pi^{\pm}$ cascades can produce featureless γ-ray spectra while proton and $\mu^{\pm}$ synchrotron photons are responsible for the double-bumped shape of the SED. Mannheim1993 [164] argues that TeV photons interact with UV/X-ray photons to

undergo PIC process. Successive population of lower-energy (GeV - MeV) pair produce the observable γ-rays. Hadronic models demand a high magnetic field ($\sim$10 times more than in leptonic models) in order to accelerate protons. Another hadronic model (Dar1997 [81]) suggest that the γ-rays are produced by the collision of jets with BLR at the line of sight. Intensive TeV γ-ray flares occur when BLR clouds cross the line of sight across the BH.

Hadronic models can not really explain the fast variability, due to their large mass compared to electrons, hence relative long cooling time of protons. The model can not explain the observed X-ray TeV variability in Mkn 421 and Mkn 501. Hadronic models uniquely predict the production of neutrinos, however neutrinos are yet to be detected from a blazar. Should they be detected, that would be a 'smoking gun' proof in favour of hadronic models, and that would also possibly explain the origin of UHE cosmic rays.

2.7 SSC model

SSC model is the simplest and the most popular emission model that adequately explains the SED of blazars. Detailed description on this model can be found in Tavecchio2001 [224], Kino2001 [152], Katarzynski2001 [147] and Finke2008 [98]. The model assumes the emission region as a sphere of radius R, threaded with a magnetic field B, relativistically moving at an angle θ with respect to the line of sight of the observer, such that the motion is described by bulk Lorentz factor Γ and Dopler factor $\delta = [\Gamma(1 - \beta\cos\theta)]^{-1}$. From the theory of synchrotron emission it is known that, a power law spectrum with slope α is produced by relativistic electron population of slope $n = 2\alpha + 1$. To produce the double power law shape of the synchrotron peak, a broken power law of electron energy distribution is assumed. If $\gamma_{\rm min}$ and $\gamma_{\rm max}$ are the minimum and maximum Lorenz factor, γ_b is the Lorenz factor at the break, n_1 and n_2 are the slope of the broken power law, and K is the normalization constant, the electron energy distribution can be described by,

$$N(\gamma) = \begin{cases} K\gamma^{-n_1} & ;\gamma_{\rm min} < \gamma < \gamma_b \\ K\gamma_b^{n_2-n_1}\gamma^{-n_2} & ;\gamma_b < \gamma < \gamma_{\rm max} \end{cases}$$

Thus, the parameters which describe the SSC model are $\gamma_{\rm min}$, γ_b, $\gamma_{\rm max}$, K, n_1, n_2, B and R. An SED fit can be fully described by 6 observational quantities: they are, the spectral slope bellow and above the synchrotron peak (α_1, α_2), synchrotron and IC peak (ν_s, ν_c) and their respective luminosities ($L_s(\nu_s)$, $L_c(\nu_c)$). An additional quantity can

obtained from the variability of the source with an assumption $R \leq ct_{var}\delta$.

The synchrotron frequency averaged over the spectral shape for an electron of Lorenz factor γ_b is given by,

$$\nu_s = 3.7\,10^6 {\gamma_b}^2 B\delta. \tag{2.7.26}$$

The peak luminosity is given by,

$$\nu_s L(\nu_s) = V\delta^4 \int N(\gamma)P(\gamma)d\gamma \simeq V\delta^4 N(\gamma_b)\gamma_b P_s(\gamma_b), \tag{2.7.27}$$

where, $V = \frac{4}{3}\pi R^3$ and $P_s(\gamma_b) = \frac{4}{3}\sigma_T c\frac{B^2}{8\pi}\gamma_b^2$, which is the synchrotron power of electrons at the break of electron energy population. Therefore, the peak synchrotron luminosity can be written as,

$$\nu_s L(\nu_s) \simeq \frac{8}{9}\sigma_T c B^2 R^3 K \gamma_b^{3-n_1}\delta^4. \tag{2.7.28}$$

The electrons producing the synchrotron emission, scatter with the synchrotron photons through IC process. The process must be distinguished according to the relevant cross section. Most of the scattering undergoes in Thomson regime and the rest occurs in Klein-Nishina(KN) regime. Since most of the synchrotron power is emitted at the frequency $\nu_s^{'} = \nu_s/\delta$ and most of the IC power is emitted by the electrons with Lorentz factor γ_b, the cross sections can be approximated by following equations.

$$\gamma_b \nu_s^{'} > \frac{m_e c^2}{h}\,(\text{Thomson}), \tag{2.7.29}$$

$$\gamma_b \nu_s^{'} < \frac{m_e c^2}{h}\,(\text{KN}). \tag{2.7.30}$$

At Thomson regime, the peak of the IC component is given by,

$$\nu_c = \frac{4}{3}\nu_s^{'}\gamma_b^2\delta. \tag{2.7.31}$$

From Eq. 2.7.24 and Eq. 2.7.29, one can obtain γ_b;

$$\gamma_b = \left(\frac{3\nu_c}{4\nu_s}\right)^2. \tag{2.7.32}$$

The peak IC luminosity can be written as

$$\nu_c L(\nu_c) \simeq V\delta^4 \int N(\gamma)P_c(\gamma)\mathrm{d}\gamma \simeq V\delta^4 N(\gamma_b)\gamma_b P_c(\gamma_b), \tag{2.7.33}$$

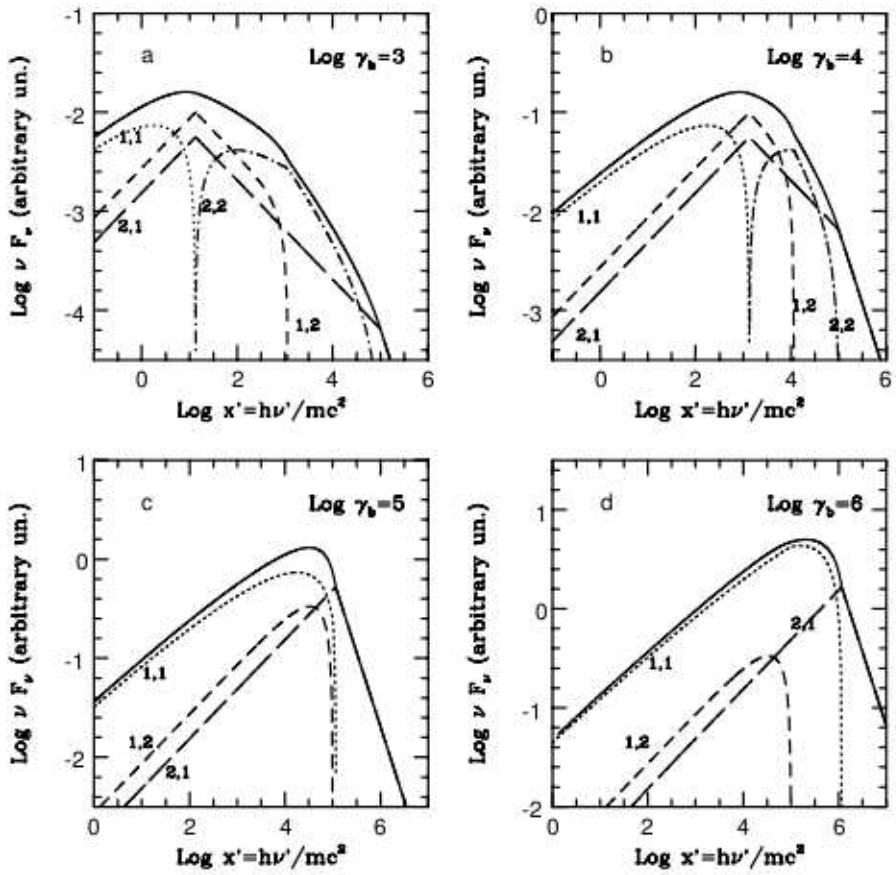

Figure 2.8: Four different integrals contributing to the SSC spectra. Doted line shows the contribution from low energy photons and low energy electrons, the short dashed line shows the contribution from the low energy electrons and high energy photons. The long dashed line represents the contribution from high energy electrons and low energy photons. The dot-dashed curve is due to high energy electrons and high energy photons.

where, $P_c(\gamma_b) = \frac{4}{3}\sigma_T c U'_{\rm syn}\gamma_b^2$ is the IC power of electrons at γ_b, in which the synchrotron energy density is $U'_{\rm syn} = L/4\pi R^2 c\delta^4$. Therefore,

$$\nu_c L(\nu_c) \simeq \frac{4}{3}\sigma_T c\gamma_b^3 N(\gamma_b) U'_{\rm syn} V\delta^4 \propto K^2 B^2 R^4 \delta^4 \gamma_b^{2(3-n_1)}. \tag{2.7.34}$$

In case of KN cross section, the full cross section can be approximated by a step function,

$$\sigma(\gamma,\nu) = \begin{cases} \sigma_T\,; \gamma\nu < \frac{3}{4}\frac{m_e c^2}{h} \\ 0\,; \gamma\nu > \frac{3}{4}\frac{m_e c^2}{h}. \end{cases}$$

An approximation for the peak frequency could be $\nu_c \sim \gamma_b m_e c^2 \delta$. A calculation assum-

ing KN cross section as a step function, and broken power law electron population, shows that ν_c can be better approximated by $\nu_c = g\gamma_b m_e c^2 \delta$, where g depends on the spectral slope. In KN regime, the luminosity can be calculated using substantially low synchrotron energy density compared to Thomson regime. The available synchrotron energy density in KN regime is,

$$U'_{\rm syn,avail} = \int_0^{\frac{3mc^2}{4h\gamma_b}} U'_{\rm syn}(\nu)\mathrm{d}\nu, \tag{2.7.35}$$

where, $U'_{\rm syn,avail}$ is the energy density seen by electrons at γ_b due to KN step approximation.

The general way to study the effect of Thomson and KN cross section, is to split the contribution of electrons bellow and above γ_b, and scattering photons bellow and above the break at ν'_s, such that $I_{1,1}, I_{1,2}, I_{2,1}, I_{2,2}$, where the first digit represents photon, the second one represents electrons, "1" represents low energy while "2" represents higher energy (See also Fig.2.8).

Other than the observable quantities used above, one can also use some additional quantities to constrain the model parameters, like the opacity of γ-rays against the absorption by pair production should be smaller than unity. Comparison between cooling and escape time can give another additional constraint.

2.8 Summary of observed AGN in VHE range

The first detected TeV emitter was Mkn 421 and Mkn 501, which are comparatively nearer objects. After the arrival of lower energy threshold instruments like MAGIC and HESS, more of these sources have been discovered. The list of VHE γ-ray emitters include 32 sources (Wagner2010 [242]). The majority of these sources are HBLs as expected. The remaining ones are: 5 LBLs, 2 QSO and 2 RGs. The current list of observed AGN can be found in Table 2.1. Note that the detection of VHE γ-ray from the vicinity of of 3C 66 A/B (MAGIC J0223+430) is not included in the table. It may be the RG, 3C 66B (Aliu2009 [46]). Also star burst galaxies and unknown γ-ray sources like VER J0521+211 (ATel 2260) are not included in the table.

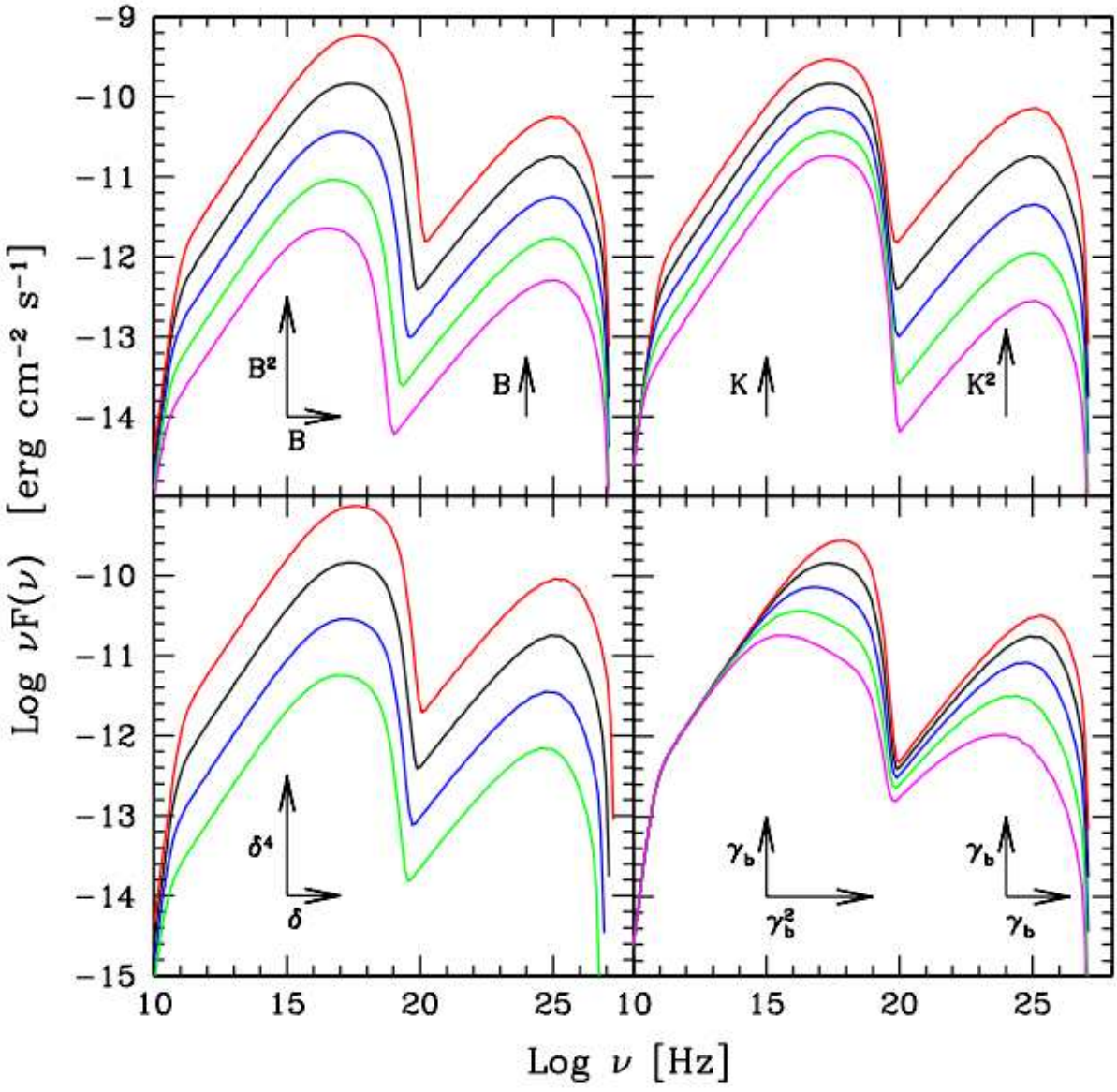

Figure 2.9: Effect of variation of parameters B, K, δ and γ_b. Top left, from top to bottom: B = 0.6, 0.3, 0.15, 0.075, 0.0375 G. Top right, from top to bottom: K = 4.2×10^3, 2. $\times10^3$, $1.05\times, 10^3$, 5×10^2, $2.5\times10^2\,\mathrm{cm}^{-3}$. Bottom left, from top to bottom: δ = 27,18, 12, 8. Bottom right, from top to bottom: γ_b =1.14×10^5, 5.7×10^4, 2.85×10^4, 1.42×10^4, 7.1×10^3.

Source	Class	Redshift	Instrument	Discovery
Mkn 421	HBL	0.030	Whipple	Punch1992 [190]
Mkn 501	HBL	0.034	Whipple	Quinn1996 [191]
1ES 2344+514	HBL	0.044	Whipple	Catanese1998 [74]
1ES 1959+650	HBL	0.047	Seven Tel. Array	Nishiyama1999 [179]
PKS 2155-304	HBL	0.116	Mark 6	Chadwick1999 [75]
1H 1426+428	HBL	0.129	Whipple	Horan2002 [142]
M 87	RG	0.0044	HEGRA	Aharonian2004a [11]
PKS 2005-489	HBL	0.071	HESS	Aharanian2005a [13]
1ES 1218+304	HBL	0.182	MAGIC	Albert2006c [32]
H 2356-309	HBL	0.165	HESS	Aharonian2006c [18]
1ES 1011-232	HBL	0.186	HESS	Aharonian2006c [18]
PG 1553+113	HBL	> 0.09	HESS	Aharonian2006d [19]
			MAGIC	Albert2007a [34]
Mkn 180	HBL	0.045	MAGIC	Albert2006d [33]
PKS 0548-322	HBL	0.069	HESS	Superina2007 [221]
BL Lac	LBL	0.069	MAGIC	Albert2007b [35]
1ES 0229+200	HBL	0.140	HESS	Aharonian2007c [22]
1ES 0347-121	HBL	0.185	HESS	Aharonian2007a [20]
1ES 1011+496	HBL	0.212	MAGIC	Albert2007 [36]
3C 279	QSO	0.536	MAGIC	Albert2008a [40]
RGB J0152+017	HBL	0.080	HESS	Aharonian2008a [24]
1ES 0806+524	HBL	0.138	VERITAS	Acciari2009 [8]
W Comae	LBL	0.102	VERITAS	Acciari2008 [6]
S5 0716+71	LBL	0.31	MAGIC	Anderhub2009 [49]
3C 66A	LBL	0.444	VERITAS	Acciari2009 [8]
Centarus A	RG	0.002	HESS	Aharonian2009a [26]
RGB J0710+591	HBL	0.125	VERITAS	ATel 1941
PKS 1424+240	LBL	>0.06	VERITAS	Atel 2084
RBS 0413	HBL	0.19	VERITAS	Atel 2272
1ES 0414+009	HBL	0.287	HESS and *Fermi*	ATel 2293
1ES 0502+675	HBL	0.341	VERITAS	ATel 2301
PKS 0447-439	HBL	0.2	HESS	ATel 2350
PKS 1510-089	QSO	0.36	HESS	Wagner2010 [240]

Table 2.1: TeV emitting AGN detected so far (updated March 2010).

3

The MAGIC Telescope

3.1 Introduction

The window of VHE γ-rays was opened after the birth of Imaging Air Cerenkov Telescope (IACT). The important features of Extended Air Showers (EAS) and the difference between γ/hadron induced showers are briefly described, followed by the details of the Major Atmospheric Gamma Imaging Cherenkov (MAGIC) Telescope.

3.2 Extended Atmospheric Showers (EAS)

Cosmic ray particles interact with atmospheric nuclei to produce secondary particles. The secondary particles further undergo the interaction process. As a result the number of secondary particles grow rapidly and evolve EAS. At some stage of this process, when the energy threshold of secondary particles is not enough to produce further secondary particles, the shower dies out. Different types of showers and the production mechanisms are briefly described.

3.2.1 γ-induced showers

γ-induced showers are produced by the interaction of high energy photons or electrons with atmospheric nuclei. The main processes in the development of showers are pair production and bremsstrahlung. The interaction length of an electron during bremsstrahlung is $X_0^e = 37\,\mathrm{g/cm^2}$ and that during pair production is $X_0^\gamma = 7/9 X_0^e$. Therefore the shape of γ-induced EAS is quite symmetric. The secondary electrons and photons loose energy after each steps of new particle production, and the shower slowly dies out after the critical

energy (~ 83 MeV), bellow which ionization of air molecules becomes the dominant process for electrons to loose energy.

The number of electrons N_e above the critical energy E_c is calculated by Greisen1966 [130].

$$N_e(t, E) = \frac{0.31}{\sqrt{\ln(E/E_c)}} \exp[t(1 - 1.5\ln(s))] \tag{3.2.1}$$

where E and E_c are the primary energy and critical energy of photon respectively, t is defined as X/X_0. X is slant depth which depends on the thickness of the atmosphere along the shower axis (for vertical showers $X = \int_h^\infty \rho_{(\mathrm{air})}(h)dh$). S, the shower age is defined as $S = \frac{3t}{t+2\ln(E/E_c)}$.

Differentiating Eq. 3.2.1 with respect to s, one can see that N_e increases with time, for $0 < s < 1$, reaches maximum at $s = 1$, and decreases with increasing s.

The height where number of particles in the shower is maximum is called shower maximum. The shower maximum for a γ-ray induced shower is between 7 - 13 km over the sea level.

3.2.2 Hadron-induced showers

When hadrons (generally protons) collide with atmospheric atmospheric nuclei, pions (90%) kaons and antriprotons (10%) are produced. The secondary hadrons again undergo interaction with atmospheric molecules to give rise to particle cascade. Particle energy bellow the threshold of pion production (~ 1 GeV), ionization process become dominant and hadronic shower gradually dies out. Among secondary particles: π^0 decay into photons and then the resulting photons produce e^+e^- induced showers. Charged pions and kaons, due to their high Lorentz factor, produce more secondary mesons. Due to small cross section and comparatively larger relativistic life time, muons reach at the ground level. Thus a large fraction of energy of primary particle is carried out by muons. Low energy muons, on the other hand produce electrons and positrons, which in turn give rise to EAS.

$$\begin{aligned}
\pi^+ &\rightarrow \mu^- \overline{\nu}_\mu \\
\pi^- &\rightarrow \mu^+ \nu_\mu \\
\pi^0 &\rightarrow \gamma\gamma \\
\mu^- &\rightarrow e^- \overline{\nu}_e \nu_\mu \\
\mu^+ &\rightarrow e^+ \nu_e \overline{\nu}_\mu
\end{aligned} \tag{3.2.2}$$

Due to comparatively higher transverse momentum of pions and kaons, the EAS produced by hadrons are wider. This is one of the important characteristics to differentiate between γ and hadron-induced showers.

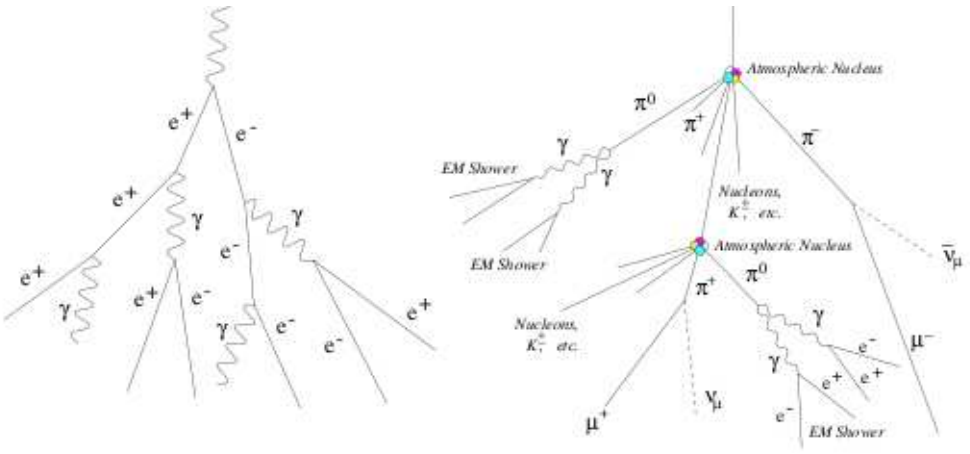

Figure 3.1: A drawing shows the difference between γ-induced shower (left) and hadron-induced shower (right).

3.3 Cherenkov radiation from EAS

When a charged particle traverse through a medium with a velocity greater than the velocity of light, it polarizes the medium. The net polarization of the medium remains along the trajectory of the particle, till the medium emits radiation to turn back to its ground state. The radiation is called Cherenkov radiation (Cherenkov1934 [77]; Frank1937 [105]). At relativistic speed of particles, the emitted radiation is in the form of shock waves,

in such a way that the wave front of the shock wave is propagated at a constant angle (Cherenkov angle; θ_c), with respect to the trajectory of the particle. From the geometric considerations in Fig.3.2,

$$\cos(\theta_c) = \frac{\Delta T\, c/n}{\Delta T\, \beta\, c} = \frac{1}{\beta n} \tag{3.3.3}$$

where $\beta = v/c$, v is the velocity of light in medium, and n is the refractive index of the medium. The maximum angle of Cherenkov radiation is achieved when $\beta \sim 1$.

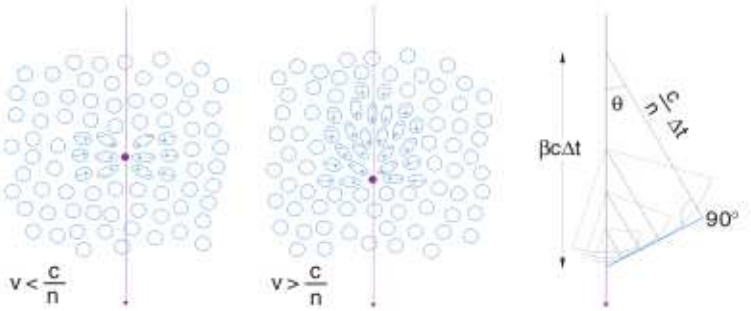

Figure 3.2: Left: When charged particles traveling in a medium with a higher spped than the speed of light it produce Cherenkov light. Right: Cherenkov waves using Huygens construction (Wagner2006 [239]).

The minimum energy for a charged particle to emit Cherenkov radiation is

$$E_{\rm th} = \frac{m_0 c^2}{\sqrt{1-\beta^2_{\rm min}}} = \frac{m_0 c^2}{\sqrt{1-\frac{1}{n^2}}} \tag{3.3.4}$$

where we used the logic $v > c/n$, to produce Cherenkov radiation. As the refractive index of medium depends on the density of medium, the threshold energy and emission angle of Cherenkov radiation varies upon the density of medium.

According to the simplified model of atmosphere which consider an exponential variation of atmospheric density with respect to height, the density can be written as,

$$\rho(h) = \rho_0 \exp\left(-\frac{h}{h_0}\right) \tag{3.3.5}$$

where ρ_0 is the density of air at sea level ($0.0013 \mathrm{g/cm}^3$) and $h_0 = 7.1$ km. Assuming refractive index linearly depends on the density of medium,

$$n(h) = 1 + n_h = 1 + n_0 \exp\left(-\frac{h}{h_0}\right) \tag{3.3.6}$$

where, n_0 is 2.9×10^{-4}. Using Eq. 3.3.6 in Eq. 3.3.3 and Eq. 3.3.4, and $n_h \ll 1$, the maximum emission angle and threshold energy of Cherenkov radiation can be written as,

$$\cos(\theta_c^{\max}) \simeq \sqrt{2n_h} \tag{3.3.7}$$

$$E_c^{th} \simeq \frac{m_0 c^2}{\sqrt{2n_h}} \tag{3.3.8}$$

The air density decreases with height, hence the optical density n_h. According to Eq. 3.3.7 and Eq. 3.3.8, E_c^{th} at 20 km altitude for muons, electrons and protons are 14 GeV, 67 GeV and 120 GeV respectively. The threshold energy decreases as particle passes through the atmosphere. Cherenkov light intensity depends also on the development of EAS. Shower maximum for γ-rays of different energy versus the atmospheric density is shown in Fig.3.3. The average Cherenkov angle averaged over altitude is $\sim 1.2^\circ$. The Cherenkov light from EAS illuminates the ground to form light ring. The circle becomes thicker and finally merge to a circle due to the difference in the density of atmosphere where the light is produced. The circularly illuminated cherenkov light on ground is called Cherenkov light pool. with an average radius of 120 m at an altitude of ~ 2 km. Lateral distribution of Cherenkov photon density is shown in Fig.3.4.

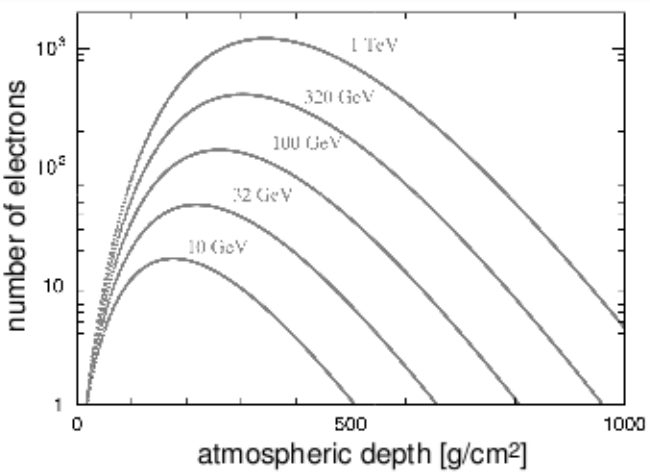

Figure 3.3: Shower maximum plotted against atmospheric density

The number of emitted Cherenkov photons for unit track length and wavelength for one particle can be written as (Yao2006 [248]):

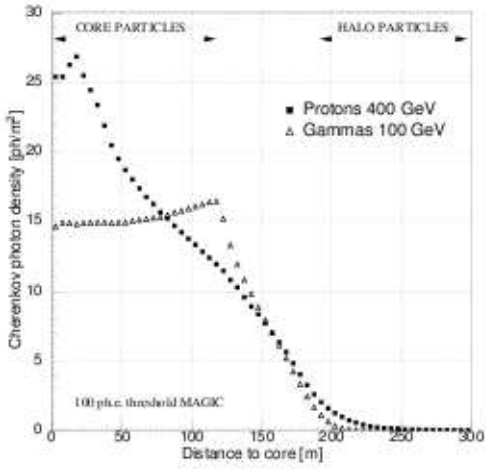

Figure 3.4: Lateral distribution of photon densities of γ-induced shower of 100 GeV and proton-induced shower of 400 GeV (Barrio1998 [52]).

$$\frac{\mathrm{d}^2 N}{\mathrm{d}x \mathrm{d}\lambda} \propto \frac{1}{\lambda^2} \tag{3.3.9}$$

This relation shows that most of the Cherenkov photons are in shorter wavelegths. The majority of photons are produced in UV range, and the number of photons decreases while increasing the λ. The Cherenkov photon spectrum is attenuated after interactions in the atmosphere. The major attenuation process is Rayleigh scattering, in which photons are scattered by small polarizable molecules which are smaller than the wavelength of photons. The cross section of this process is proportional to λ^4. Another important contribution is from Mie scattering, in which photons undergo scattering from small dust particles whose size is similar than the wavelegth of photons. Mie scattering cross section is proportional to $\lambda^{1.5}$. Absorption of cherenkov photons (mainly $\lambda < 290\,\mathrm{nm}$) by ozone molecule creates a major distortion in cherenkov photon spectrum. Absorption by H_2O and CO_2 has effects only $\lambda > 800\,\mathrm{nm}$, which is not important in observational point of view.

3.4 Imaging technique

Imaging Air Cherenkov Technique is the the most efficient way to detect VHE γ-rays. Imaging Air Cherenkov Telescope (IACT) collects the Cherenkov photons on its large mirror surface, and point them on a camera kept in the focal plane. The camera consists

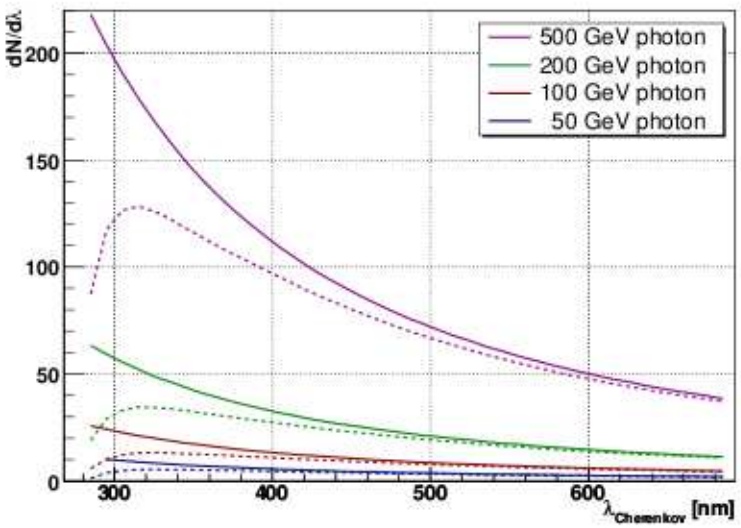

Figure 3.5: γ-induced Cherenkov photon spectrum at zenith angle $z = 0$. The solid line is the produced cherenkov spectrum at 10 km altitude, while the dotted line shows the detected photons at 2.2 km altitude, after attenuation (Wagner2006 [239]).

of PMTs to convert the photons into electric signal. The recorded event is the geometrical projection of atmospheric showers. Cherenkov photons emitted at different heights form images at different psotions of the camera. The image contains the information of longitudinal development of EAS from the number of photons and arrival time of the images. When the telescope is pointed towards a γ-ray object on the sky, images are formed near the camera center by the upper part of the shower, where the secondary particles are more energetic. The images of the photons from the lower part of the shower are formed away from the center of the camera.

The direction and energy of the primary photons (γ-ray) can be obtained from shower images. Total light contained on the camera is a measure of energy of the primary photon (6 photons roughly correspond 1 photo electron). Shape and orientation of the shower on the other hand help to understand the direction and the primary particle. Arrival direction of hadrons are uniformly distributed over the camera while the images of γ-induced EAS forms an elleptical shape and well corresponds to the position of the γ-ray point source on the sky. In order to achieve more accuracy in determining the arrival direction, pixel size of the camera should be smaller, depending on the optical point spread function (PSF) of

the telescope.

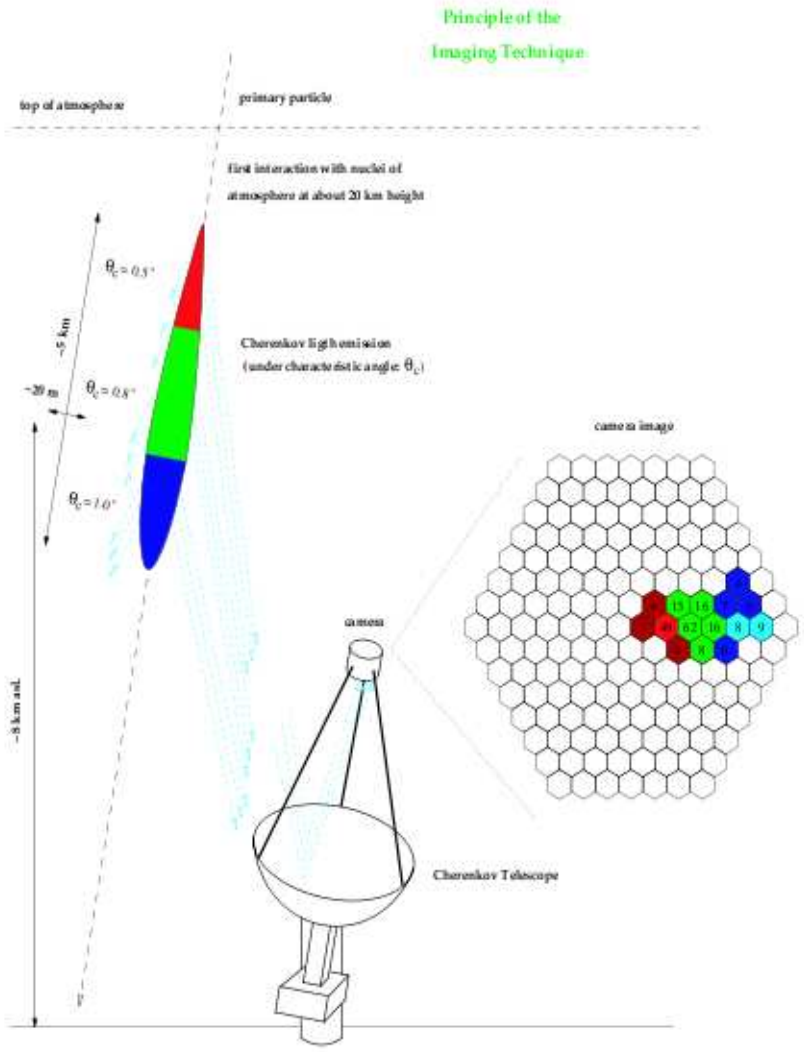

Figure 3.6: A sketch showing the immaging technique used in IACTs.

The energy threshold of an IACT is defined by:

$$E_{\rm th} \propto \sqrt{\frac{B\Omega t}{\epsilon A}} \tag{3.4.10}$$

where B is night sky background, Ω is the solid angle on the sky subtended by the mirror, t is the integration time of signals, ϵ is the efficiency of photon collection, and A is the collection area of the mirror. According to this equation, it is clear that the energy threshold can be lowered by increasing the photon collection efficiency of the photo sensor,

collection area of the mirror, minimizing the night sky back ground (galactic plane observations or moon light observations results in higher background), field of view of pixels and integration time.

The first detection of a γ-ray source using an IACT, was achieved in 1989. Whipple telescope observation of Crab Nebula resulted in 9 σ detection of the source (Weekes1989 [243]).

3.5 The MAGIC Telescope

γ-ray observations in the energy range of 50-300 GeV was left unexplored because the range is too high for satellite experiments, at the same time too low for IACTs to detect a significant amount of photons. The MAGIC telescope is a result of the quest of decreasing the lower energy threshold of IACT in order to extend the observation to the unexplored part of electromagnetic spectrum. It is the most recent generation IACT in the world. MAGIC is located at La Palma, Canarian Islands in Spain (28.3°N, 17.8°W, 2240 m a.s.l). The site, which is owned by Instituto de Astrofisica de Canarias, at the Observatario del Roque de los Muchachos (ORM) is one of the ideal places for astronomical observations. The low energy threshold of the instrument is 50 GeV (25 GeV with a special trigger set up called sum-trigger). Together with other IACTs and satellite born experiments like *Fermi* and AGILE, MAGIC is exploring a window of universe which is decisive for several important Physics goals.

The important parts of subsystems of the telescope are followed.

3.6 Telescope structure and drive system

One of the main goals of MAGIC telescope is to point the telescope at any direction of the sky in less possible time. This is very important for GRB studies (where the major emission occurs in the first few minutes). To reach this goal the weight of the telescope structure should be limited. Lower weight was achieved by using light weight carbon fiber tubes. The maximum repositioning time of the telescope is 100s with an average repositioning time of $\sim$ 30s.

In order to minimize the effect of night sky background, it is important to minimize

Figure 3.7: MAGIC Telescope located in Roque de los Muchachos, La Palma.

the spread of arrival time of showers on the camera. To achieve this goal, the reflector structure was made in parabolic shape. The ratio of focal length and diameter (f/D) is around 1, which ensures the optical aberrations of the shower image is less than a pixel size.

The telescope has an azimuth and a zenith axes, in order to point any part of the sky. The drive system includes three motors of 11 kW of power, two for azimuth and one for zenith movement. The allowed range of movement in azimuth is $\phi = -90°$ - $+318°$, and in zenith is $\theta = +105°$ - $-70°$. The angular position of the telescope is measured by 14-bit shaft encoders with a precision of $0.02°$. One of them is in azimuth axis while the other two are in zenith axis. During slewing relative distance of the new position is calculated and commands are sent to the micro controllers. The procedure repeats at least ten times, if the precision in positioning was not achieved in the previous trial. While tracking a source, tracking loop algorithm transforms celestial coordinates of the target (RA, DEC) into telescope coordinates.

3.7 Reflector and Active Mirror Control

As mentioned before, it is essential to collect more photons to lower the energy threshold with high sensitivity. 17 m diameter reflector surface (with a surface area 240 m^2) makes MAGIC as the largest single dish Cherenkov telescope in the world. The reflector is composed of 965 mirror elements of $49.5 \times 49.5\,cm^2$ area each. The curvature of each single mirror is spherical. 892 of them are grouped in 4-element panels while the rest in 3-element panels at the reflector dish. Each mirror panel has a heating element to prevent dew or ice formation.

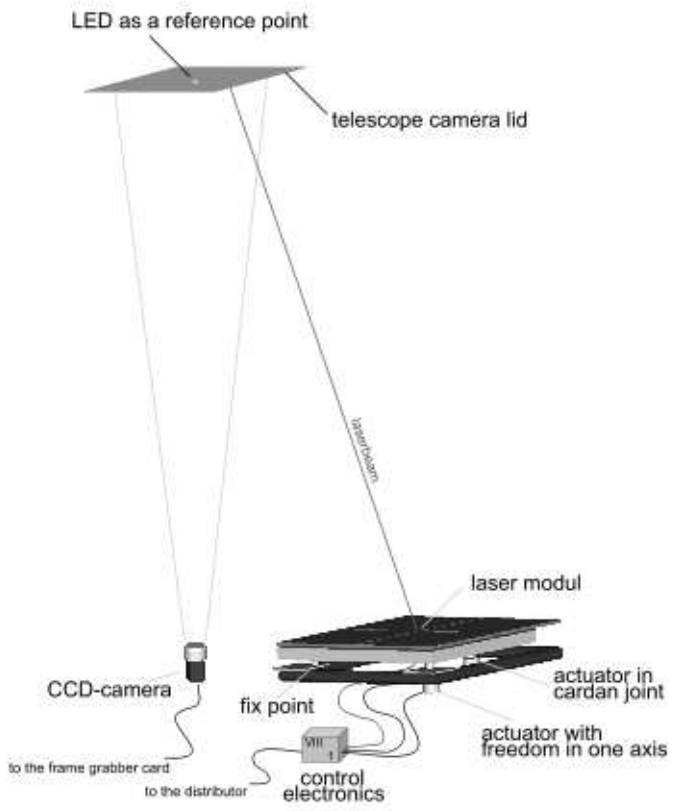

Figure 3.8: Schematic drawing of AMC.

An aluminum box filled by an aluminum honeycomb structure work as the base of each mirror element. An AlMgSi alloy is glued in front side of the structure. This part is polished and shaped with diamond milling and coated by quartz in order to protect from scratches. Mean reflectivity of the MAGIC mirrors are 85% in $\sim$ 200 - 650 nm range.

Even though the frame is rigid, the mirrors may suffer from distortions due to gravitation. Another technical innovation is used to overcome this problem, which is called Active Mirror Control (AMC; Garczaczyk2005 [111]). AMC consist of two actuators for each mirror panel and a laser pointer. When the laser is switched on, it creates an image on the camera wall (camera is closed during this operation). This image has been detected by a CCD camera (called AMC camera), to determine the alignment of mirrors. The panel is adjusted by motors till the reflector point to the direction of the center of the camera. This operation is done every night before starting observations and take around 5-10 minutes. In order to save time while changing the source of observation during night, a look up table (LUT) is used, to allaign the panel in each zenith angle. LUT is prepared by pointing the telescope to a star. AMC camera can identify the reflected star light on the camera cover. The advantage of this method is that this operation takes only less time and can be performed during the repsotioning time of the telescope.

3.8 Camera

An ideal IACT camera should be able to record high energy as well as low energy events. As high energy events produce extended images, it is important that the field of view (FOV) of camera should be larger enough to capture the whole event. Lower images produced by low energy events require small pixel size. A large FOV together with smaller pixels ensures a better γ/hadron separation.

Several PMTs (which will be replaced by Hybrid Photo Detectors in a later stage of the experiment) are used to convert collected photons into electric signals in the MAGIC camera. The lay out of the Camera is shown in Fig.3.9. Two different kind of pixels are used after the compromise between telescope performance and the cost. Out of 576 pixels, 396 inner pixels are of finer size with 0.1° angular diameter which corresponds to a FOV of 2.1°, and the rest are bigger pixels of 0.2° angular diameter which corresponds to FOV of 3.5°. For the outer pixels, no low energy showers are expected.

MAGIC PMTs have a Quantum Efficiency (QE) of $\sim$ 25% in $\sim$ 350-450 nm range of photons. A further improvement is achieved in QE (upto 30%) with a light a light scattering lacquer mixed together with a wavelength shifter (Paneque2004 [182]). The photocathode of PMTs are of bialkali with enhanced sensitivity in the green band of

electromagnetic spectrum.

Figure 3.9: A photograph of MAGIC camera.

In order to increase the efficiency of photon collection, light guiders are used in front of each PMTs. Light concentrators increases the active area of PMTs and decreases the light coming from outside the incident angle defined by the edge of mirror surface. Light guiders are made of plastic material covered by almuminized Maylar foil of 85% reflectivity. They maximize the probability of photons to double cross the PMT cathode. It has been found that the usage of light guiders increased the efficiency of the camera by about 50%. In order to protect the camera from the external environment a 2 mm thick UV transmitting plexiglass is used, with an overall transmission of 92%.

For the moonlight observations the gain of the PMTs is adjusted as 5×10^4, instead of standard gain of $\sim 10^6$-10^7. This reduces the current in the last dynode of the PMTs, and observation of high night sky background (moonlight) became possible. MAGIC can observe sources with an angular distance $> 50^\circ$ to the moon, up to three days before and after full moon. In order to compensate with the aging and the possible degradation of PMTs, a readjustment of High Voltages is done a few times in an year.

To provide an ideal and homogenous temperature, the camera wall is equipped with water cooling system. It is also advised not to operate the camera in unsuitable weather conditions like high brightness, wind or humidity, in order to avoid the possible damage of the camera.

3.9 Signal transmission

The MAGIC read out system is placed in the counting house which is ~ 150 m far from the telescope. In order to transfer the signal from PMT to the counting house optical fibers are used. The electric signal from PMTs is AC coupled with a gain of ~ 6. The amplified signal is converted back to optical signal using fast current driver amplifiers coupled to a vertical cavity surface emitting laser diodes (VCSELs). The analogue optical signal is then transferred into optical fibers. Optical fibers ensures that there is no cross talk between neighbouring channels, avoid electro magnetic distortions and almost no signal attenuation. Optical fibers are light weight, which is another advantage of using them.

3.10 Receiver, Trigger and Data acquisition

The signals from the optical fiber are converted to electric signals, using photo diodes inside the receiver board. The electric pulses are then duplicated: One signal goes to the trigger system while the other to the data acquisition (DAQ) system.

It is not required to store the continuous data which are not necessarily the γ-ray event. So, a trigger system filter out unwanted events. The trigger region of MAGIC camera includes only 325 innermost pixels. They are grouped into 19 macrocells as shown in the Fig.3.10. The trigger system has three levels. Level 0 Trigger (L0T) is a discriminator in the single signal pixels. The threshold of this descriminator can be set according to the light conditions (eg: moon light, galactic region, extragalactic region). After L0T, the signal splits into two. One part goes to Level 1 Trigger (L1T), while the other one for Level 2 Trigger (L2T). For L1T, a next neighbour logic is used. According to this logic at least 4 neighbouring pixels (4NN) should have a signal in a few nano seconds. This is mainly to suppress the hadron-induced triggers. The number of neighbouring pixels can be adjusted (For eg: 3NN or 5NN), however it has been found that 4NN provides better efficiency. Level 2 Trigger (L2T) was planned for online pattern recognition. However L2T is not yet used in MAGIC.

The second part of the analog signal from the receiver board goes to analog to digital converter. A dual gain 200 MSamples/s 8-bit FADC system was used. The disadvantage of this converter is that the process is rather slow compared to the response time of

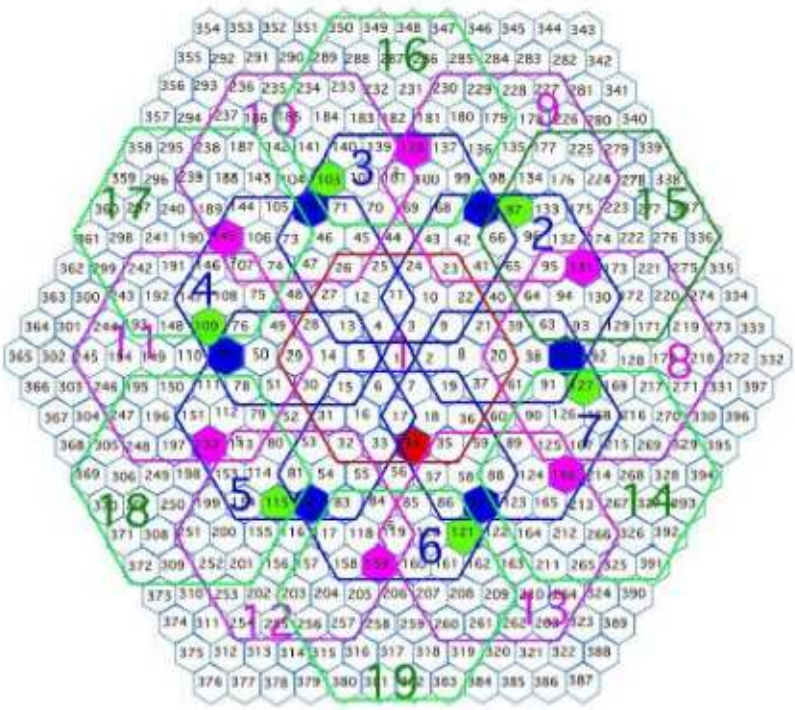

Figure 3.10: MAGIC trigger region with 19 macrosells.

γ-ray signal which is usually $\sim$2 ns pulses. A faster readout helps to reduce night sky background and a better γ/hadron separation. The MAGIC collaboration started using a faster readout called MUX FADCs (2 Gsamples/s), since 2007.

The MUX readout system uses two MUX FADCs to digitalize 16 readout channels. This is done by delaying analog signals by 40 ns with respect to the previous channel. The signals are then electrically multiplexed and sent to FADC. A schematic diagram of MUX FADCs is shown in Fig.3.11. More on MUX FADC can be found at (Goebel2007 [128])

3.11 Calibration

In order to convert FADC charges into number of photo electrons (phe), and FADC timing into absolute signal timing, an optical calibration system is used. The calibration box is mounted on the middle of the mirror dish. It consists of 64 LEDs emitting photons of λ 370 nm, 460 nm and 520 nm, such that they illuminate the camera in a certain frequency.

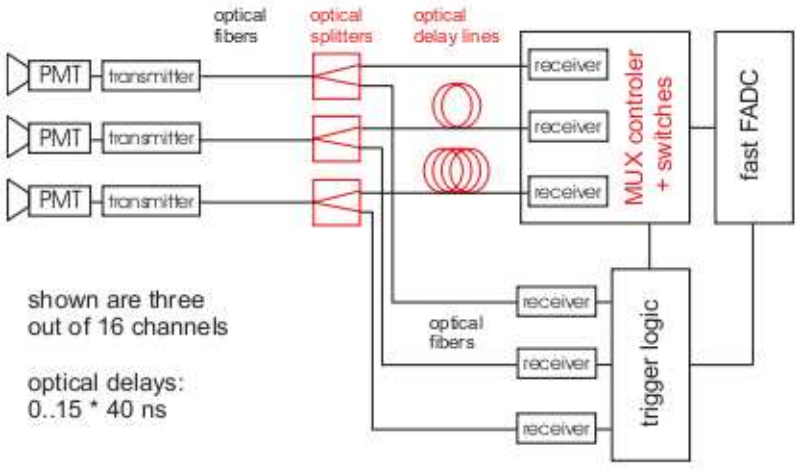

Figure 3.11: A schematic diagram of MUX read-out system.

The intensity of light can be varied from 4 - 700 phe per inner pixel. This set-up also allows to check the linearity of the readout chain.

The calibration of the signals recorded by pixel of the camera is performed by a relative calibration and an absolute calibration. Relative calibration is to check the responses of each channel by comparing the same input signal. The different response in different channels may arises from the slight variations of QE of PMTs, photo collection efficiency or the difference in VCSELs.

To convert FADC charge and time information into physical quantities absolute calibration is used. Three methods are used for this purpose. In Blind pixel method (Blind pixel are the three pixels placed in the outermost ring of the camera with a filter of factor 100 in the PMT range wavelengths), the QE of the blind pixel PMTs are accurately measured. By analyzing the phe spectrum of blind pixels and knowing the QE of the pixel, the mean number of photons from the calibration pulse can be calculated. Another method is by using Positive-Intrinsic-Negative (PIN) diode, which is a photo diode whose conductivity depends on the intensity and wavelength of the incident light. The calibrated PIN diode is kept 110 cm from the calibration box. The mean number of photons emitted from the calibration box can be estimated from the number phe generated by the PIN diode. Another conventional method used in Cerenkov telescopes is F-factor method. The method is based on the basic characteristic principle of PMTs, which is, excess noise is

linearly depends on the initial number of phe that produces the PMT output signal pulse. F-factor is therefore defined as signal to noise ratio at input level to that of output level. From the knowledge of the F-factor of the PMTs (1.15 ± 0.02; Paneque2003 [181]) and the analysis of the output signal of each pixel, average number of input phe.

3.12 MAGIC observation modes and Data

MAGIC telescope can observe a source in two different modes. In ON-OFF mode, the telescope points to the source (ON data) and then the telescope points to a dark part of sky where there is no known γ-ray sources (OFF data), in similar observational conditions. In Wobble mode the telescope points to a direction 0.4° away from the camera center, and the symmetric part of the camera can be considered as anti-source position. Source and anit-source position is wobbled in each 20 minutes. While the sensitivity for Wobble mode is 20% less than that of ON-OFF mode (Bretz2005 [70]) , observation time can be significantly reduced, as the Wobble mod does not require any OFF data.

MAGIC data are recorded as three different labels - Calibration, pedestal and data runs. Calibration runs are taken using calibration pulses from 10 UV LEDs. Calibration runs are used to calculate the conversion factor from FADC counts into the number of phe and arrival time offsets. During pedestal runs, the readout is triggered artificially with 500 Hz to calculate the offset, which has to subtracted from the signal. A dedicated calibration and pedestal runs are taken before the data run starts. A data run contains cosmic events and interleaved calibration events of 50 Hz frequency.

3.13 Dailycheck

The quality of the data depends on the good functioning of the telescope subsytems. Therefore it is important to check the performance of subsystems every day after data taking. The program is automatically executed every morning to extract information from subsystems through the central control, and the output plots were checked by human till May 2008.

3.13.1 Automatic dailycheck

Automatic check (autocheck) of dailycheck plots were introduced to increase the efficiency in time and accuracy.

The subsystem check of autocheck program includes:

1. The position of the telescope in both axes, which is obtained by the data from shaft encoders. This check gives an idea about the working of the drive system.

2. Parameters like PMT voltages, camera lids, cooling system, PMT direct currents and camera sentinel are checked in order to make sure the working of camera.

3. Camera high voltage, current, the power supply of the 5th and 6th PMT dynodes, the discrimination threshold (DT; which depends on the light condition of the observing region of the sky) are plotted against time.

4. Check on trigger system, which is achieved by checking the first and second level of trigger rates versus zenith angle and RMS of individual pixel rate (IPR). This data also helps to check if DTs were set correctly.

5. Star guider check which can spot mispointing problems. Mispointing is determined by comparing the position of bright stars around the observing region of the sky and the reference LEDs on the camera.

6. Weather station checks that make sure all data were taken in ideal condition of temperature, relative humidity and wind speed.

7. The time difference check between the rubedium clock and UTC time which is received by a radio receiver, make sure the magic data are labelled with right time stamp.

8. Receiver temperature check was introduced because high temperature of receivers may effect the data quality. Moreover fast variations of the temperature causes variations in signal charges.

Other than the performance of subsystems, the dailycheck program also check MUX Daq statistics files. The first two checks include mean pixel charge and time for each pixel

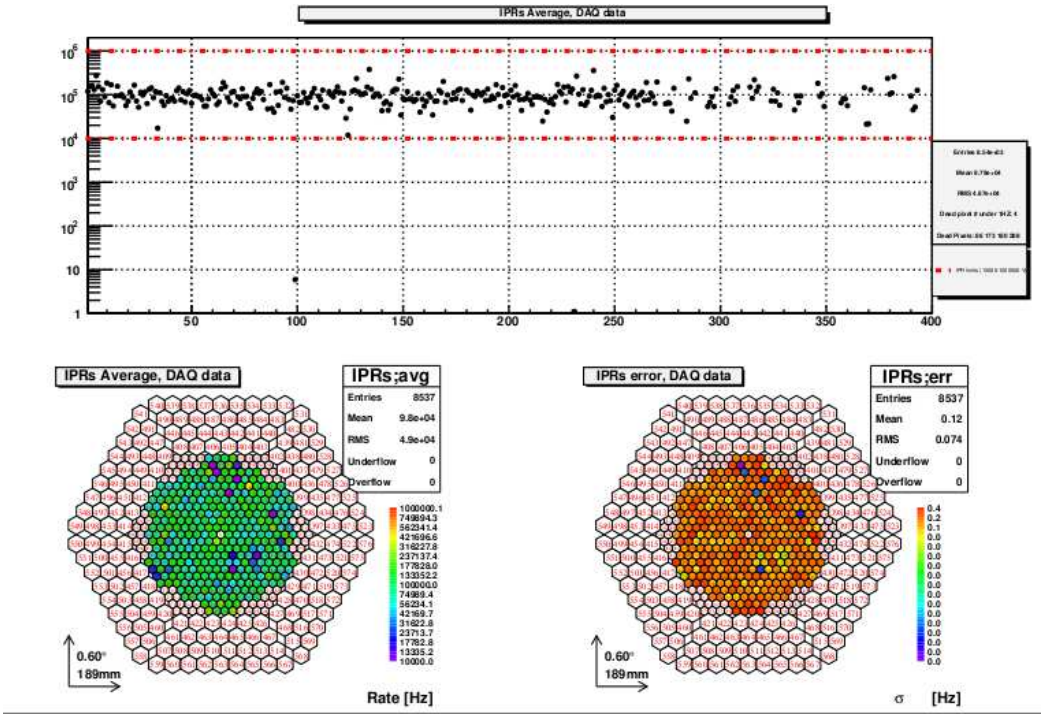

Figure 3.12: An example for the dailycheck plots. These plots refers to the IPRC check.

during calibration and data run of the telescope. Arrival time of signal and calibration events in units of FADC slices is to understand whether some part of data had arrived too early or too late, which will result in non-saving the peak part of the digital signal. Number of bad pixels during one night of observation gives an idea about the quality of data. A pixel is considered as bad pixel if (1) If the calibration signal contains only pedastals. This can be a dead pixel. (2) If signal comes too early or too late, such that FADC window can not extract the pulse. (3) If the calculated number of phe have high deviation, which may arise from the malfunctioning of the channel. (4) The mean value of charge from calibration pixel is very different from the mean values of all pixels. Following these criteria, it is normal to have 20-30 bad pixels every night.

Autocheck program checks if the parameters are inside the pre defined limits. In case the parameters are outside limit, the program calculates the total data taking time in which the parameters are outside the limit. The program creates the text file, which is used by a php parser in order to fill the web form of dailycheck questions. After filling the form php report builder sends the report to a selected mailing list of the magic collaboration.

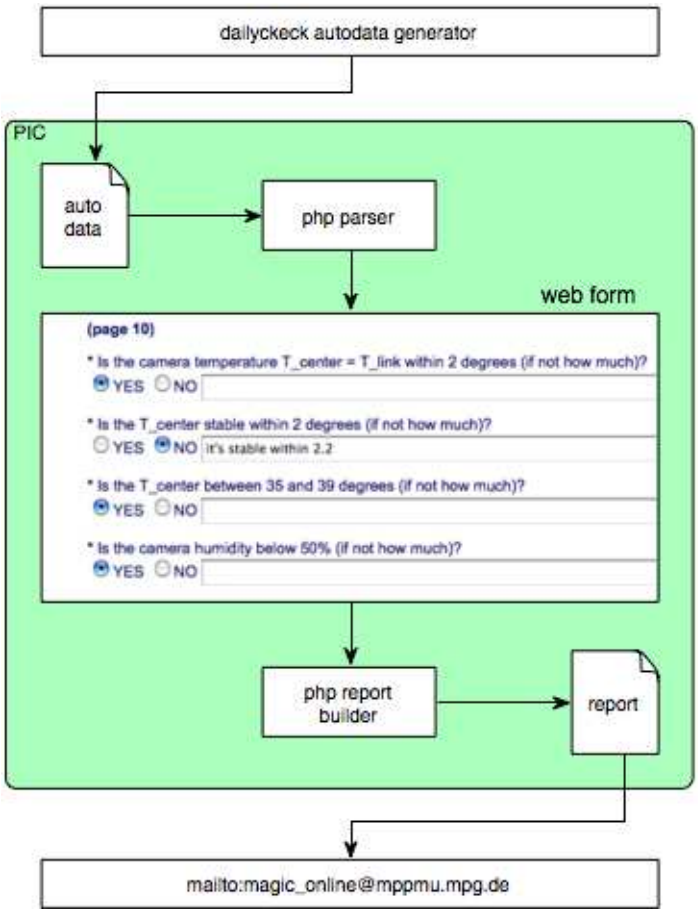

Figure 3.13: Automatic dailycheck box diagram.

3.14 MAGIC stereo system

The basic principle of stereo IACT system is to place two telescopes in the light pool of EAS and operate them as a system. It gives rise to an additional possibility in trigger system. The trigger will be created only when two of the telescopes have a signal over a threshold. When the two telescopes are inside a light pool, the two images can be compared to construct the impact point of the shower, which in turn improves the energy reconstruction and the source position. The resulting γ/hadron separation can improve the sensitivity of the telescope.

The construction of the second telescope of MAGIC collaboration was finished in 2008, and commissioned in 2009. The two telescopes can be operated independently.

The structure of second telescope is almost identical to the first one. The telescope

structure and AMC has only marginal improvement compared to the first one. For the reflecting surface, $1\,\mathrm{m}^2$ mirrors were developed instead of $0.25\,\mathrm{m}^2$ mirrors in MAGIC I.

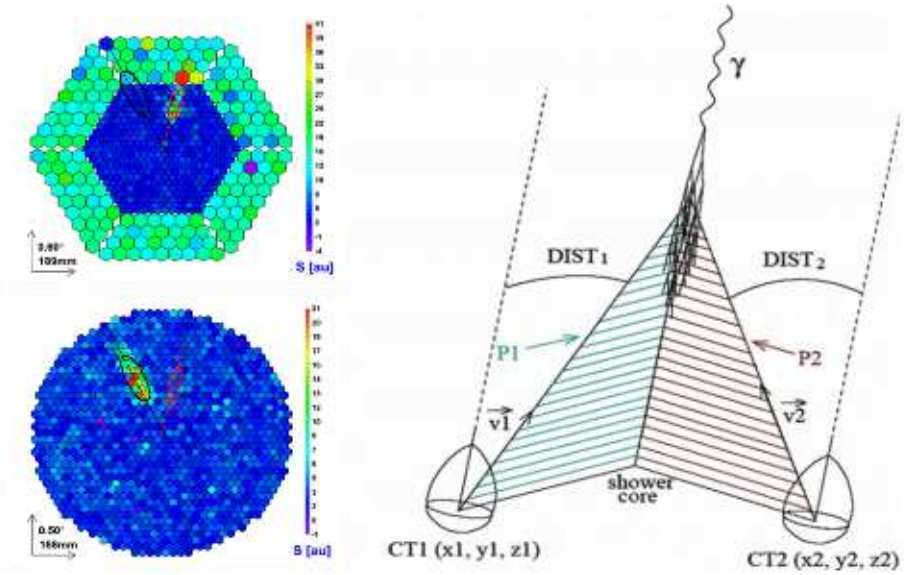

Figure 3.14: Images formed on MAGIC I and MAGIC II camera. The incoming direction reconstruction and the core distance are obtained from the two images.

The main improvement with respect to the first telescope is in the camera and read out system. MAGIC II camera has only smaller 1039 pixels instead of smaller inner pixels and larger outer pixels in MAGIC I. However, total field of view of the camera is 3.5° for both telescopes. Each seven pixels are grouped into one cluster. Clusters are inserted into holes between two cooling plates where cooling liquid is running through the pipes in order to stabilize the temperature of the camera. The modular design allows easier maintenance of the camera. Increased QE PMTs are used in the first phase, which will be replaced by Hybrid Photo Detectors (HPDs) in the second stage.

The fast Cherenkov pulses are sampled by a low-power Domino Ring Sampler chips and temporarily stored in an array of 1024 capacitors. Signals are sampled at the same speed of MAGIC I read out system (2 GSamples/s). They are then digitalized by a 12-bit resolution by an external ADC readout at a speed of 40 MHz.

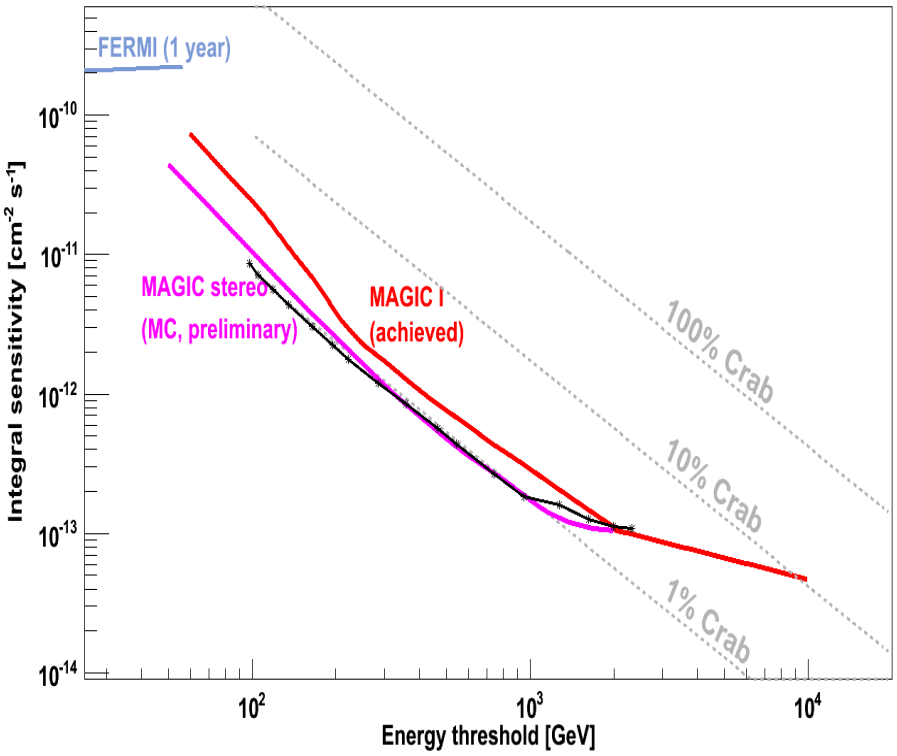

Figure 3.15: The comparison of sensitivities of MAGIC I (achieved), MAGIC stereo (MC). MAGIC stereo (achieved) is shown in black line.

4

Analysis of the MAGIC data

4.1 Introduction

As described in the previous chapter, IACT collects Cherenkov photons from EAS induced by γs and hadrons, together with massive amount of Night Sky Background (NSB). The preliminary goals of analysis of an IACT data are: to distinguish γ like events from the whole data, to determine the incoming direction of primary γ-rays, and to determine the energy of γ events, to calculate the γ-ray energy spectrum of the source. MAGIC Collaboration uses a dedicated software called MAGIC Analysis and Reconstruction Software (MARS) which is a ROOT [200] based C++ code.

4.2 Charge and arrival time reconstruction

The charge and arrival time of the Cherenkov photons at each pixel of the camera have to be determined. MAGIC telescope uses 2 GHz FADC system to sample photon signals. FADC contents are interpolated from the signal extraction method, using a cubic spline algorithm (Albert2008b [41]). The position of the maximum of the interpolation function is then estimated by the algorithm. By integrating the interpolation function in a window of fixed size, total charge of the signal can be obtained. The position of the rising edge of the pulse at 50% of the peak value is considered as arrival time.

The charged FADC slices that are recorded comprises Cherenkov photons, NSB and photons from sources of light close to the telescope (eg: car flash). The pedestals comprise fluctuations induced by this background and noise induced by the readout chain. When a signal is not high enough to enable the lowgain recording, the second half of the FADC

readout does not contain cherenkov signal. So, these FADC samples are used to calculate the pedestal fluctuations. Pedestal readings can be obtained also from the dedicated pedestal run in which no cosmic signals are expected . The mean pedestal for each pixel and event is determined by averaging over the 500 closest pedestal values.

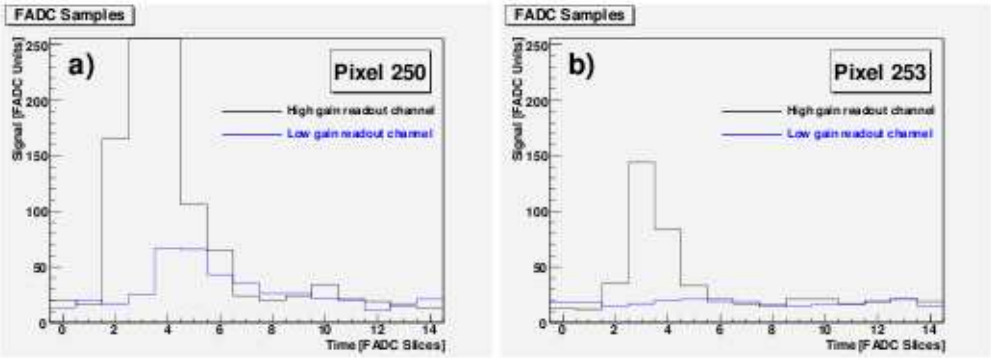

Figure 4.1: FADC read out window. Left: High gain and low gain FADC slices. Right: No low gain signal, this signal is used for calculating pedestal fluctuations.

The integrated charge of the extracted signal of FADC slices are in units of FADC counts. In order to convert this value into number of phe, 'F-factor' method is used as described in the previous chapter. This method, assumes a Poisson variance of the number of phe arriving in the first dynode of the PMT, a uniform phe detection efficiency, introduces a constant excess noise is in the gain fluctuations. The mean number of phe $< n >_{\rm phe}$ reaching the first dynode of the PMT is given by

$$< n >_{\rm phe} = F^2 \frac{(< Q > - < P >)^2}{\sigma_Q^2 - \sigma_p^2} \tag{4.2.1}$$

where $< Q >$ is the mean charge distribution with a standard deviation σ_Q and $< P >$ is the charge distribution from pedestal with a standard deviation σ_P. The F factor can be estimated in lab by using single phe response of the PMTs. The F factor of the MAGIC PMTs are measured as 1.15 (Gaug2006 [110]). The conversion factor from FADC counts to phe for each pixel can be found out from the following relation.

$$C = \frac{< n >_{\rm phe}}{< Q > - < P >} = F^2 \frac{(< Q > - < P >)}{\sigma_Q^2 - \sigma_P^2} \tag{4.2.2}$$

During a typical MAGIC observation ∼30 pixels are treated as bad pixels, as explained in the previous chapter. In such cases, the number of phe can be taken as the average of

neighboring pixels. More about MAGIC calibration can be found in Gaug2006 [110]. The charge and arrival time estimation is performed by a MARS program called *callisto*.

4.3 Image cleaning

Many of the camera pixels contain images of NSB fluctuations. The procedure to reject these fluctuations is called image cleaning. Image cleaning has two stages. In the first stage, pixels whose number of phe larger than a threshold value are selected. These pixels are named as core pixels. During the second stage, another threshold value is applied for the pixels which are the neighboring pixels of the core pixels. These pixels are called boundary pixels. The first and second threshold values can be 10 and 5, or 7 and 5 phe for core and boundary pixels respectively.

A recent advancement on image cleaning is the inclusion of arrival time of each photons. The method is based on the logic that Cherenkov photons from a γ-ray event should be spread in a few seconds whereas NSB arrive the camera pixels randomly. This method gives an additional requirement to select core and boundary pixels, which results in reducing the threshold of number phe in core and boundary pixels. Lowering the phe threshold will increase the probability of keeping the low energy γ induced images. In this method, the time difference between the arrival time of core pixels should be in 4.5 ns whereas that for core and boundary pixels should be in 1.5 ns. The usual charge cleaning used in this method is 6 and 3 phe, for core pixels and boundary pixels respectively. The image cleaning part is done by a MARS program called *star*.

4.4 Data selection

To improve the quality of analysis, bad data runs has to be rejected. The event rate is one of the most useful indicator to define the quality of data. If the event rate is too higher or unstable than an expected rate at a specific zenith angle, there is a possibility of having a hardware or software problems, or an accidental high intensity light (eg: car flash). A lower rate indicates either a hardware or software problems or bad weather (eg: high cloudiness).

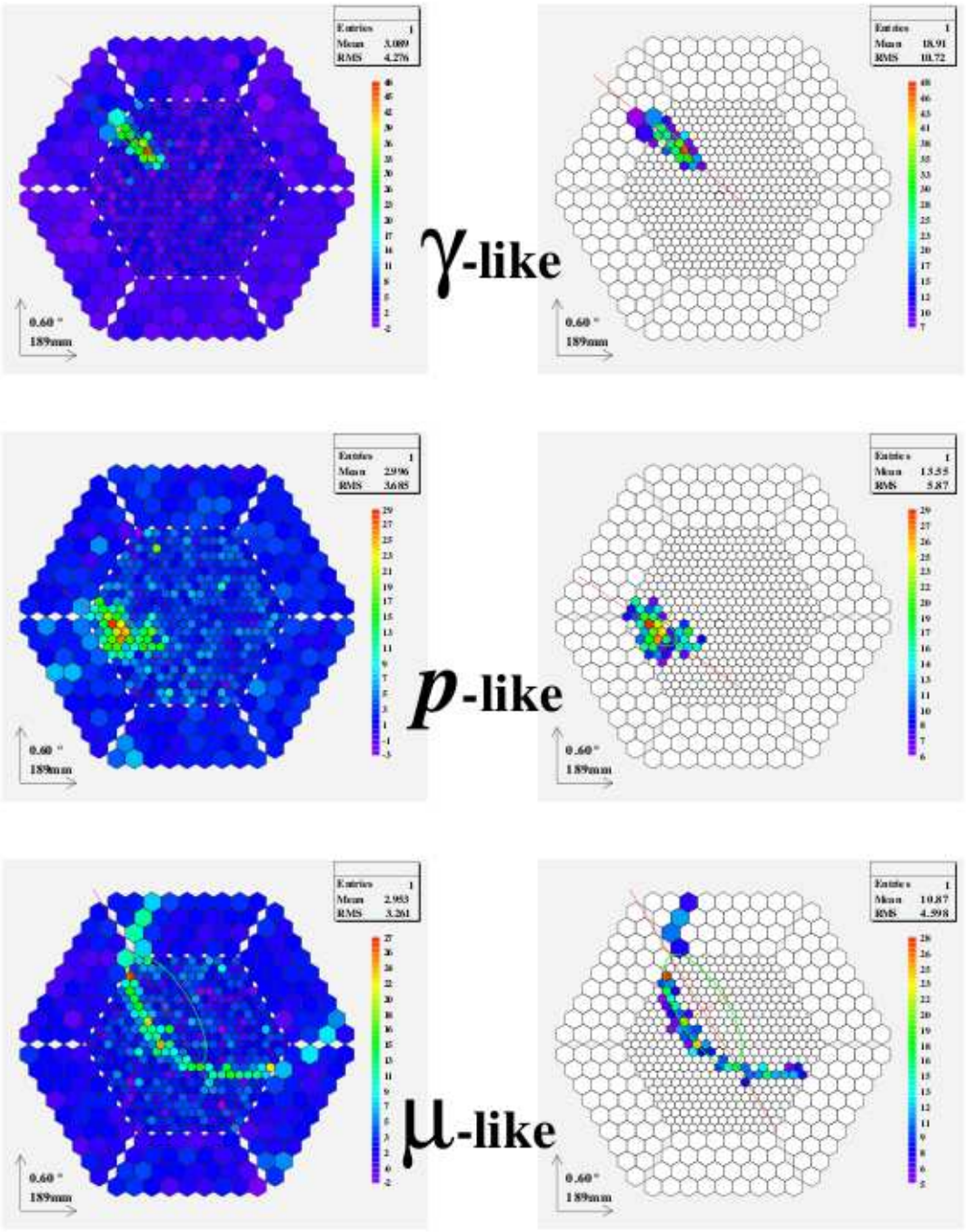

Figure 4.2: Images of a γ-like, hadron-like and muon-like events before and after cleaning.

4.5 γ/hadron separation

After image cleaning, the ratio between number of γ-induced images to hadron-induced images is 1:1000. However the images show some marginal difference due to different mechanisms of the shower formation. These differences in images can be used to separate γ/hadron induced images. The main parameters which are used in γ/hadron separation in IACT images are introduced by Hillas1985 [138]. Hillas parameters include:

Length: Half length of the main axis of the shower ellipse. It contains the information of longitudinal development of the shower in the atmosphere. *Length* of hadron-induced images are usually larger compared to the γ-induced images.

Width: Half length of the minor axis of the shower ellipse. It is correlated to the transverse development of the shower. Hadon-induced images are wider than γ-induced shower, due to the larger transverse momentum of hadron showers.

Size: The total charge contained in an image. This parameter is an indicator of the energy of the primary particle.

M3Long: The third longitudinal momentum of the major axis of the ellipse. $M3Long$ is useful to compute the head tail discrimination of a shower. if $M3Long$ is positive, the head of a shower is closer to the camera center than the tail.

Conc: Conc(N) is the charge contained in N brightest pixels with respect to the total charge of the image. This parameter helps to find the core of the shower. In Standard MAGIC analysis, $Conc(2)$ is used, and generally refers as Conc.

Leakage: Charge contained in the outermost pixels of the camera image, when the total image not fully contained in the camera. This parameter is important for the energy estimation of high energy events.

There are three more parameters which help in γ/hadron separation. the first two these parameters are calculated with respect to the prior knowledge of the source position.

Alpha: The angle between the major axis of the ellipse and the direction determined by the center of gravity of image and the source position in the camera. Normally the source position in the camera coincides the the camera center. In ideal cases, most of the γ-induced shower images point towards the source position in the camera, to result smaller *Alpha* distribution. On the other hand, hadronic shower images are isotropically distributed, gives rise to a flat *Alpha* distribution. This is the most powerful γ/hadron

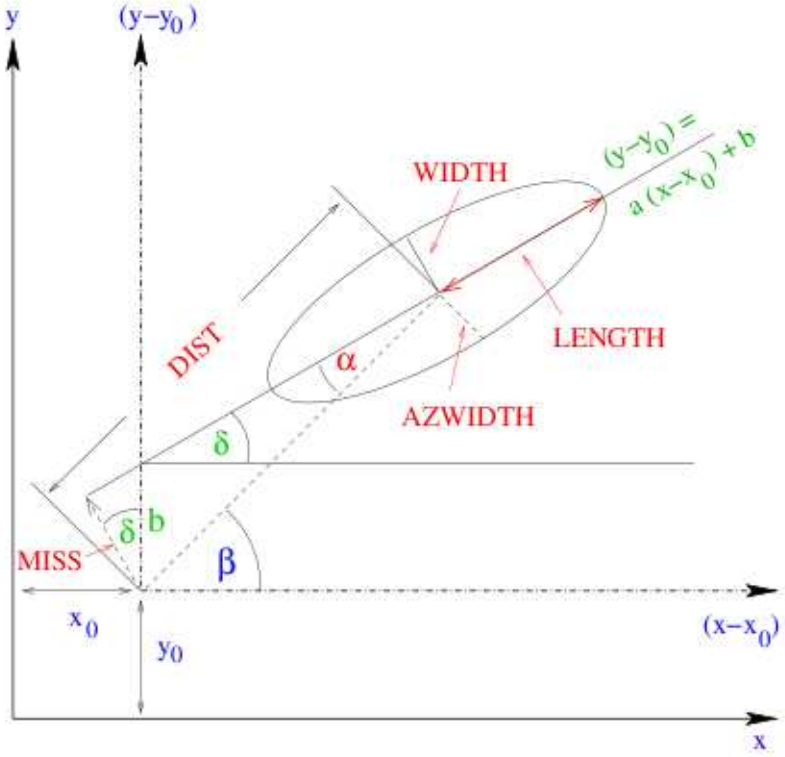

Figure 4.3: A drawing explaining Hillas parameters.

separation parameter.

Dist: The distance between the center of gravity of image and the source position in the camera. It is correlated with the impact parameter of the shower. It is an important parameter for energy estimation.

Time Gradient: The gradient of time along the major axis of the ellipse. It shows how fast the arrival time changes along the major axis. The parameter is correlated with the development of the shower. If the arrival time increases when moving away from the source position, time gradient is positive. For a typical γ-induced shower, time gradient is always positive.

4.5.1 Random Forest

MAGIC uses Random Forest (RF) method in order to distinguish γs and hadron induced shower images. It is a multi dimensional classification method to determine the average probability of an event to be a hadron induced shower. It is based on a collection of

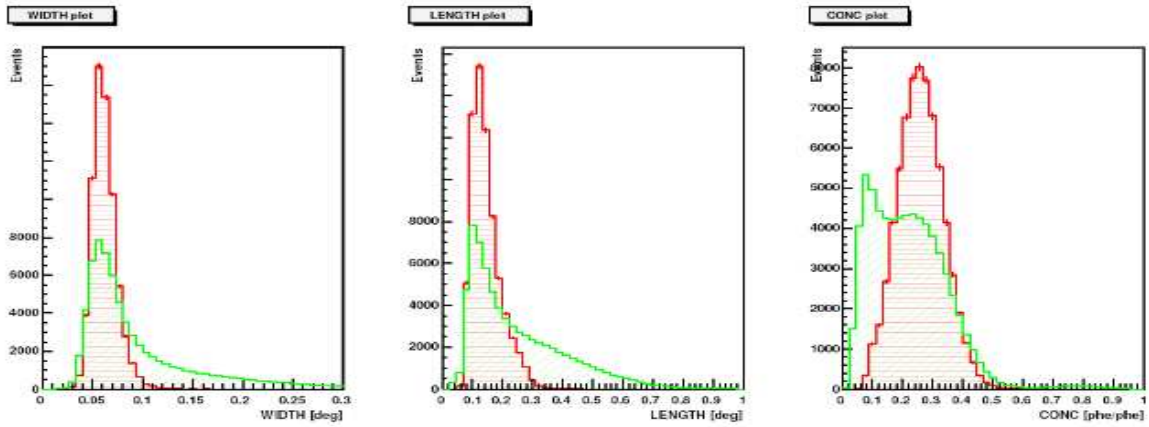

Figure 4.4: A comparison between MC data (red) and sample of real hadron-dominated data (green).

decision tree related to the parameters of random choices. A set of γ-induced events (Monte Carlo) and hadron-induced (OFF data) are used to train RF.

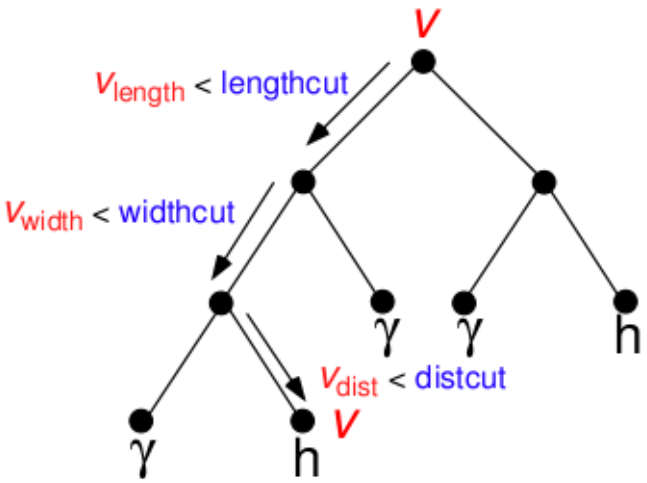

Figure 4.5: A example for the tree structure in Random Forest.

For the training samples, binary decision trees can be constructed which subdivide the parameter space in to two. Each parameter space is repeatedly subdivided in the same way. Suppose, if an event characterized by a vector v in an image parameter space has to be classified, at the first level, the RF split the sample based on any one of the image parameters. The split assigns a label l to v. In the next level, it choose another parameter

(it can be again the same parameter, as they are chosen randomly) and follow the same steps, until it reach terminal node. The mean classification value is calculated as

$$h(v) = \frac{\Sigma_{i=1}^{n} l_i(v)}{n} \tag{4.5.3}$$

where n denotes terminal node.

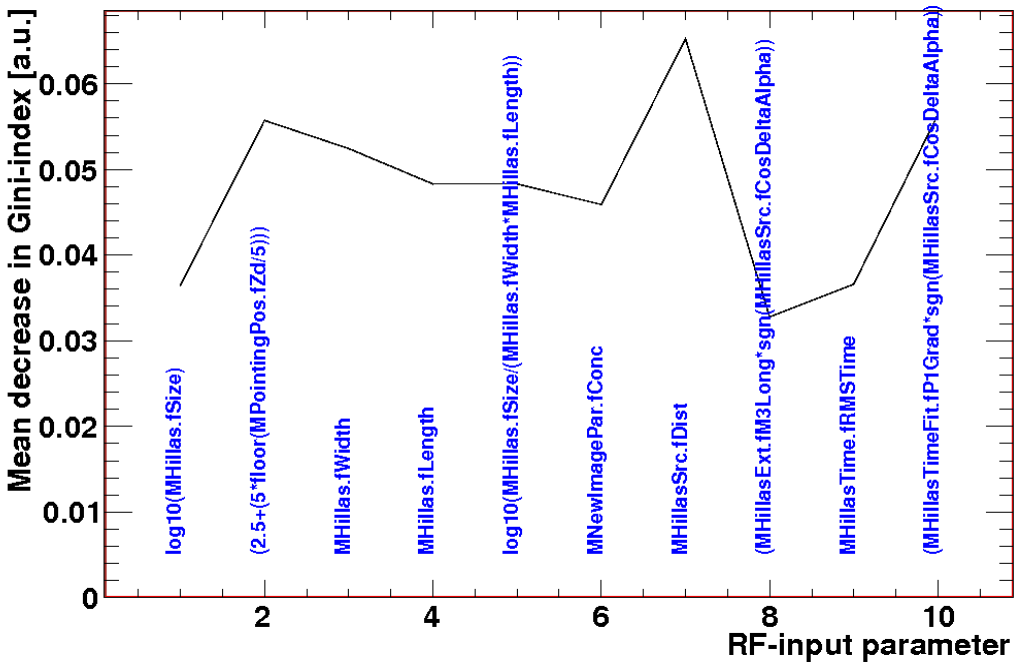

Figure 4.6: A example of gini index of each parameter of RF. It shows the comparative contribution of each parameter in RF.

For standard analysis, the parameters used for training the samples are *Length*, *Width*, *Conc*, *Dist*, *M3Long*, Time RMS, Time gradient, *Size* and Zenith angle. The last two parameters are included because of the the difference in image shape at different Size or Zenith. It is important to treat other parameters separately in each size and zenith.

After the training, the test samples can be classified by RF parameter, called Hadronness, which spans from 0 (for γ-like events) to 1 (for hadron-like events).

4.5.2 Signal extraction

Even after extracting the ON events based on the hadronness value, the data still contain the γ events and background. This background can be determined by applying the same

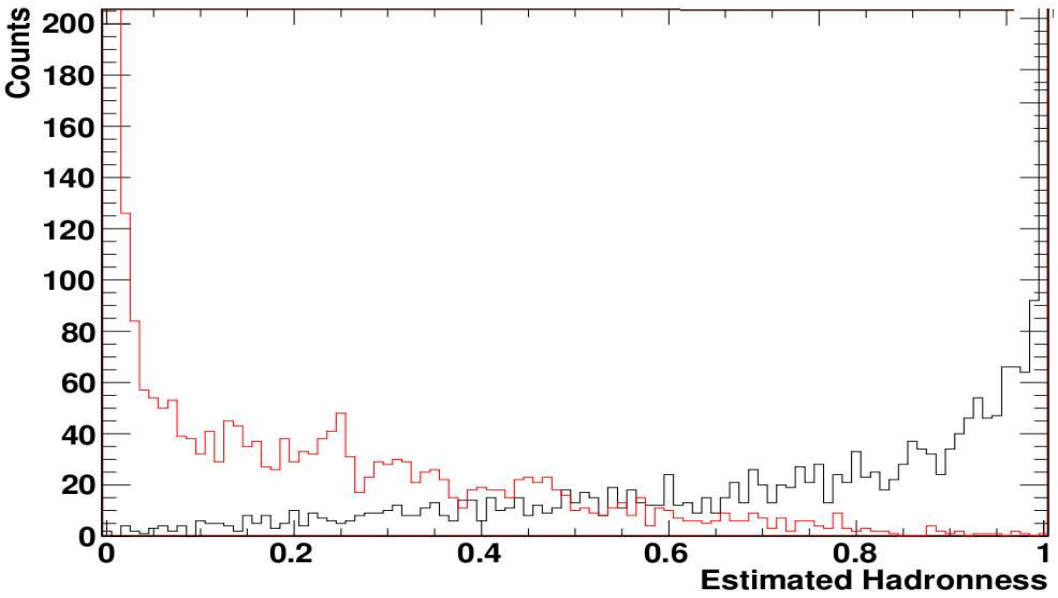

Figure 4.7: Estimated hadronness values.

cuts on OFF events. The number of γ events (N_γ) is given by,

$$N_{ON} - \alpha \times N_{OFF} \tag{4.5.4}$$

where α is the normalization factor between ON events and OFF events. The statistical significance of the excess γ events is given by LiMa formula [160]:

$$S = \sqrt{2}\left(N_{ON}\, ln\left(\frac{1+\alpha}{\alpha}\right) + N_{OFF}\,(1+\alpha)\left(\frac{N_{OFF}}{N_{ON}+N_{OFF}}\right)\right)^{0.5} \tag{4.5.5}$$

Two analysis methods are usually followed in MAGIC analysis, in order to determine N_{ON} and N_{OFF}: *Alpha* analysis and *Disp* analysis.

In *Alpha* analysis, all γ-like events are distributed according to *Alpha* parameter. Since the γ images are expected to be aligned along the source direction, the absolute value of the *Alpha* parameter is expected to be closer to zero. Hadron shower images are distributed uniformly along the *Alpha* parameter values, due to the hadron-induced shower features. Generally, a *Dist* cut is applied in *Alpha* analysis because of the limited trigger area.

Disp method reconstructs the source position independent of the known source position. *Disp* is defined as the distance between the image center of gravity and the unknown source position, which is assumed to be on the major axis of the ellipse. The *Disp* calcu-

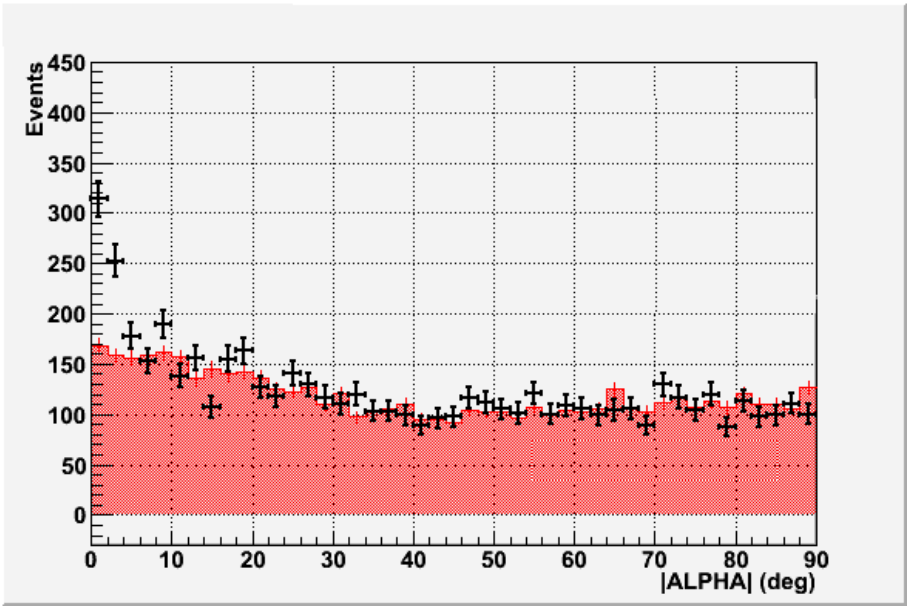

Figure 4.8: An example of *Alpha* distribution. Black points corresponds to ON data while the red shaded area corresponds to OFF data.

lated in standard MAGIC analysis is:

$$Disp = A\,Size + B\,Size\,\frac{Width}{Length + \eta\,Size \times Leakage} \tag{4.5.6}$$

where the parameters A, B and η are second order polynomials, which can be calculated from MC simulations or real data of a well known source. *Disp* method provides two possible source positions on the major axis of the ellipse. However, $M3Long$ parameter is used as head-tail discriminator, and to estimate the source position on the camera.

In order to choose hadronness and *Alpha* or θ^2 cut values should be optimized on a sample of data from known sources. Generally the data from Crab Nebula of similar observational conditions are used for this purpose.

4.6 Skymap

The estimates source position by *Disp* method can be displayed on a two-dimensional plot, which indicates the most probable source position. This called skymap of the source. De-Rotation of the events and background estimation are very important in constructing skymap. During the data taking, the telescope is moving in order to track the source in

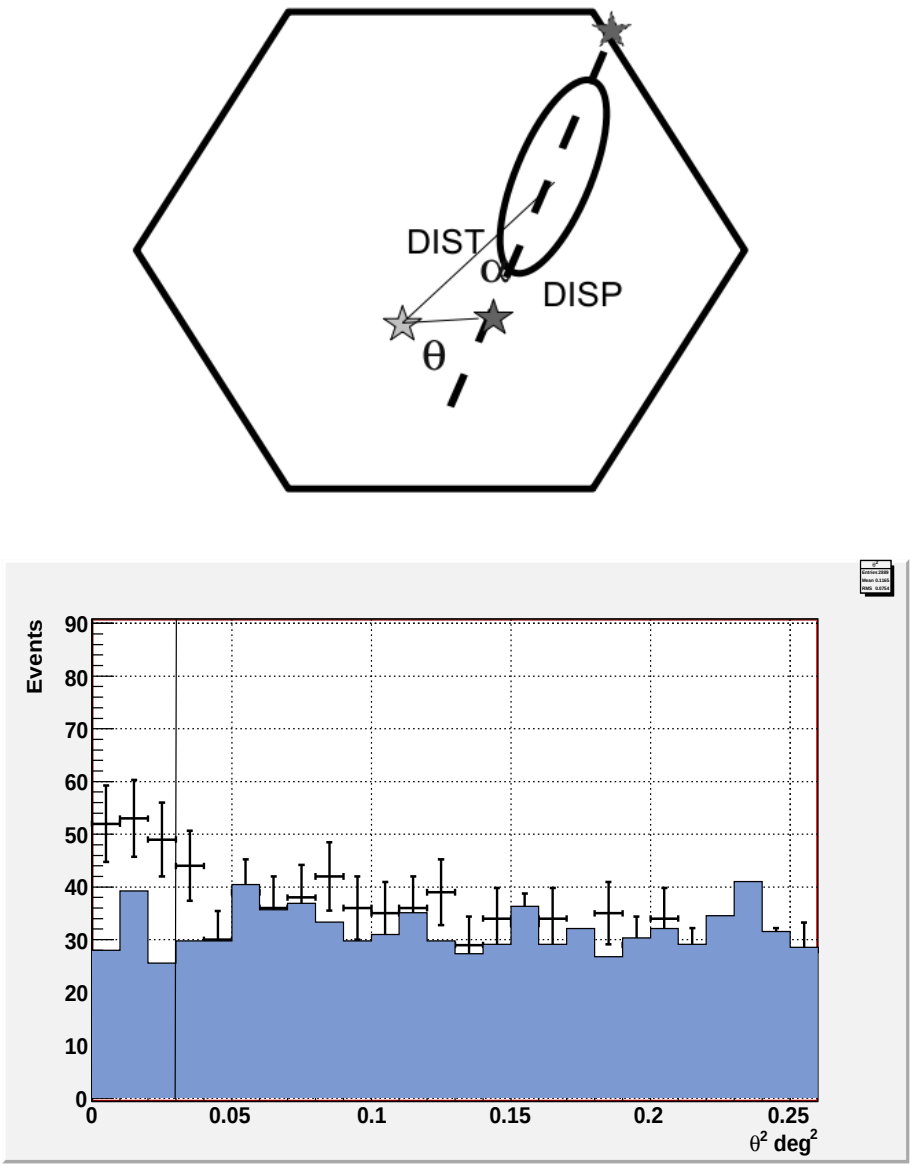

Figure 4.9: Top: Estimation of the *Disp* parameter from the camera image. The distance between estimated source position (dark star, using DISP) and the true source position (gray star) is called θ. Bottom: An example of θ^2 distribution. Black points corresponds to ON data, while blue shaded area corresponds to OFF data.

the sky, while the camera does not rotate. So a coordinate transformation is necessary to convert the camera events to the sky coordinates. So a de-rotation of the On data is performed using the information of telescope position during the data taking. Background

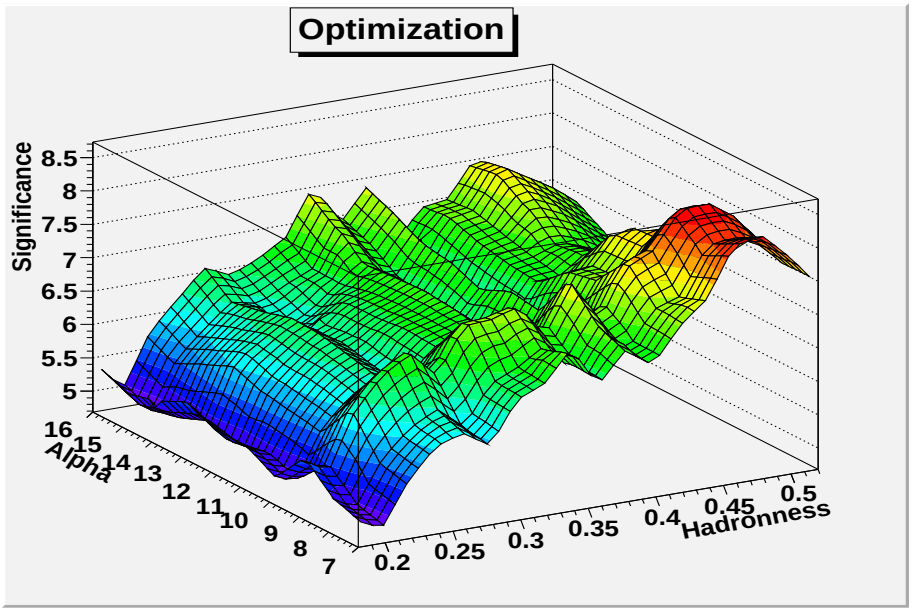

Figure 4.10: An example of optimization of Hadronness and *Alpha* cuts on Crab nebula data sample.

event estimation is done by using the data from the half of the camera that does not contain the source position, which will result in two histograms of two halves of the camera. These two histograms are merged considering the normalization factor, which depends on the time spent on each wobble position. For Off events a random de-rotation is applied using a randomly chosen de-rotation angle from the Off events histogram.

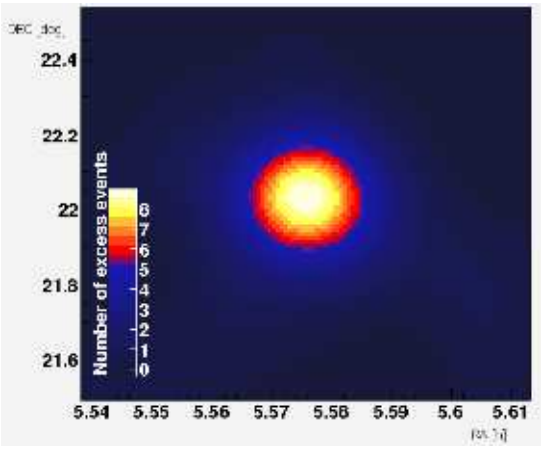

Figure 4.11: Skymap of Crab nebula in the energy range of 300 - 700 GeV.

4.7 Energy spectrum

4.7.1 Energy reconstruction

The energy reconstruction is performed by RF method with the same parameters used for the γ/hadron separation. MC γ-samples are used for training.RF calculates the probability that a given event belongs to certain energy event, based on the RF parameters and the known energy of MC events (E_{true}). The obtained result is given to another set of MC γ-samples in order to construct the migration matrix of estimated energy (E_{est}) and E_{true}. The migration matrix is used on the real data to reconstruct the energy of events. The correlation of E_{true} and E_{est} is linear for most of the energy range. However, E_{est} is over estimated at lower energies, and under estimated at high energies. This bias can be corrected by unfolding. The energy resolution for each energy bin is defined as:

$$\frac{E_{\text{est}} - E_{\text{true}}}{E_{\text{true}}} \tag{4.7.7}$$

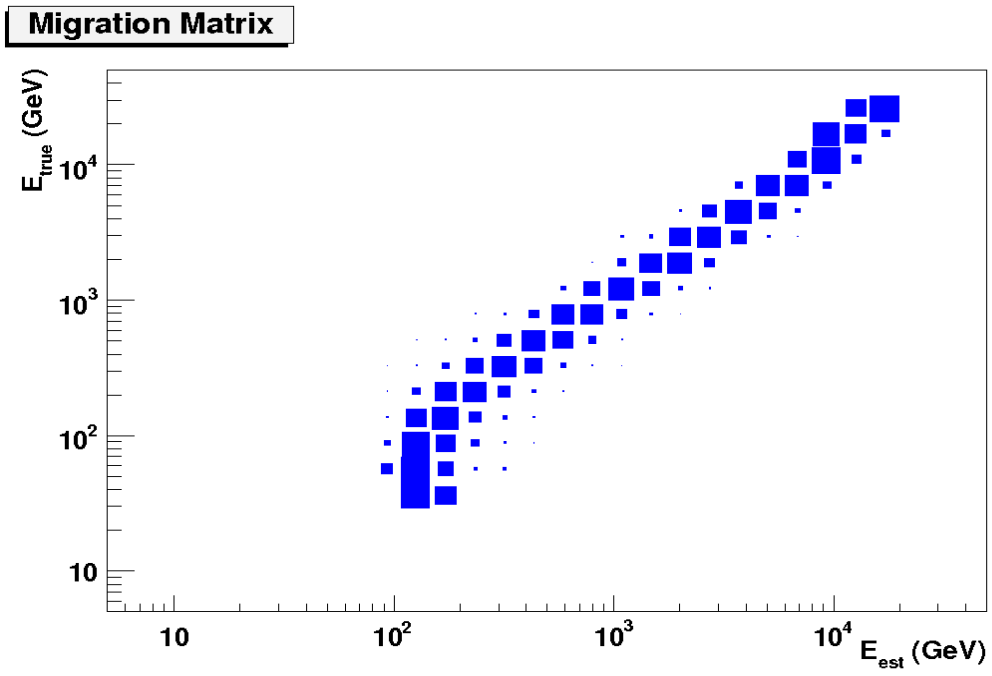

Figure 4.12: Relation between simulated γ-ray energy (E_{true}) and estimated γ-ray energy from RF method (E_{est})

4.7.2 Flux estimation

The differential γ-ray spectrum is defined by

$$\frac{\mathrm{d}F}{\mathrm{d}E} = \frac{\mathrm{d}N_\gamma}{\mathrm{d}E\, dA_{\mathrm{eff}}\, \mathrm{d}t_{\mathrm{eff}}} \tag{4.7.8}$$

where A_{eff} and t_{eff} are the effective collection area and effective observation time respectively.

The effective collection area is the area in which the showers can be observed by the telescope. It can be described by the detection efficiency $\epsilon(E, \theta, \phi, b)$, and the impact parameter b.

$$A_{\mathrm{eff}}(E, \theta) = \int_o^{2\pi} \int_0^{inf} \epsilon(E, \theta, \phi, b) b\, \mathrm{d}b\, \mathrm{d}\phi \tag{4.7.9}$$

where, θ and ϕ corresponds to azimuth and zenith angle respectively. The detection efficiency is calculated using MC γs. It is the ratio of number of γs survived after all cuts to the toal simulated γs. So the effective collection area can be written as:

$$A_{\mathrm{eff}}(E, \theta) = \frac{N_\gamma^{\mathrm{survived}}(E, \theta, \phi)}{N_\gamma^{\mathrm{simulated}}(E, \theta, \phi)} \times A_{\mathrm{simulated}} \tag{4.7.10}$$

The effective time is defined as the time required to detect events for an ideal instrument. In practice, the observation time is not identical to effective time due to the dead time of hardware. To record n number of events, the effective observation time t_{eff} is defined as:

$$t_{\mathrm{eff}} = \frac{n}{\lambda} \tag{4.7.11}$$

where, λ can be determined by fitting the consecutive events time difference distribution by a function

$$\frac{\mathrm{d}n}{\mathrm{d}t} = n_0\, \lambda \exp(-\lambda\, t) \tag{4.7.12}$$

This method requires a constant event rate. Therefore, data with different rate should be treated separately.

4.7.3 Unfolding

Due to experimental deficiencies the estimated energy E_{est} and true energy E_{true} may not be identical. The aim of unfolding is to recover the true distribution in E_{true} from E_{est}. The relation between E_{true} and E_{est} can be written as:

$$Y_i = \Sigma_j M_{ij} X_j \tag{4.7.13}$$

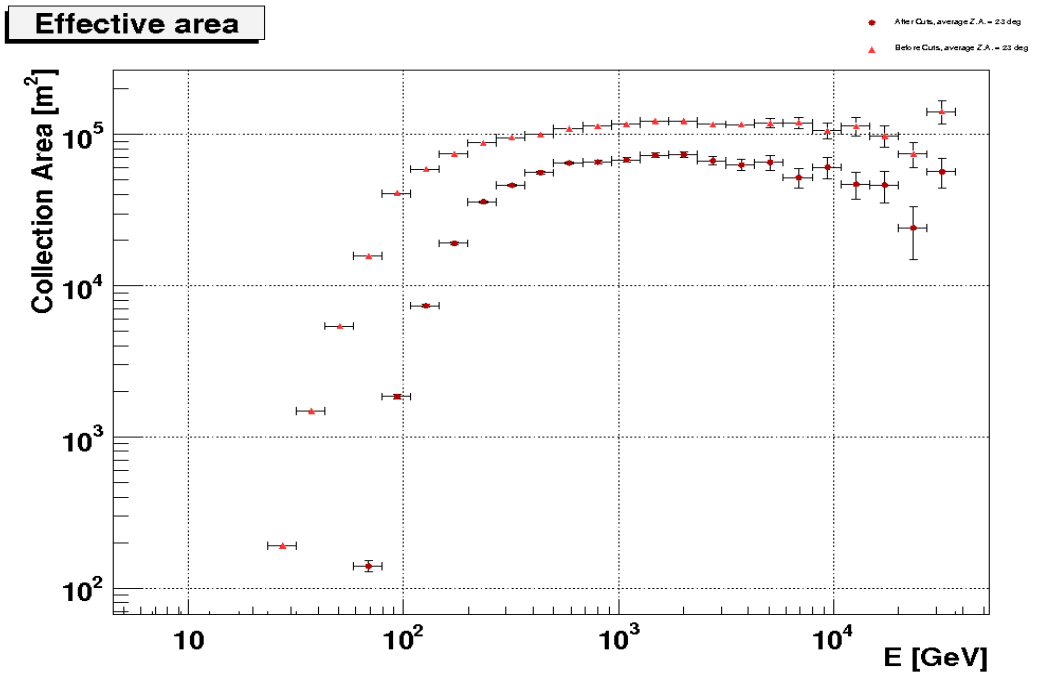

Figure 4.13: Effective collection area of γ-ray events at $z = 23$ deg before (triangle) and after applying cuts (filled circle).

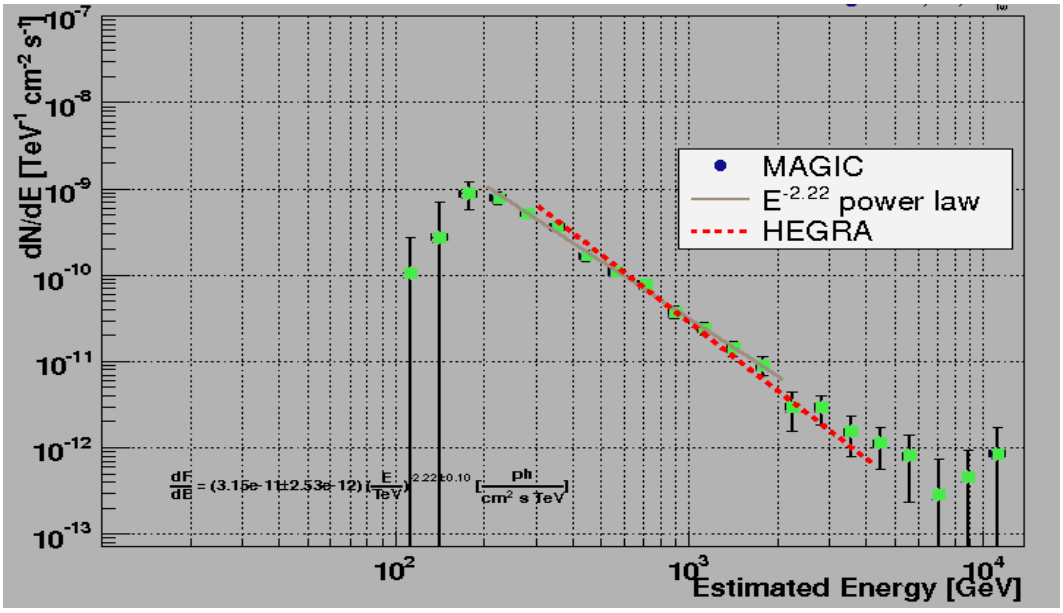

Figure 4.14: Differential spectrum of Crab Nebula. The red dotted line is the spectrum obtained by HEGRA telescope.

where X and Y corresponds to true and estimated energy respectively, and M is the detector response, which is the migration matrix described in the previous section. The aim of unfolding is to determine X from Y and M. Due to the large correlation between adjacent bins, the matrix inversion method results in large noise. In order to suppress this unwanted behavior, a regularization (Reg) is used, such that:

$$\chi^2 = \frac{\omega}{2} \times \chi_0^2 + Reg \tag{4.7.14}$$

where χ_0^2 corresponds to the degree of agreement between $M \times X$ and Y, ω is the regularization parameter, and the term Reg is a measure of smoothness of X. The different unfolding methods are different in the way of regularization. The usual unfolding methods that are used in MAGIC analysis are: Tikhonov1979 [229], Bertero1989 [56], and Schmelling1994 [206].

4.8 Light curve

Light Curve (LC) is the integral γ-ray flux in a certain time period. The time period can be in order of days, hours or minutes according to the strength of the source. LC is generally produced in order to understand the variability/stability of a source.

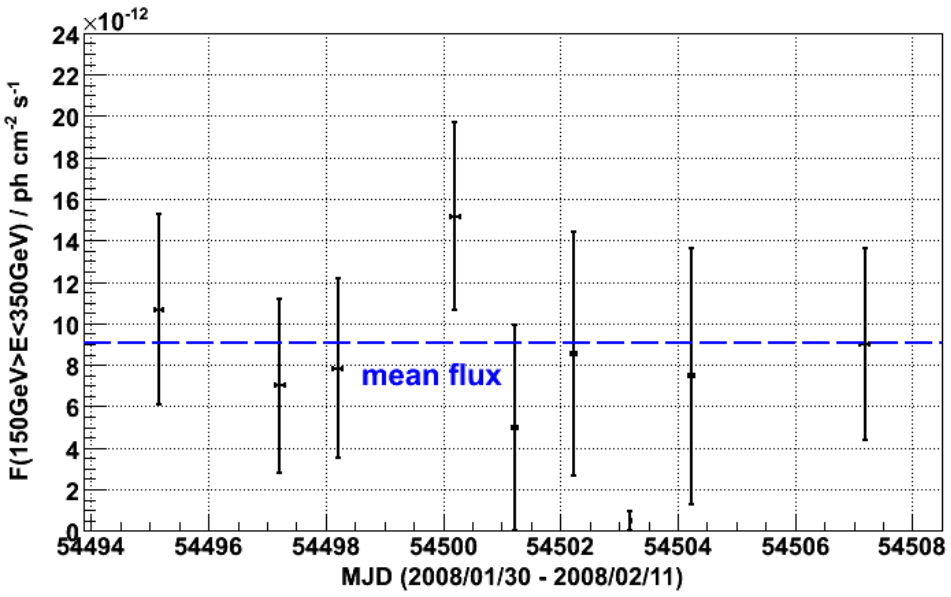

Figure 4.15: An example of Light Curve of AGN M 87 in 2008

5

QSO: 3C 454.3

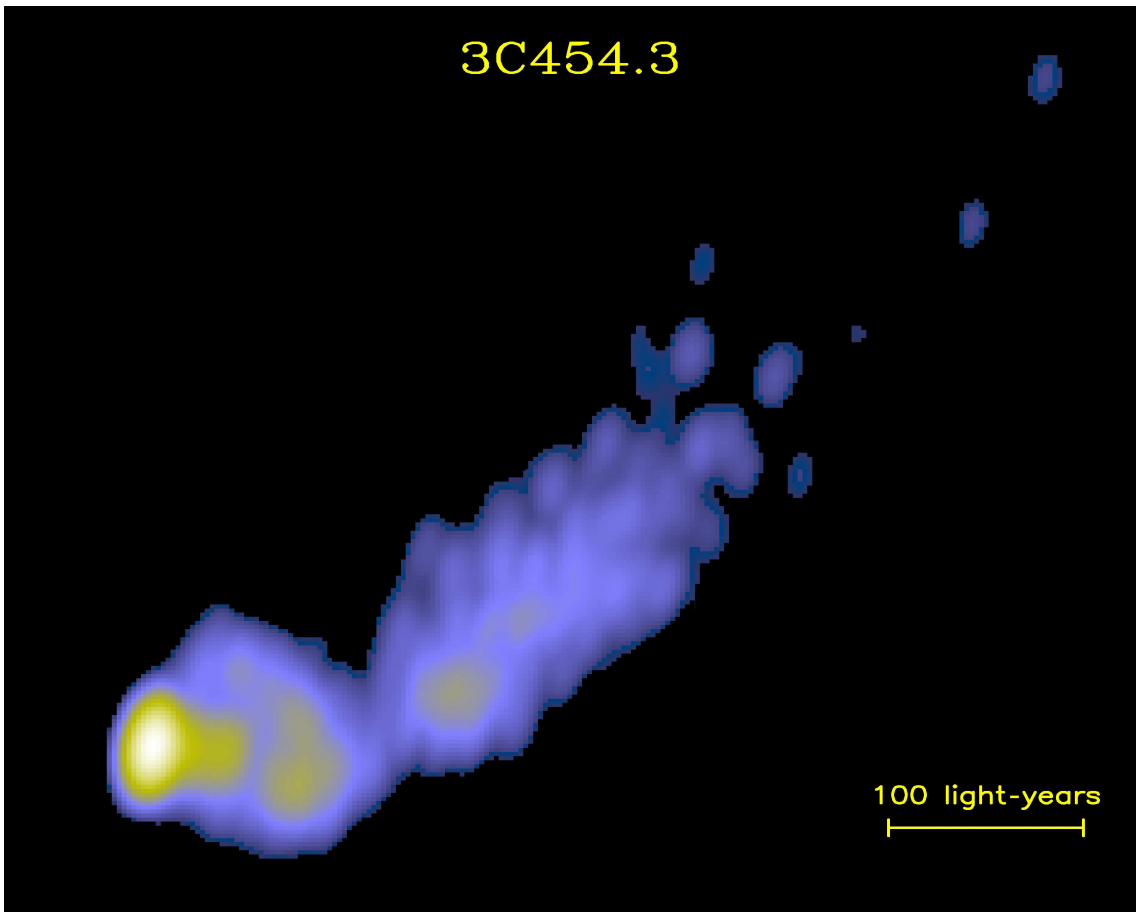

Figure 5.1: Radio image of 3c 454.3 as seen by VLBA.

5.1 Introduction

The detection of 3C 279 (Albert2008a [40]) indicates that also quasars can, to some extent, emit VHE radiation. General theoretical arguments support the view that powerful Flat Spectrum Radio Quasars (FSRQs) cannot be important VHE emitters (Tavecchio2008 [228]). Moreover, FSRQs are generally located at relatively high redshift, implying a huge absorption by the EBL. On the other hand, it is clear that the detection of these sources at VHE would be important for our comprehension of their structure and would provide a unique opportunity to probe the EBL at relatively high redshifts, allowing to study its evolution over cosmic time.

The FSRQ 3C 454.3 is a variable blazar at a redshift of $z = 0.89$. It exibits a strong emission lines in UV (Pian2005 [185]), and associated to a radio and X-ray jet (Lobanov2000 [162]; Marshall2005 [166]). The source has been observed in different frequencies several times. MeV and keV observation details can be found at Worrall1990 [246], Tavecchio2002 [226], and Zhang2005 [250]. It has also been detected several times in the γ-ray band by the *EGRET* telescope onboard *CGRO*, with an average photon index of $\Gamma = 2.2$ (Hartman1999 [135]). In 2005 it underwent a very active phase in optical and X-ray bands, triggering intensive observations in the radio, optical and X-ray (Swift, Chandra, INTEGRAL) bands (Villata2006 [237], Giommi2006 [125], Pian2006 [186]). Unfortunately no γ-ray satellite was operating at that time and no information in GeV band was obtained.

5.2 MAGIC observations

During the summer of 2007, 3C 454.3 was active, reaching a level of the optical emission comparable to 2005. Several observations in the optical, X-ray and γ-ray band were activated (optical: KVA, optical-UV: UVOT onboard Swift, X-ray: XRT onboard Swift, GeV band: AGILE). The AGILE satellite, detected intense emission from 3C 454.3 (Vercellone2008 [235]).

Triggered by these observations, the MAGIC telescope started observations of 3C 454.3 on July 18 and observations were prolonged until July 21. Then another intensive set of observations with MAGIC was performed in August. Another γ-ray active phase was

recorded by AGILE in November-December 2007 (Chen2007 [76]), which triggered another set of observations with MAGIC during that period. In all these observations, the source was not detected and only upper limits can thus be derived.

The observation was carried out in ON/OFF mode, during July 2007, and August 2007. Later, in November and December 2007, new observations were performed in wobble mode (total 6.8 hours). The zenith angle of all these observations ranged from 12 to 30 degrees. A few percent of the data had to be discraded because of the atmospheric absorption caused by calima (Saharan air layer: intensly dry, warm and dust-laden layer of the atmosphere) formed in La Palma during the days of observation. The total hours of data selected were 19 hours of ON data and 7 hours of wobble data.

The analysis was performed using the standard MAGIC analysis software. After calibration and two levels of image cleaning tail cuts, the camera images were parameterized by the Hillas image parameters. Two additional parameters - the time gradient along the main shower axis and the time spread of the shower pixels, were also computed. Hadronic background suppression was achieved using the RF method, in which for each event the Hadronness value was computed, based on the Hillas and the time parameters. The RF method was also used for the energy estimation. The Crab Nebula data from the same periods and zenith angle distributions were studied using the same analysis chain to check the validity of the results.

5.3 Results

The total number of events obtained in all 8 samples of data and the important cut parameters are given in Table 5.1. In order to claim the detection of a new source significance of the γ-ray events has been calculated. However the significance obtained was always bellow 2σ. In order to claim the detection, at least 5σ significance is required. The absence of a significant excess means that the rate or magnitude of the physical effect is below the sensitivity of the instrument. However, the results can then be expressed quantitatively as an upper limit on the observable events. We calculated an upper limits in 95% confidence level, based on Rolke2005 [199] method. We took into account 30% of systematic error in the upper limit calculation.

Table 5.2 shows the results in July-August observations, which we compare to the

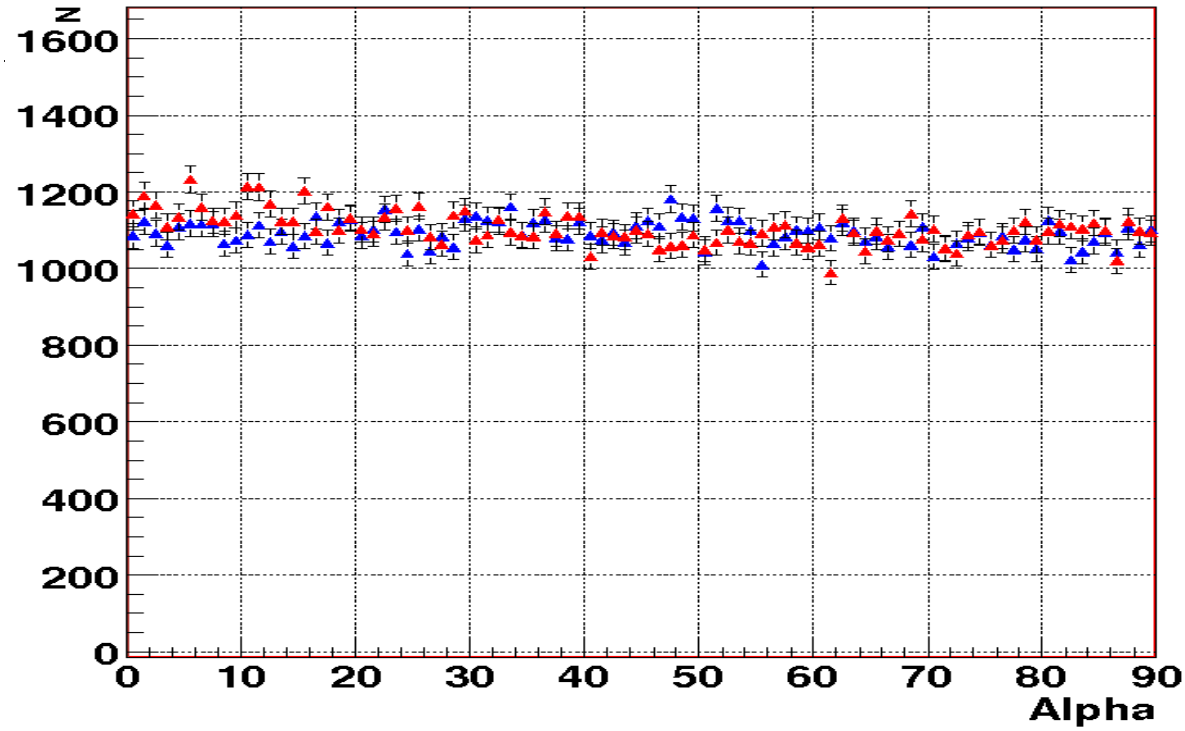

Figure 5.2: Alpha distribution of 3c 454.3 data in July. Blue triangles denote the ON data while red triangles denote OFF data.

AGILE observation in this work. Also the derived upper limits for November-December observation are given (Table 5.3).

5.4 Discussion

The SED of 3c 454.3 around the epoch of the July MAGIC observations, assembled with the available data, is shown in Fig.5.3. We report the nearly simultaneous data in the optical (KVA), optical-UV (UVOT onboard Swift), X-ray (XRT onboard Swift) and γ-ray (AGILE) band. For comparison we also show (open circles) historical data (see the Fig.5.3).

In the period July 24-30 AGILE observed an almost constant emission with an average flux above 100 MeV of $F(> 100\,\mathrm{MeV}) = (280 \pm 40) \times 10^{-8}$ ph cm^{-2} s^{-1} (Vercellone2008 [235]). We report the flux at 1 GeV (filled circle) assuming a spectral slope of $\Gamma = 2.5$ with the errorbar indicating the values for slopes in the range $\Gamma = 2 - 3$.

In the same figure, upper limits from observations with MAGIC are shown in triangles (observed: empty; deabsorbed: filled) (see Table 5.2). For the deabsorption we used the LowSFR model of Knieske2004 [150], which predicts a low level of the EBL close to what

3C 454.3 analysis					
Period	Energy (GeV)	Hadronness	Alpha	N_{ON}	N_{OFF}
July	83	0.5	15	54188	54705
	187	0.4	10	976	965
	476	0.15	7	62	52
August	83	0.5	15	121556	124019
	187	0.4	10	3892	3885
	476	0.15	7	202	221
November+December	113	0.5	9	22498	22518
	235	0.05	9	178	170

Table 5.1: Analysis summary of 3C 454.3.

$\langle E \rangle$	**U.L. July**		**U.L. August**	
[GeV]	C.U.	[erg cm^{-2} s $^{-1}$]	C.U.	[erg cm^{-2} s^{-1}]
83	0.04	0.78×10^{-11}	0.02	0.3×10^{-11}
186	0.05	0.62×10^{-11}	0.03	0.3×10^{-11}
476	0.03	0.169×10^{-11}	0.01	0.09×10^{-11}

Table 5.2: Derived upper limits on flux for July's and August's data. The columns represent respectively: the average true energy, the flux upper limit in Crab Unit (C.U.) and [erg cm^{-2} s^{-1}].

$\langle E \rangle$	**U.L. Nov. & Dec.**	
[GeV]	C.U.	[erg cm^{-2} s $^{-1}$]
113	0.3	4.6×10^{-11}
235	0.09	0.9×10^{-11}

Table 5.3: Derived upper limits on flux for wobble data. The columns represent respectively: the average true energy, the flux upper limit in Crab Unit (C.U.) and [erg cm^{-2} s^{-1}].

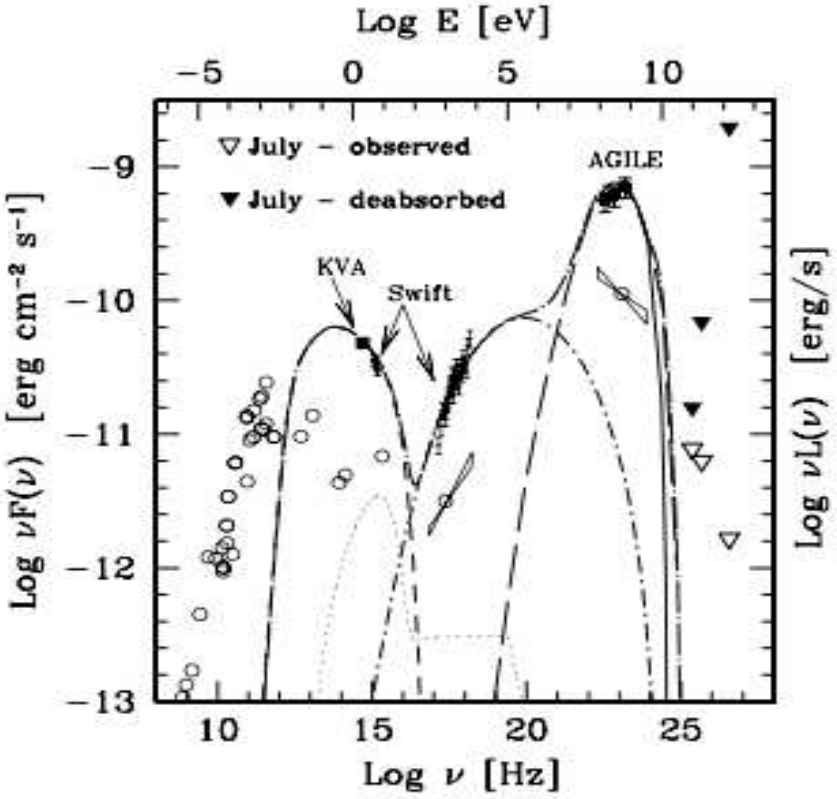

Figure 5.3: SED of 3C 454.3 assembled with multifrequency information available for the period close to the MAGIC observation at the end of July 2007 (optical: KVA, optical-UV: UVOT onboard Swift, X-ray: XRT onboard Swift, GeV band: AGILE). For AGILE we report the flux at 1 GeV (filled circle) assuming a spectral slope of $\Gamma = 2.5$ with the errorbar indicating the values for slopes in the range $\Gamma = 2 - 3$. Triangles report the observed (empty) and the deabsorbed (filled) upper limits of MAGIC in three different bands. For comparison we also report (open circles) historical data (Kuehr1981 [151], Gear1994 [113], Stevens1994 [220], Impey1988 [144], Smith1988 [207] for radio and optical; Tavecchio2007 [227] for X-rays from Chandra). The open circle and the bow-tye in the MeV-GeV region indicates the average EGRET spectrum (Hartman1999 [135]). Solid and long dashed lines report the results of the modelling with the synchrotron-inverse Compton model. The dotted line shows the emission from the accretion disk, while the spikes (solid line) around 10^{15} Hz shows the emission lines produced by the broad line region, used as soft photons for the inverse Compton process (see Tavecchio2008 [228] for details).

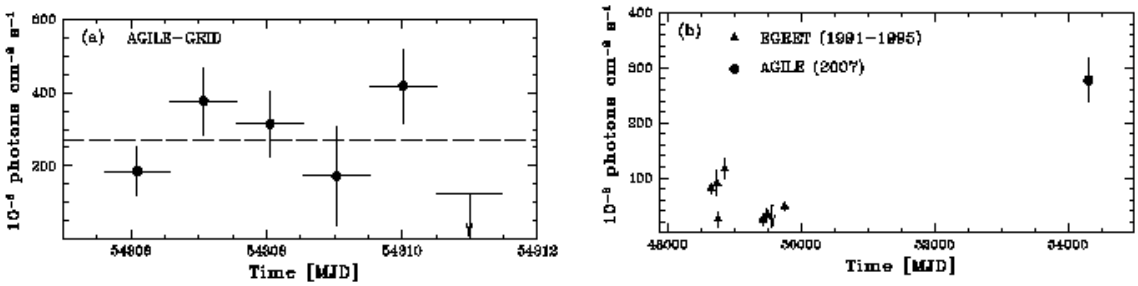

Figure 5.4: Left: AGILE-GRID γ-ray light curve at$E > 100\,\mathrm{MeV}$ (Vercellone2008 [235]). Right: A comparison between light curve measured by EGRET (Hartman1999 [135]) and AGILE-GRID.

is presently inferred from observations (Mazin2007 [174]).

One can see from Fig.5.3 that if the γ-ray (100 MeV-100 GeV) spectrum is relatively hard ($\Gamma < 2.5$) the MAGIC (absorption corrected) upper limit at $\sim$100 GeV is inconsistent with the extrapolation from GeV energies, thus indicating either that the spectrum is very soft ($\Gamma > 2.5$) or there is break (or a cut off) of the emission between 1 GeV and 100 GeV band. As discussed below, this is consistent with the expectations from the simplest leptonic model.

Emission from blazars is dominated by the non-thermal continuum of a relativistic jet closely aligned toward the observer. The SED of FSRQs is widely interpreted in terms of synchrotron and inverse Compton emission from high-energy electrons (leptonic models). The latter component is probably dominated by the scattering of the external photons (originating in the disk and/or in the broad line region [BLR], Sikora1994 [214]), though the synchrotron self-Compton emission (Maraschi1992 [167]) can significantly contribute in the X-ray band. The SED of 3C 454.3, including optical, X-rays and GeV measurements around the end of July, has been already discussed and modelled by Ghisellini2007 [118]. Here (solid line in Fig.5.3) we report a similar model. However, given the focus on the VHE emission we used a more refined calculation, including the full Klein-Nishina (KN) cross section for the IC scattering, and also considering the absorption of γ-ray photons through pair production within the BLR. Moreover, the external radiation field (assumed to be isotropic in the frame of the black hole), usually approximated by a black body peaking in the UV region, has been calculated using the photoionization code *CLOUDY* (Ferland1998 [95]). Details on the emission model can be found in Maraschi2003 [168],

while the description of the calculation of the external radiation field is reported in Tavecchio2008 [228]. Briefly, we assume that the emission is produced within a spherical region of radius $R = 5 \times 10^{16}$ cm, in motion with bulk Lorentz factor $\Gamma = 18$ at an angle $\theta = 3.2$ deg with respect to the line of sight. The tangled magnetic field has an intensity $B = 4.2$ G. The emitting particles, with total density $n = 1.7 \times 10^4$ cm^{-3}, follow a (steady state) broken-power law energy distribution extending from $\gamma_1 = 1.5$ to $\gamma_2 = 5 \times 10^3$, with indices $n_1 = 1.7$ and $n_2 = 3.25$ below and above the break at $\gamma_b = 16$. This *purely phenomenological* distribution has been assumed to reproduce the observed shape of the blazar SEDs, without any specific assumption on the acceleration/cooling mechanism acting on the particles. With this choice we are allowed to assume extreme low-energy slopes ($n_1 < 2$) such as those required for 3C 454.3, which cannot be obtained under standard conditions. It is conceivable that, at least in these cases, the electron distribution derives from two (continuously operating) different acceleration mechanisms. We also neglect the effects related to the cooling of particles in the KN regime, discussed by Moderski2005 [176]. We note, however, that these effects should produce a bump in the optical-UV synchrotron emission which is not apparent in the available data, though the poor coverage does not allow a firm conclusion. We model the external radiation field assuming that the disk emission (dotted line in figure), with a total luminosity of $L_{\rm disk} = 5 \times 10^{46}$ erg/s, is reprocessed by clouds of the BLR, a sphere with radius 3×10^{17} cm (we assume that clouds are characterized by standard values of the density $n_{BLR} = 10^{11}$ cm^{-3} and hydrogen column density, $N_H = 10^{23}$ cm^{-2}). The model (with parameters similar to those obtained using the self-consistent particle distribution of Ghisellini2007 [118]) allows us to reproduce reasonably well the multiwavelength SED of 3C 454.3.

The rapid decrease of the emission above few tens of GeV is related to two effects: i) the decrease of the scattering cross section and ii) the absorption of the produced γ-rays through pair production. The energy above which the KN effects become important can be roughly expressed as: $E_{\rm KN} \simeq 22.5 \nu_{o,15}^{-1}$ GeV, where $\nu_{o,15}$ is the frequency of the external photons (in units of 10^{15} Hz). The emission including only the KN effects, neglecting the absorption, is shown by the long-dashed line. The frequency above which the absorption of γ-rays become effective can be roughly expressed as: $E_{\gamma\gamma} \simeq 60 \nu_{t,15}^{-1}$ GeV, where $\nu_{t,15}$ is the frequency of the target photons (in units of 10^{15} Hz). Therefore, as shown by the

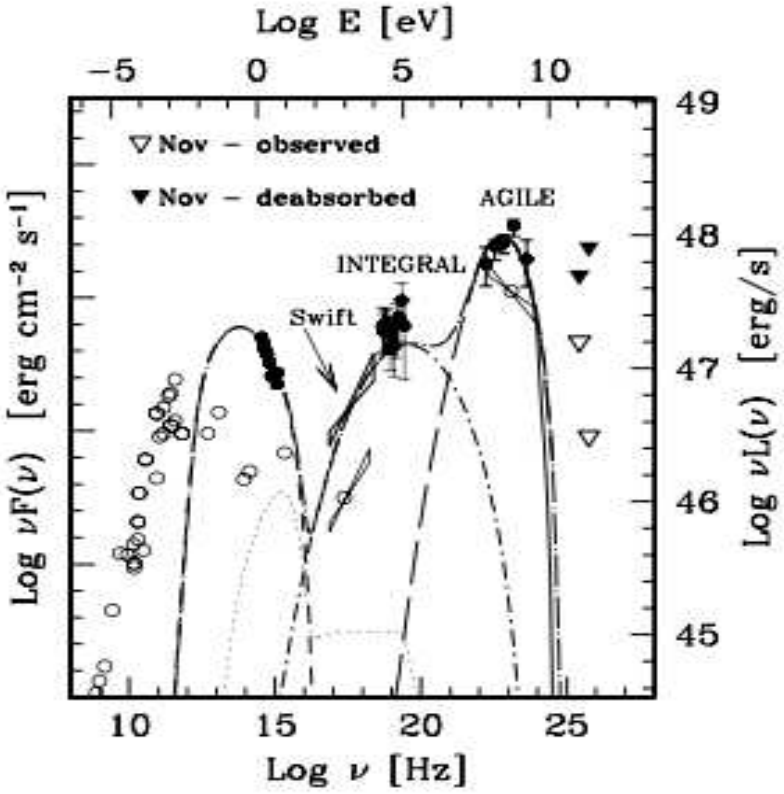

Figure 5.5: SED of 3C 454.3 in November 2007. (optical: KVA, optical-UV: UVOT onboard Swift, X-ray: XRT onboard Swift,Integral, GeV band: AGILE). The description of the model fit is same as in Figure 5.3.

Month	Γ	B	K	n_1	n_2	γ_{min}	γ_b	γ_{max}	R
July	18.4	3.1	5×10^5	1.9	3.6	85	500	6.5×10^3	6.5
November	17.8	5	5×10^5	1.9	3.9	80	500	3.9×10^3	5

Table 5.4: Parameters used in the emission model of July and November 2007. Γ : Bulk Lorentz factor of the emission region; B: magnetic field in Gauss; K: density of relativistic electrons in cm^{-3}; n_1 and n_2: low and high energy slope of electron energy distribution; γ_{min}, γ_b and γ_{max}: minimum energy, break energy and maximum energy of electron energy disribution; R: radius of emission region in units of 10^{15} cm.

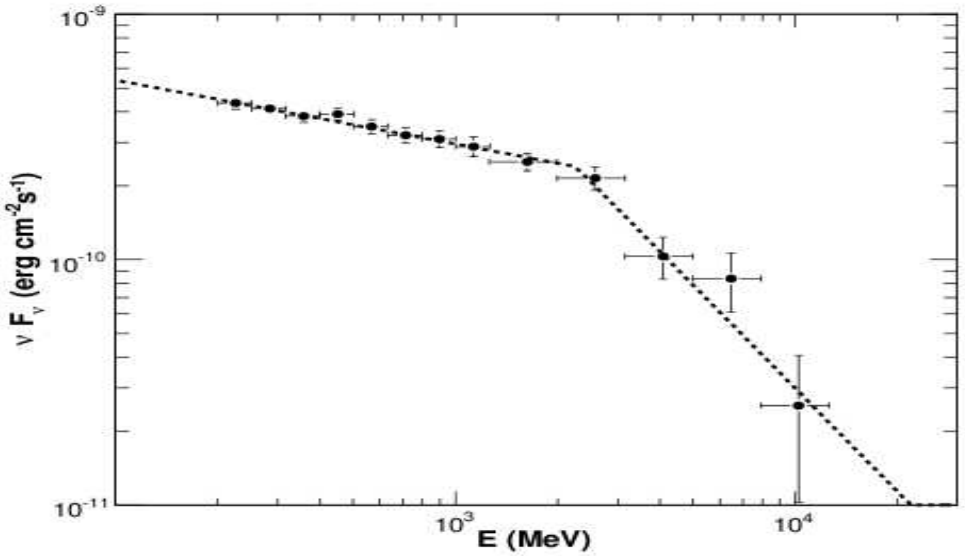

Figure 5.6: The break the 3c 454.3 spectrum in HE range, as observed by *Fermi*.

solid line in Fig.5.3 (calculated including both effects), the expected emission above 20-30 GeV is rather small, consistently with the observed upper limits. Note that, although the limit set by KN effects is a characteristic feature of leptonic models, absorption of γ-rays by soft photons can also be relevant for hadronic models (e.g. Reimer2007 [197]).

5.5 3C 454.3 flare in 2009

3C 454.3 went on a huge flare in November - December 2009. The LC measured by Fermi is shown in Fig.5.7. The preliminary analysis of MAGIC data of 6 hours, shows no detection of VHE γ-ray signal during this flare. However, the extrapolation (See appendix) spectrum on VHE range shows that the source can be detected in 50 hours by MAGIC stereo observation in ideal conditions, even though the extrapolated spectrum just overlap with the sensitivity plot of MAGIC stereo system. This is because of the intrinsic break in the spectrum (see also: Abdo2009b [2]) and comparatively high redshift of the source, hence a strong EBL attenuation. The energy break used in the extrapolation is 0.28 GeV. VHE γ attenuation is calculated using Gilmore2009 [123] EBL model. The source can be detected in a very high flare by MAGIC, and stronger model constraints will be obtained with observations of *Fermi*.

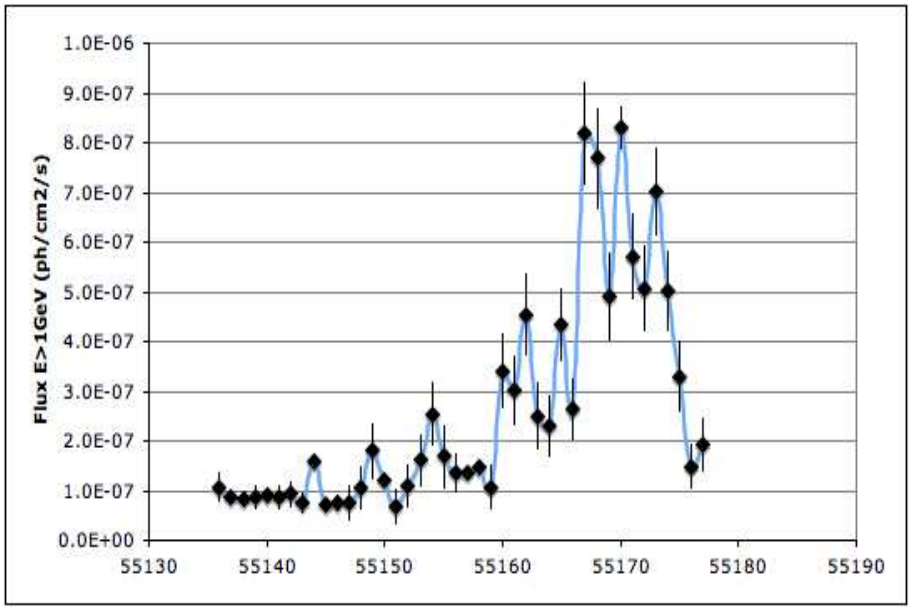

Figure 5.7: The LC of 3c 454.3 at $E > 1GeV$ as measured by *Fermi* in November - December 2009.

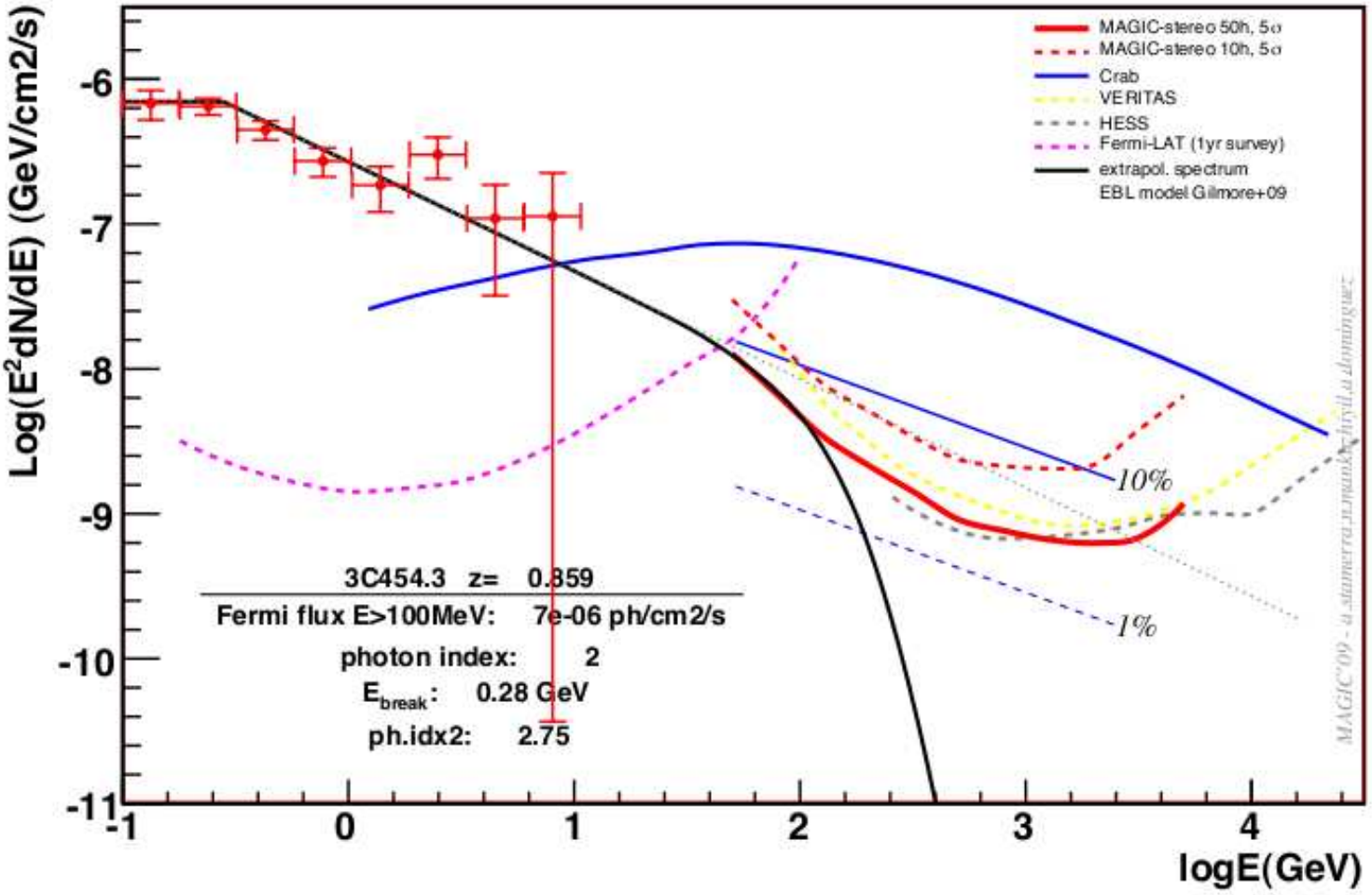

Figure 5.8: The extrapolated *Fermi* spectrum to VHE range, while 3C 454.3 was in a high state in December 2009 (see Appendix C for the plot details).

6

HBL: PG 1553+113

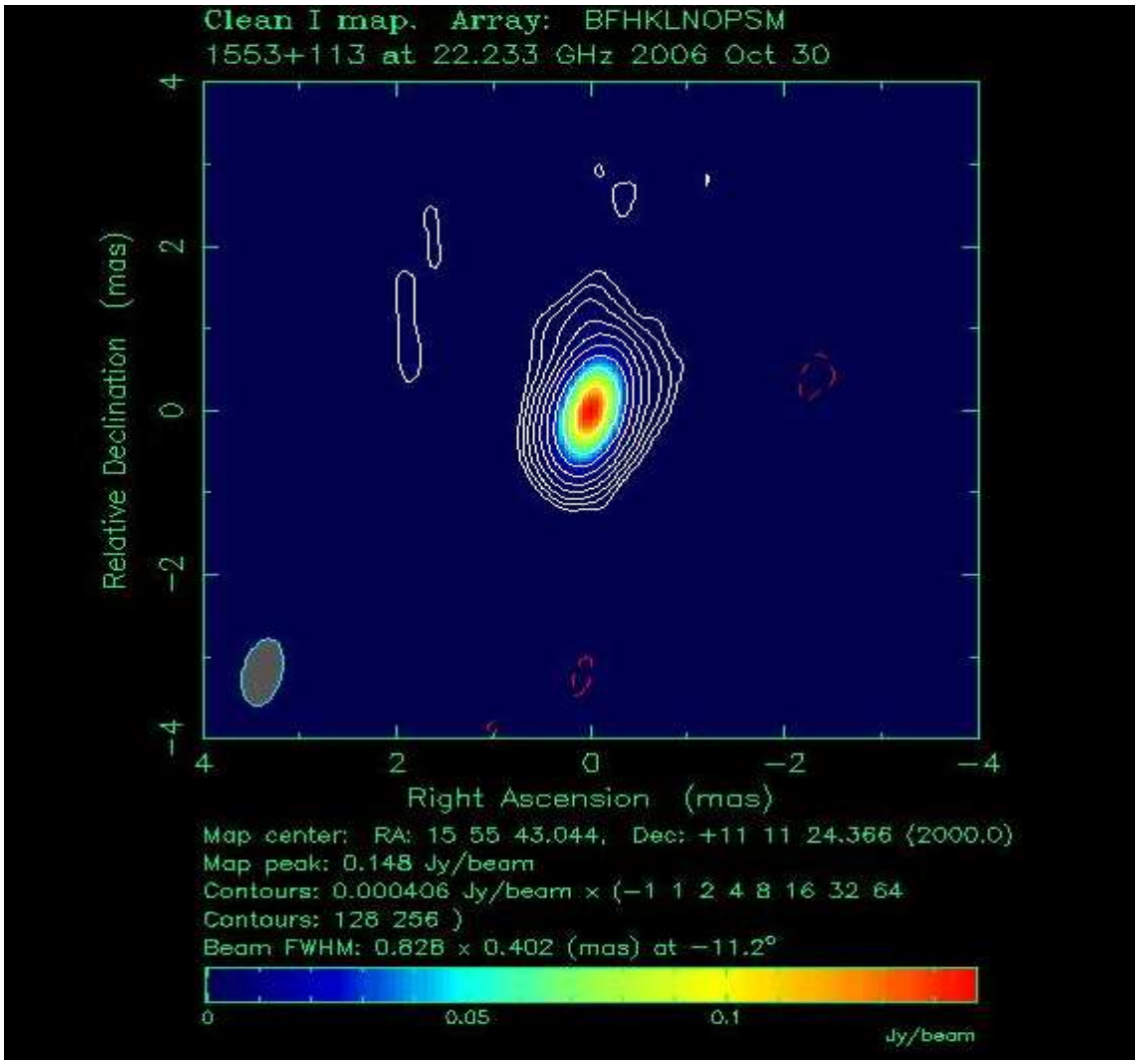

Figure 6.1: Radio image of PG 1553+113 as seen by VLBA.

6.1 Introduction

PG 1553+113 is a well known blazar in VHE sky. Even though it has been detected several times in VHE range, it is important to understand the emission features of the source in MWL observation, because blazars often show violent flux variability, that may or may not be correlated between the different energy bands. Strictly simultaneous observations are crucial to investigate these correlations and understand the underlying physics of blazars. This is the first simultaneous broad-band (i.e., HE+VHE) γ-ray observation, though AGILE did not detect the source.

The HBL source PG 1553+113 was firmly detected at very high energy γ-rays (VHE; photon energy E>100 GeV) by MAGIC at a significance level of $8.8\,\sigma$ above 200 GeV, based on data from April - May 2005 and January - April 2006 (Albert2007a [34]). Observations with the HESS telescope array in 2005 yielded a tentative detection in VHE band, at the level of $4\,\sigma$ ($5.3\,\sigma$ using a low energy threshold analysis; Aharonian et al. 2006), which was confirmed later with the combination of the 2005 and 2006 datasets (Aharonian2008b [25]). After the first detection of PG 1553+113 with MAGIC, a multi-frequency campaign on this source was conducted in July 2006 (Albert2009 [43]). The main difference between our present and previous campaign is the use of X-ray and the high energy (HE; photon energy E>100 MeV) flux.

The lack of detection of spectral lines (neither in emission nor in absorption) in the optical spectrum of PG 1553+113 makes it impossible to measure its redshift directly (Falomo1990 [96]). However, an ESO-VLT spectroscopic survey of unknown-redshift BL Lac objects suggests $z > 0.09$ (Sbarufatti2006 [205]), while the absence of host galaxy detection in HST images raises this lower limit to $z > 0.25$ (Treves2007 [230]). On the other hand, the absence of a break in the VHE spectrum can be interpreted as suggesting $z < 0.42$ (Mazin2007 [172]). The absence of Ly-α forest in the the spectrum also constrains a lower redshift. However, Cosmic Origins Spectrograph GTO team have been analyzing recent spectral observations of PG1553+113 in the far-UV (1150-1750A). The data is of sufficient quality to pick out 40 Lya absorbers at low redshift including a strong line at $z = 0.395$ (confirmed with metal lines at the same redshift). There are no obvious Lya systems between there and $z = 0.47$. By assuming to have at least a few Lya systems in this interval, one can constrain $z_e m > 0.395$, and probably $z \approx 0.40 - 0.43$ is an accurate

estimate for the system (private communication: C. W. Danforth).

6.2 Observations

6.2.1 Optical and Near Infrared (NIR) data

6.2.1.1 KVA observations

The KVA (Kungliga Vetenskaps Akademien, Royal Swedish Academy of Sciences) telescope is located at the Roque de los Muchachos, in the North-Atlantic canary islands of La Palma and is operated by the Tuorla Observatory. The telescope is composed of a 0.6m f/15 Cassegrain devoted to polarimetry, and a 0.35m f/11 SCT auxiliary telescope for multicolour photometry. This telescope has been successfully operated remotely since autumn 2003. The KVA is used for optical (R-band) support observations during MAGIC observations. Typically, one measurement per night and per source is conducted. Photometric measurements are made in differential mode, i.e. by obtaining CCD images of the target and calibrated comparison stars in the same field of view (Villata1998 [236]).

6.2.1.2 Abastumani observations

Observations at the Abastumani Observatory (Georgia, FSU) were performed with the 70 cm meniscus telescope (f/3). This is equipped with an Apogee Ap6E CCD camera, with 390×390 pixels, and a field of view of 15×15 arcmin. Its quantum efficiency is 40% at 4000 Å and 65% at 6750 Å. The frames were acquired in the Cousins' R band and were reduced with the DAOPHOT II package[1].

The source magnitude was derived from differential photometry with respect to a reference star in the same field, which lies ~ 46 arcsec east and ~ 5 arcsec south of PG 1553+113. According to the USNO 2.0 Catalogue (Monet1998 [177]), its magnitude is $R = 13.2$.

6.2.1.3 REM observations

REM (Rapid Eye Mount, a fast-slewing robotized infrared telescope) acquired photometry of PG 1553+113 on April 18, 25 and May 2 2008 with all available filters (VRIJHK). The

[1] `http://www.star.bris.ac.uk/ mbt/daophot/`

data reduction followed standard procedures as described in Dolcini2005 [85]. The mean flux of observation is reported in Table 6.3. The NIR magnitudes were calibrated against the 2MASS catalog. For the SED reconstruction, all magnitudes have been dereddened with the dust IR maps (Schlegel1998 [208]).

6.2.2 X-rays: RXTE/ASM Observations

The All Sky Monitor (ASM) on board the *Rossi* X-ray Timing Explorer (*R*XTE) satellite consists of three wide angle scanning shadow cameras. The cameras, mounted on a rotating drive assembly can cover almost 70% of the sky every 1.5 hours (Levine1996 [159]). The measurements were done between March 1 and May 31, 2008. The mean measured flux of PG 1553+113 is shown in Table 6.3.

6.2.3 γ-ray data

6.2.3.1 HE band: AGILE observations

The Gamma-ray Imaging Detector (GRID, 30 MeV - 30 GeV) on board the high energy astrophysics satellite AGILE observed PG 1553+113 in three different time intervals: March 16-21, March 25-30 and April 10-30 2008. The GRID data were analyzed using the AGILE standard pipeline (see Vercellone2008 [235] for a detailed description of the AGILE data reduction), with a bin size of $0.25^\circ \times 0.25^\circ$ for E $>$ 100 MeV. Only events flagged as confirmed γ-rays and not recorded while the satellite crossed the South Atlantic Anomaly were accepted. We also rejected all events with a reconstructed direction within 10° from the Earth limb, thus reducing contamination from Earth's γ-ray albedo. PG 1553+113, observed at about 50 degrees off-axis with respect to the boresight, was not detected by the GRID at a significance level $> 3\ \sigma$ and therefore the 95% confidence level upper limit was calculated. Considering that AGILE has a higher particle background at very high off-axis angles, we calculated also the upper limit selecting only photons with energies greater than 200 MeV in order to minimize the possible contamination at low energies. The log of the AGILE observations and the results of the analysis are reported in Table 6.2. During March - April 2008, the source was outside the field of view of SuperAGILE, the hard X-ray (20-60 keV) imager onboard AGILE.

6.2.3.2 VHE band: MAGIC observations

The MAGIC observations for this campaign were carried out on March 16-18 and April 13, 28-30 in 2008. The zenith angle of the data set ranges from 18 degree to 36 degree. Observations were performed in wobble mode. After data rejection based on the standard quality cuts and the trigger rate, 7.18 hours of total effective observation time data was selected.

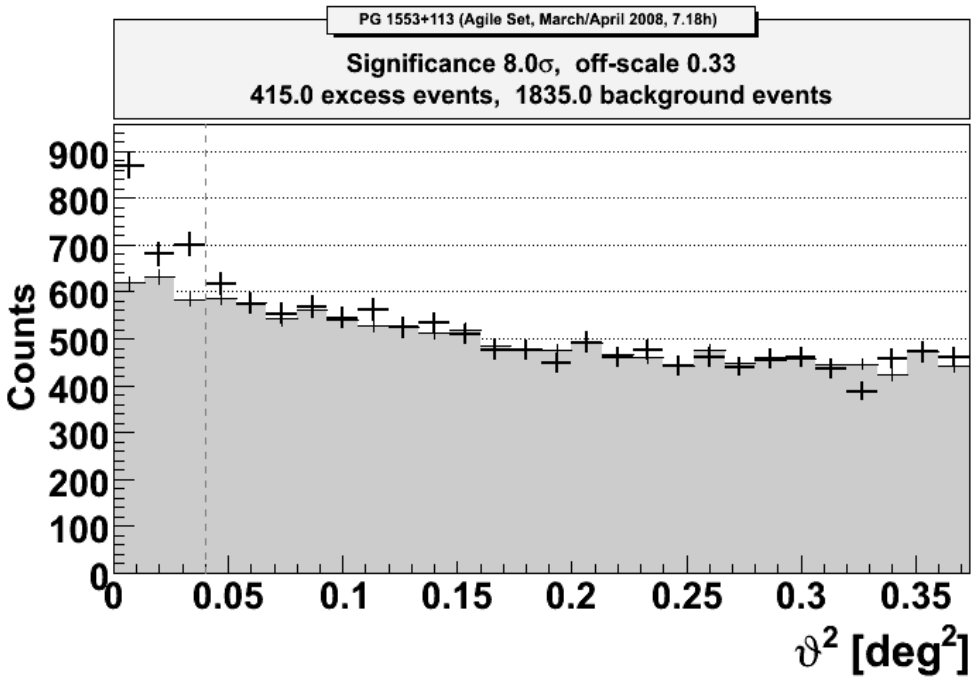

Figure 6.2: The alpha distribution of PG 1553+113 data. The black points correspond to ON events where as the gray back ground correspond to OFF events.

An automatic analysis pipeline (Dorner2005 [88]) was used to process the data, which includes the muon calibration (Goebel2005 [127]), and an absolute mispointing correction (Riegel et al. 2005). The charge distribution and arrival time information of the pulses of neighboring pixels was used to suppress the contribution from the night sky background in the shower images. Three OFF regions were used to determine the background, providing a scaling factor of 1/3 for the background calculation. The shape and orientation of the shower images were used to discriminate γ-like events from the overwhelming background. To select the γ-like events a dynamical cut in Area (Area=π·WIDTH·LENGTH) versus SIZE (total charge contained in an image) and a cut in ϑ (angular distance between real

source position and reconstructed source position) were applied. The above mentioned image parameters are described by Hillas1985 [138]. The reconstructed γ-ray spectrum is shown in Fig.6.5. For the spectral reconstruction, looser cuts were applied to ensure that more than 90% of the simulated gamma photons survived. Varying cut efficiencies between 50% and 95% over the entire energy range were applied to the data in order to check systematic effects of the cut efficiency on the spectral shape (shown as gray area in Fig.6.5). Data which has been affected by calima (sand dust from the Sahara in an air layer between 1.5 km and 5.5 km a.s.l. causing absorption of the Cherenkov light) has been corrected following the method described in Dorner2009 [90].

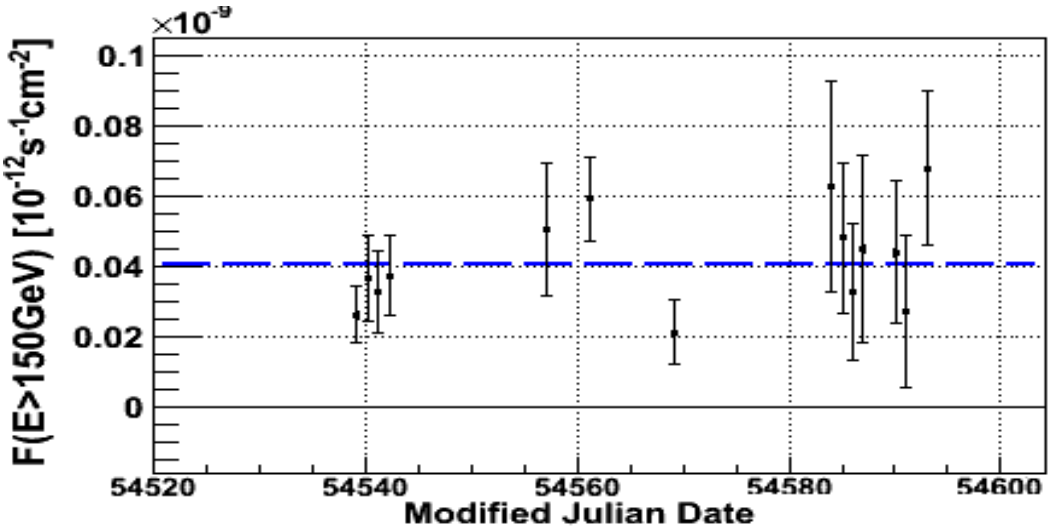

Figure 6.3: The light curve of PG 1553+113 during the MAGIC observations.

6.3 Results

Analyzing the MAGIC data, an excess of 415 γ-like events, over 1835 normalized background events was found, yielding a significance of $8.0\,\sigma$. The resulting differential VHE spectrum of PG 1553+113, averaged over all observing intervals, is plotted in Fig.6.5 (filled circles). It can be well described by a power law $\frac{dN}{dE} = F_0 \left(\frac{E}{200GeV}\right)^{\Gamma}$ m^{-2} s^{-1} TeV^{-1}, where F_0 is normalization flux at 200 GeV and Γ is photon index during our observation, which are given in Table 6.1. Test on a possible spectral cut off has also been performed. However fewer points of the spectrum does not favour a cut off power law over a simple power

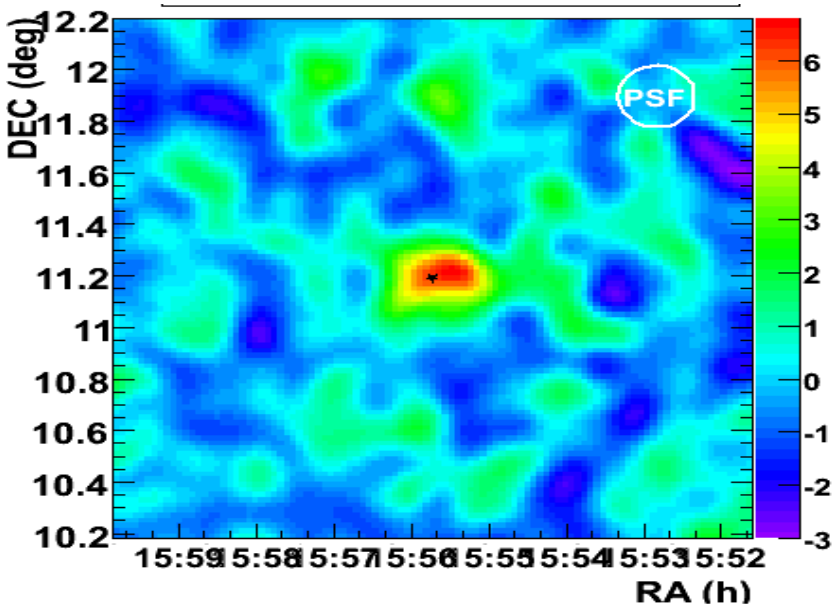

Figure 6.4: The skymap of PG 1553+113

law. The lowest point of the spectrum is at 82 GeV, mainly because of the losses of low energy events from the cleaning and γ selection cuts. The values obtained during our previous observations (Albert2007a [34]) are also given.

The interaction of VHE γ-rays with the extragalactic background light, leads to attenuation of the VHE γ-ray flux via e^+e^- pair production. We computed the deabsorbed (i.e., intrinsic) fluxes using a specific 'low star formation model'of the EBL (Kneiske2004 [150]), assuming a source redshift of $z = 0.3$. The resulting deabsorbed points are represented as empty squares in Fig.6.5.

Observation period	F_0 [ph TeV^{-1}s^{-1}m^{-2}]	Γ
March-April 2008	$2.0 \pm 0.3 \times 10^{-6}$	-3.4 ± 0.1
March 2008	$1.9 \pm 0.4 \times 10^{-6}$	-3.5 ± 0.2
April 2008	$2.1 \pm 0.4 \times 10^{-6}$	-3.3 ± 0.2
April-May 2005+January-April 2006	$1.8 \pm 0.3 \times 10^{-6}$	-4.2 ± 0.3

Table 6.1: The F_0 and Γ during MAGIC current observations and previous observation. The errors are statistical only. The systematic uncertainty is estimated to be 35% in the flux level and 0.2 in the photon index.

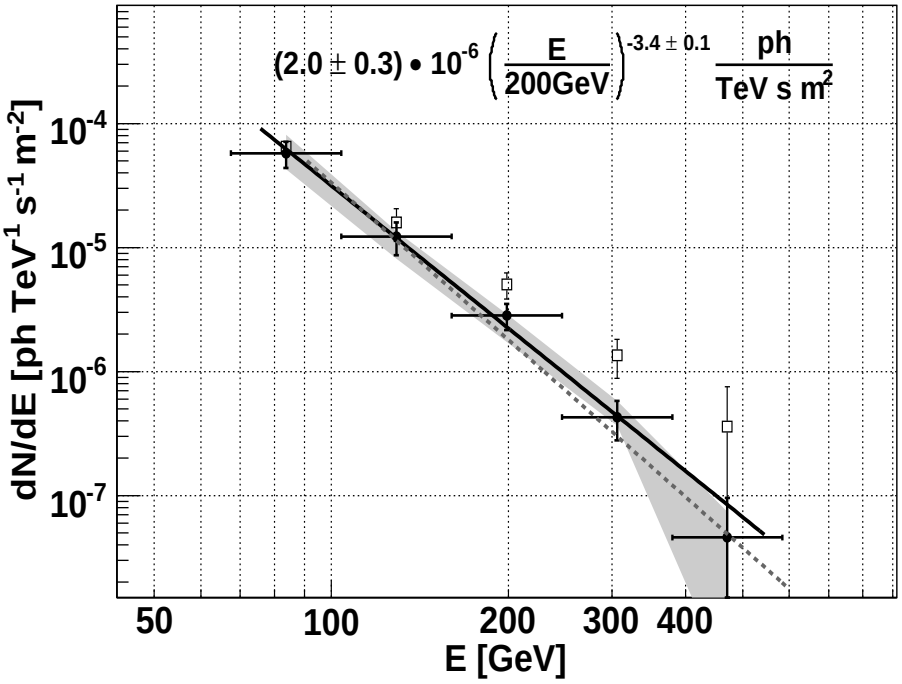

Figure 6.5: The MAGIC measured spectrum of PG 1553+113 (filled circles). The χ^2/DOF of the fit is 1.36/3. The EBL-corrected points are shown as empty squares. The spectrum obtained during our first observation is shown in dashed line.

The HE data reduction results from AGILE are summarized in Table 6.2. The $2\,\sigma$ upper limits obtained by AGILE are consistent with the average flux point observed by the *Fermi*-LAT for this source during August-Octorber 2008 (Abdo2009a [1]). The upper limit obtained in the third time interval has been used for the modeling of SED. The fluxes and corresponding effective photon frequencies of the other telescopes which contribute to this multi-frequency campaign are reported in Table 6.3.

6.4 Discussion

The SED of PG 1553+113 is shown in Fig.6.6. The VHE and HE γ-ray flux points are from MAGIC and AGILE respectively. The X-ray point, provided by *R*XTE/ASM, represents the average flux between March 1 and May 31, 2008. The optical R-band point, provided by the KVA telescope, is the average flux obtained on March 18 and 19. The flux provided by Abastumani is the average flux of April 1 - May 17 observations. In addition to these

Time interval	Energy	U.L.Flux [ph m^{-2}s^{-1}]
March 16-21	> 100 MeV	5.6×10^{-3}
	> 200 MeV	3.6×10^{-3}
March 25-30	> 100 MeV	5.5×10^{-3}
	> 200 MeV	2.8×10^{-3}
April 10-30	> 100 MeV	3.4×10^{-3}
	> 200 MeV	2.1×10^{-3}

Table 6.2: $2\,\sigma$ Upper limit calculated from AGILE data in three different time intervals.

data, we also used the NIR flux from REM. To assess the soundness of this addition, we checked the optical variability of the source during this period using Abastumani data, and found that the source was essentially stable (minimum and maximum values of $log(\nu F_\nu)$ are -10.14 and -10.02 respectively). For comparison of the HE flux, we included the flux points from the *Fermi* γ-ray Space Telescope (Flux, $F(E > 100MeV) = 8 \pm 1 \times 10^{-4} ph\, m^{-2}\, s^{-1}$ and photon index, $\Gamma = 1.7 \pm 0.6$; Abdo2009a [1]). The average flux (15-30 keV) obtained from the X-ray satellite $Swift$/BAT during 39 months (December 2004 - February 2008) of observation (Cusumano2010 [80]) is also included.

We fit the resulting simultaneous SED with a homogeneous one-zone SSC model (Tavecchio2001 [225]). The model assumes that the source is a spherical plasmon of radius R, moving with a Doppler factor δ towards the observer at an angle θ with respect to the line of sight threaded with a uniforming distributed tangled magnetic field of strength B. The injected relativistic particle population is described as a broken power-law spectrum with normalization K, extending from $\gamma_{\rm min}$ to $\gamma_{\rm max}$ with indices n_1 and n_2 below and above the break Lorentz factor $\gamma_{\rm br}$. By fitting the observed flux with the model, we obtain following parameters: $\gamma_{\rm min} = 1$, $\gamma_{\rm b} = 3 \times 10^4$, $\gamma_{\rm max} = 2 \times 10^5$, $K = 0.5 \times 10^4$ cm$^{-}3$, $n_1 = 2$, $n_2 = 4.7$, $B = 0.7$ G, $R = 1.3 \times 10^{16}$ cm, and $\delta = 23$. The optical and X-ray flux constrain on the slope of electron energy distribution (EED), while X-ray and VHE spectrum fix the Lorentz factors.

The difference between the current SED and the previous one published in Albert2007a [34] is due to flux variation in the X-ray and small variation of the slope of VHE spectrum. We used different SED models in the current and previous paper. Doppler factor (21 and

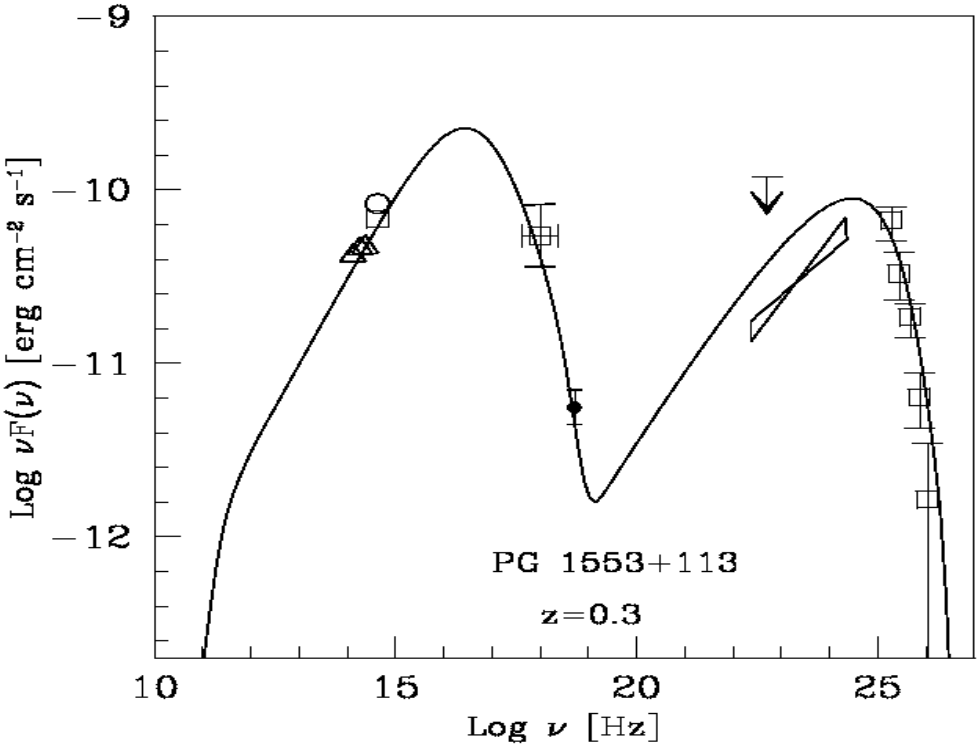

Figure 6.6: The average SED of PG 1553+113 measured in March-April 2008. The empty triangles denote the REM data, the open square represents the KVA data, the open circle denotes the Abastumani data, and the open square denotes *R*XTE/ASM data. The arrow at HE denotes the AGILE upper limit. The empty squares in VHE range are the deabsorbed MAGIC data. We also show the non-simultaneous flux points from *Fermi* (bowtie) and *Swift*/BAT (small filled circle).

23 respectively) and the size of emission region (1.3×10^{16} and 1.16×10^{16} respectively) are comparable, while the magnetic field is 0.7 G in both cases. The major difference in SED is arising from the difference in EED. However, in order not to effect the differerence in different models, we fit the previous result with Tavecchio2001 [225] SSC model. The difference between two different states of the source arises from the EED, however the slopes and $\gamma_{\rm max}$ remain constant. The $\gamma_{\rm min}$ and $\gamma_{\rm b}$ of the previous observation are found to be 3×10^3 and 2.7×10^4 respectively.

During this campaign, no significant variability of VHE flux is found. The integral flux (E>200 GeV) during these observations is $1.3 \pm 0.3 \times 10^{-7}{\rm cm}^{-2}{\rm s}^{-1}$ while during the

Instrument	log(ν [Hz])	log(νF(ν)) [erg cm^{-2} s^{-1}]
KVA	14.63	-10.17
Abastumani	14.63	-10.08
REM	14.38	-10.33
	14.27	-10.34
	14.13	-10.38
XTE	18.03	-10.3

Table 6.3: Effective frequencies, and corresponding fluxes from PG 1553+113 from KVA, Abastumani, REM and RXTE instruments obtained during this campaign.

first observations that was $1.0 \pm 0.4 \times 10^{-7}$cm^{-2}s^{-1}. The X-ray flux[2] increases by about a factor of two, while the averaged X-ray flux during 39 months of *Swift*/BAT observation agrees with our SED. Optical flux during our first observation and current observation does not show any significant variability. The *Fermi* bowtie and lowest-energy MAGIC data points together with the model fit indicate a variability at HE or VHE γ-rays.

Our results suggest that the variability of PG 1553+113 at different frequencies is time dependent: hence, only a simultaneous multi-frequency monitoring campaign over a large time span will give more information on the source. Relative to this fact, it is worth mentioning that the AGILE and MAGIC data presented here constitute the first simultaneous broad-band γ-ray observation (and ensuing SED) of any blazar, though the first simultaneous detection accomplished during the multi-frequency campaign of Mkn 421 (Donnarumma2009 [86]), and the first broad-band γ-ray spectrum was obtained from PKS 2155-304 (Aharonian2009b [27]) by HESS and *Fermi*.

[2]Note that the X-ray data used in Albert2007a [34] was not taken simultaneously with VHE and optical data.

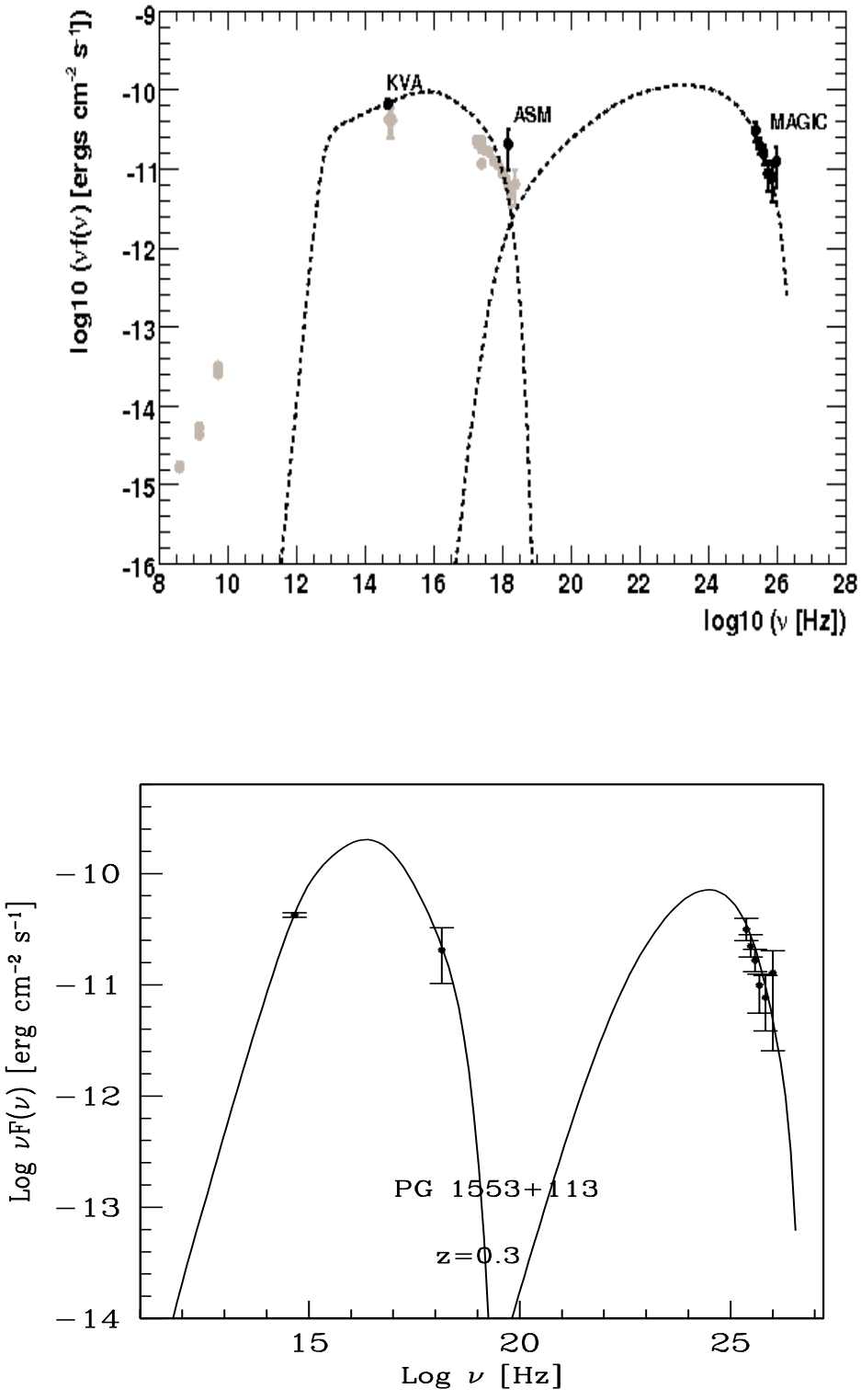

Figure 6.7: Top: The SED fit of Albert2007a [34] using Giommi2002 [124]. Bottom: The same SED has been reproduced using Tavecchio2002 [226] SSC model.

7

Variability in AGN

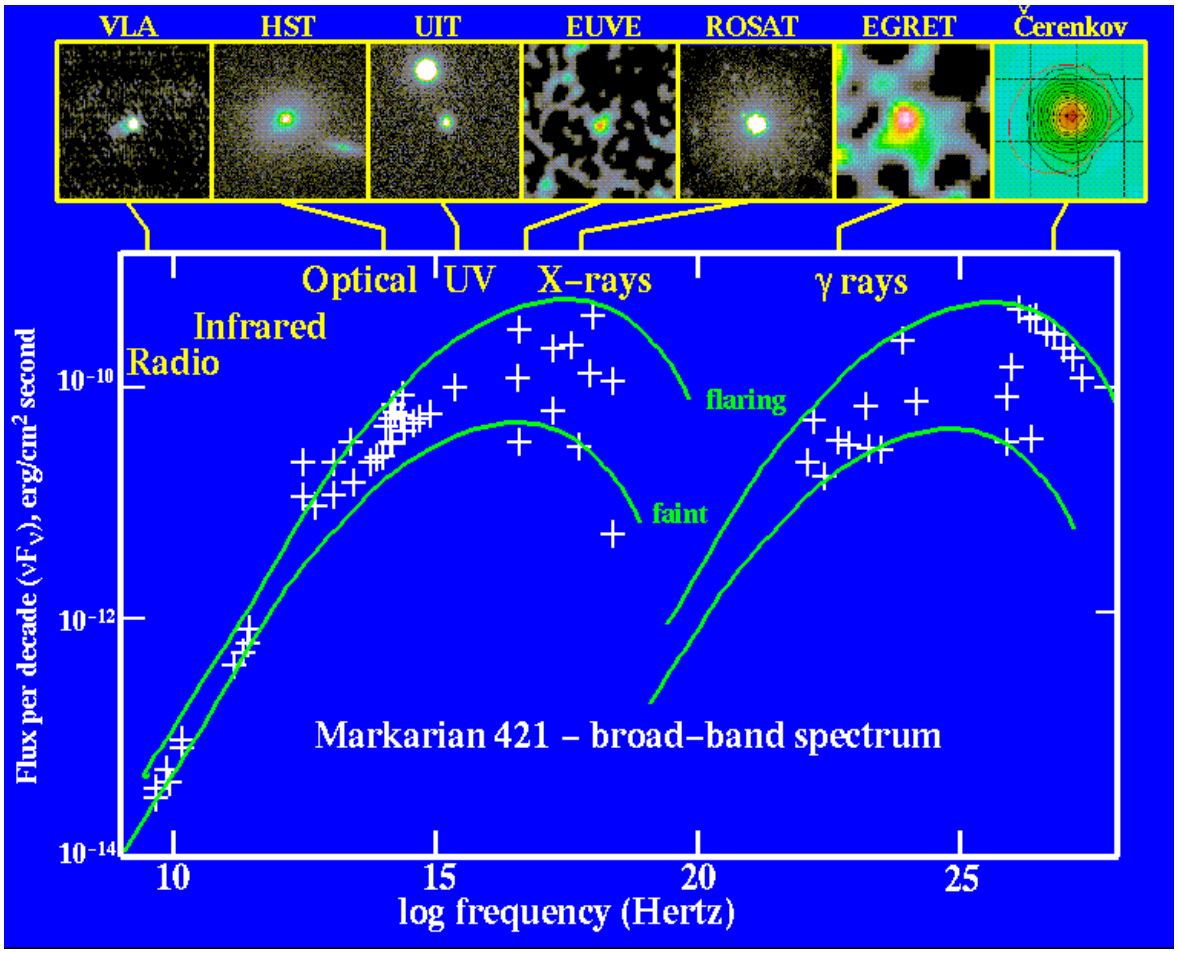

Figure 7.1: An illustration of SED in faint and flaring state (taken from Wu2010 [247])

7.1 Introduction

Blazars often undergo rapid variability in all frequencies, including VHE γ-ray region. The variability of fluxes range from a few percent to more than hundred percent (Varies2005 [234]). Variability timescale can be in the order of weeks, days or even minutes. Very fast variability has been reported from Mkn 501 (Albert2007d [37]) and PKS 2155-304 (Aharonian2007 [21]) on timescale of few minutes. More about the ultra-fast TeV variability can be found in (Ghisellini2009 [119]). TeV/X-ray and TeV/Optical flux variability correlation has been noted in some blazars (Buckley1996 [72], Catanese1997 [178]). 3C 279, the farthest blazar discovered in TeV range was also detected (Albert2008 [40]) during a high optical state. However no correlation was found in some cases, like the orphan TeV flare of 1ES 1959+650 (Krawczynski2004 [155]) and the childless X-ray flares of Mkn 421 (Gliozzi2006 [126]).

Studying the differences in variability of different AGN will provide the understanding of physics involved in such flaring events. In order to estimate the emission parameters of the AGN, we introduce a χ^2 minimization procedure. In this chapter we discuss the effect of variability of emitting particles in AGN variability using the same SSC model and EBL model for all data sets, and emphasize the need of more simultaneous multiwavelength and more precise data of AGN in different variability state.

7.2 χ^2 minimization of SSC model

Even though SSC model was proposed a few decades ago, SSC model fit is performed as an *eyeball* fit, hence a χ^2 minimization was never introduced. This can be due to the complexity of the SSC function of 9 parameters, and comparatively less number of observed points (Often the number of observed points were less than the number of parameters used in SSC model). However, in the present era, four frequency ranges are available for an AGN observation: optical, X-ray, HE and VHE. So, it is highly useful to introduce a χ^2 minimization for SSC model.

We adapted the libraries from Numerical recipes in C (Press1993 [189]) for the minimization procedure. We use Levenberg-Marquardt minimization method. It was developed for a minimization of a function. However the IDL software, which calculates the

SSC function, provides output in numerical form. So we modified the code in order to calculate the derivative of the function in each step. The code starts with an initial set of parameters in order to produce a preliminary SSC model. During each pair of sub runs the code estimates the derivative of the function with respect to one parameter. As there are 9 parameters in SSC model, the code should run 19 times for a specific point in the parameter space ($2 \times 9 + 1$). The χ^2 determination in each step is not straight forward, due to the numerical output of IDL. The code extrapolates the output of IDL program according to the observed points in each steps, if needed. The information on the derivative of the function is used to find the direction and the increment of the parameter in the next step.

We applied our minimization code in simple functions such as a parabola, using the numerical values with a small percentage of spread, to test the code. We then applied the code on an SSC model which was fitted by another χ^2 method (see Mankuzhiyil2010 [165]), and found that the results are consistent. The code takes around 20 minutes to give the best fit output. An example of the χ^2 output during different stages of the code run is shown in Fig.7.2.

7.3 Source selection

For this work, we selected the sources based on two criteria: (1) The source should be simultaneously observed at least in X-rays and VHE (2) The simultaneous observation has to be carried out at least twice. The selected sources are Mkn 421, Mkn 501, and PKS 2155-304 (see Table 7.1). The blazar 1ES 1101-232, which was observed in two different flaring states (Aharonian2007d [23]) was not selected because of the large uncertainty in the VHE spectrum.

Among BL Lacs, the nearby sources Mkn 421 and Mkn 501 are the brightest at X-rays and VHE. As the source redshifts are z=0.030 and z=0.034 respectively, comparatively less EBL attenuation makes these sources as favourite of IACTs, and hence the best studied BL Lacs in VHE. Mkn 421 is the first established TeV emitting AGN (Punch1992 [190]). The source went to high flaring state a few times (Gaidos1996 [108], Aharonian2002 [10], Acciari2009 [8]). The correlated variability of the source in all frequencies suggests a single population of particle may be responsible for the radiation. Mkn 501 is the second

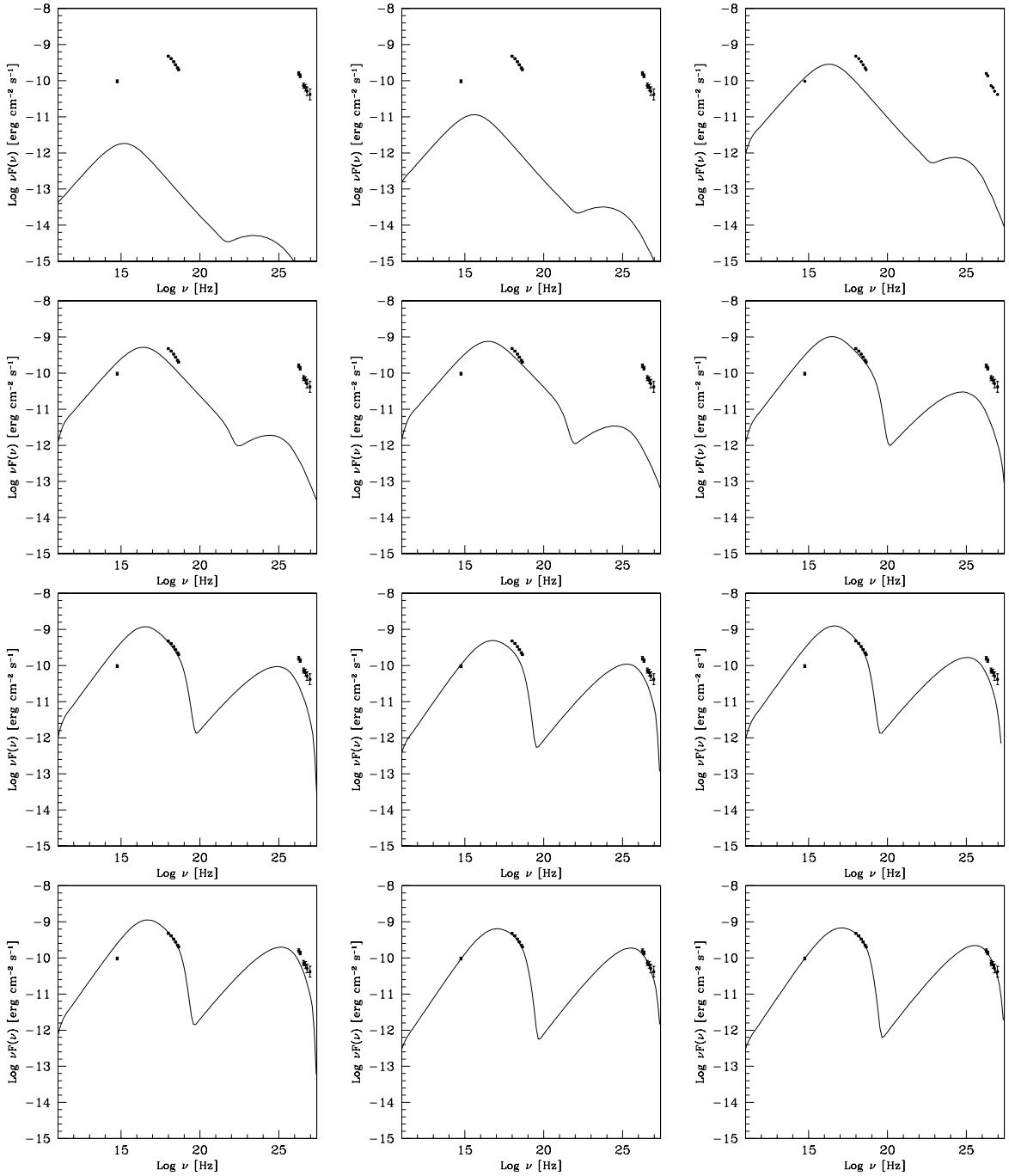

Figure 7.2: Plots during the χ^2 fit code progresses.

established TeV emitting AGN (Quinn1996 [191]). The source went to a high activity in 1997 (Aharonian1999 [9]) such that the integral flux at 1 TeV was 10 times that of the Crab Nebula. The source went to another flare activity in 2005 (Albert2008c [42]). Mkn 501 has been a target of many mwl campaigns, however most of them were not simultaneous campaigns. The TeV emission from PKS 2155-304 was first detected by Chadwick1999 [75]. Being in southern hemisphere, it was detected several times by HESS, however the source can be observed only in higher zenith angles by MAGIC (Hadasch2009 [133]).

7.4 Results and conclusion

We successfully fit all data sets with SSC model described in Tavecchio2001 [225] using χ^2 minimization. The parameters in the model are electron population lorentz factors $\gamma_{\rm min}$, $\gamma_{\rm b}$, $\gamma_{\rm max}$, the slopes of the broken power law of the electron spectrum n_1, n_2, the density of electron population k, the Doppler facotr δ, magnetic field B, and the radius of emission region R. However we assumed $\gamma_{\rm min} = 1$, such that the total parameters in the model is 8. In order to correct the VHE flux due to the EBL absorption, the optical density values provided by Franceschini2008 [107] is used.

The parameters obtained in the χ^2 minimized SSC models are given in Table 7.2, 7.3 and 7.4. It can be observed that all 8 parameters undergo changes. With the limited number of data sets and the large uncertainty of the parameters it is difficult to reach a conclusion. The large uncertainty is from the error bars of the data. Compared to the optical/X-ray data, error in VHE flux in larger. It is difficult to constrain the second peak of the SSC diagram with observed points of larger error bar VHE data. We have tested our procedure with small errors, and found that we obtain less uncetrain parameters when the VHE flux error is bellow 5%.

Even though our work does not provide any constraints on the SSC parameters in different states, we developed a χ^2 fit on SSC model and tested it on several observed points for the first time. Our result also shows that, with the present IACT telescopes it is difficult to obtain a less uncertain SSC parameters. Our results will be useful in determining the allowed error factors of the future telescopes like CTA.

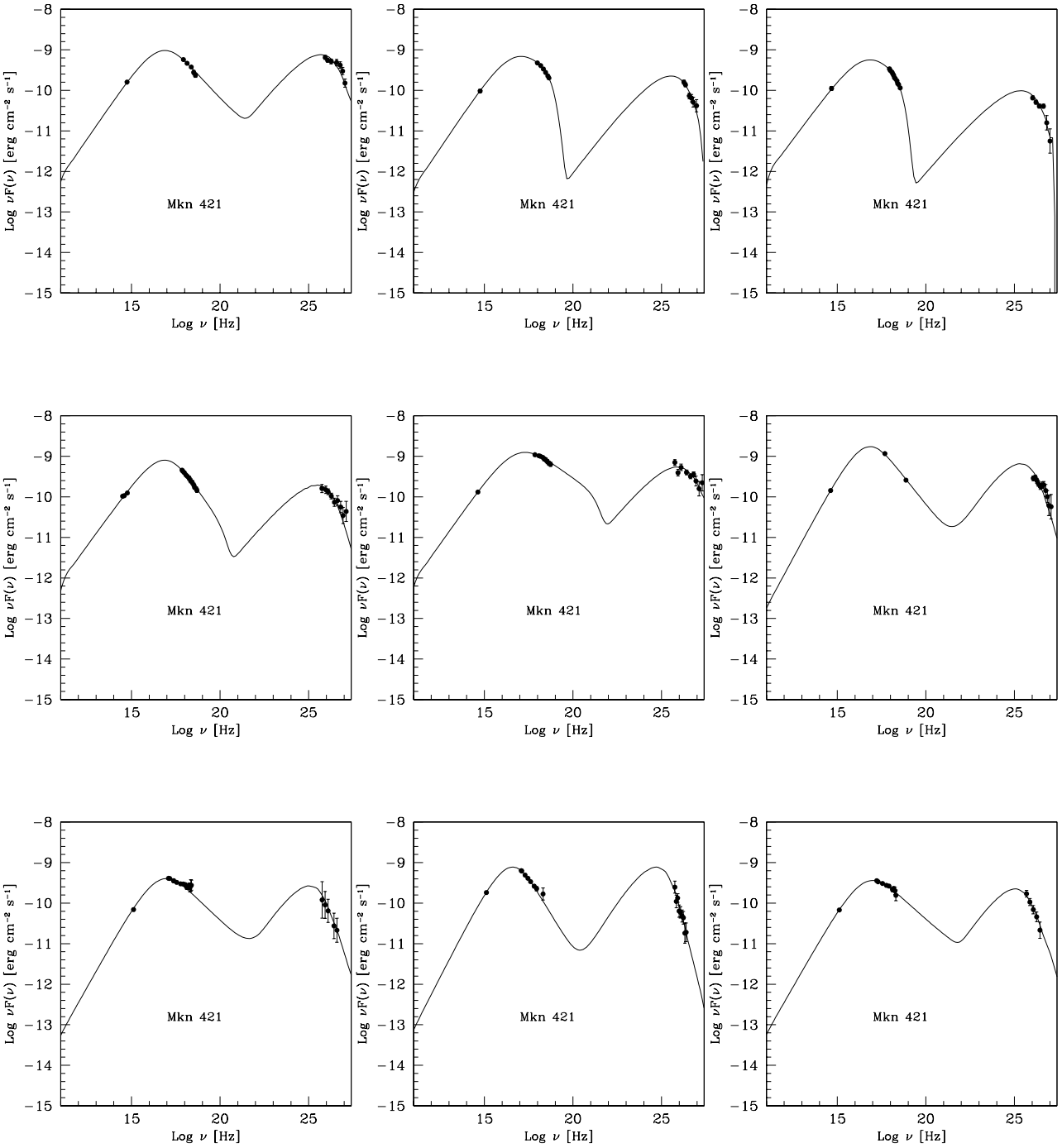

Figure 7.3: SEDs of Nine simultaneous observations of Mkn 421. Top left: Dataset A (higher state). Top center: Dataset A (lower state). Top right: Dataset B. Center left: Dataset C (medium state). Center center: Dataset C (high state). Center right: Dataset E . Bottom left: Dataset D (whipple data). Bottom center: Dataset D (veritas data). Bottom right: Dataset D (magic data).

Blazar	Year	No. of data sets	Referance	Identification letter
Mkn 421	2001	2	Fossati2008 [104]	A
	2002, 2003	1	Rebillot2006 [195]	B
	2003, 2004	2	Blazejowski2005 [66]	C
	2006, 2008	3	Acciari2009 [8]	D
	2008	1	Donnarumma2009 [86]	E
Mkn 501	2006	1	Anderhub2009b [48]	F
	2009	1	Gal12009 [109]	G
PKS 2155-304	2005	1	Aharonian2005c [15]	H
	2006	2	Aharonian2009c [28]	I
	2008	1	Aharonian2009b [27]	J

Table 7.1: Selected data sets for this work. Identification number is used in order to refer the data set in the text.

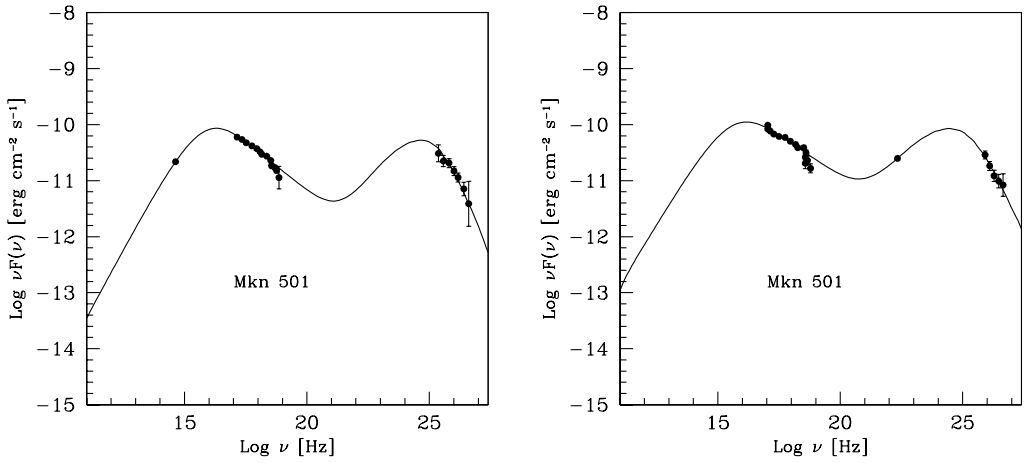

Figure 7.4: SEDs of two simultaneous observations of Mkn 501. Left: Dataset F. Right: Dataset G.

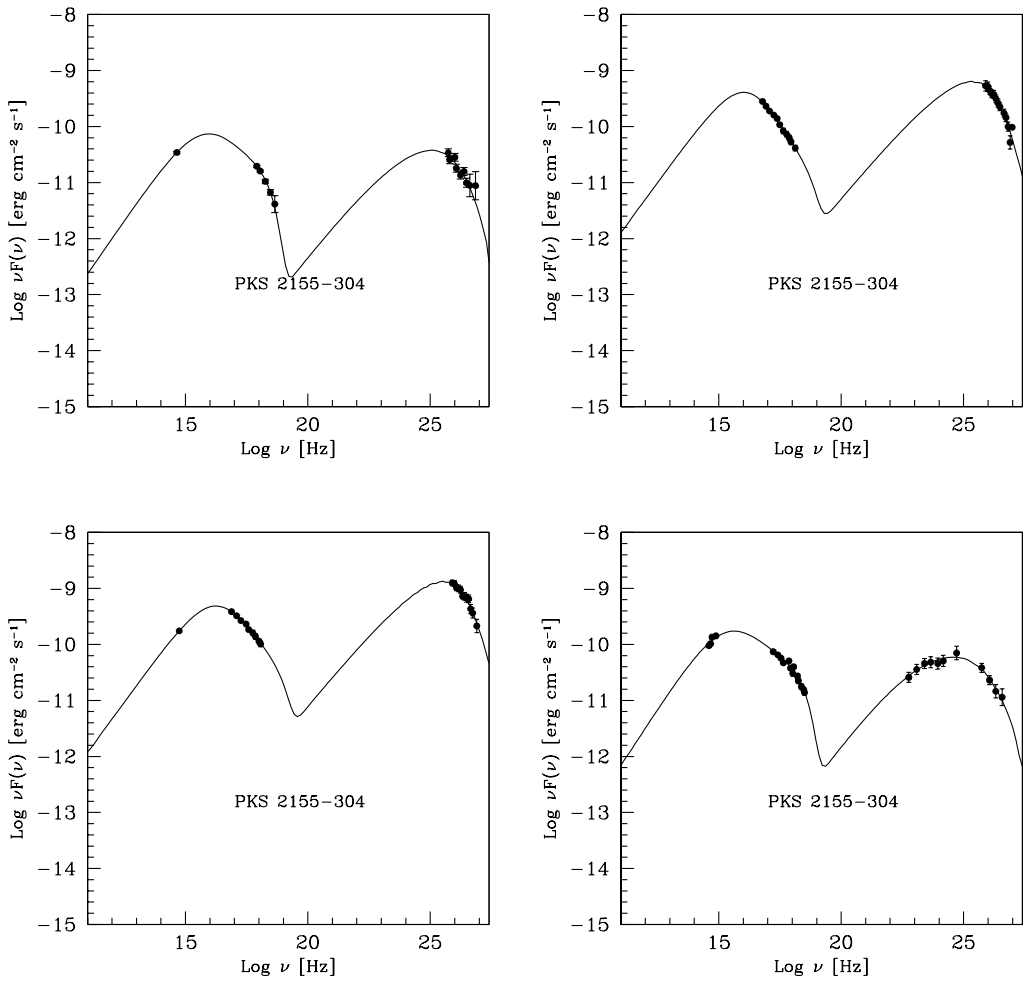

Figure 7.5: SEDs of four different observations of PKS 2155-304. Top left: Dataset H. Top right: Dataset I (low state). Bottom left: Dataset I (high state). Bottom right: Dataset J.

Parameter	Set A (high)	Set A (low)	Set B
γ_b	$(5.43\pm\ 3.9)10^4$	$(3.69\pm\ 2.2)10^4$	$(3.37 \pm 0.85)10^4$
γ_{max}	$(8.43\pm\ 2.05)10^6$	$(3.17\pm\ 0.5)10^5$	$(2.48 \pm 0.07)10^5$
n_1	1.72 ± 0.35	$1.70\pm\ 0.35$	1.82 ± 0.06
n_2	3.96 ± 0.13	3.68 ± 0.42	3.8 ± 0.4
B (G)	$0.06\pm\ 0.05$	0.14 ± 0.035	0.12 ± 0.01
K (cm^{-3})	$(2.71 \pm 17.2)10^3$	$(2.17\pm\ 6.9)10^3$	$(2.92 \pm 1.4)10^3$
R (cm)	$(1.43\pm\ 3.76)10^{15}$	$(9.32\pm\ 2.03)10^{14}$	$(1.21 \pm 0.42)10^{15}$
δ	85.3 ± 80.02	74.3 ± 13.73	84.9 ± 22.07
χ^2/d.o.f	1.56	0.30	1.40
Parameter	**Set C (med)**	**Set C (high)**	**Set D (W)**
γ_b	$(4.37 \pm 2.63)10^4$	$(5.95 \pm 5.43)10^4$	$(2.49\pm\ 0.77)10^4$
γ_{max}	$(1.69 \pm 0.05)10^6$	$(8.69 \pm 4.80)10^6$	$(9.74\pm\ 9.60)10^6$
n_1	1.80 ± 0.19	1.77 ± 0.51	$1.44\pm\ 0.13$
n_2	4.2 ± 0.12	3.62 ± 0.3	3.84 ± 0.12
B (G)	0.18 ± 0.05	0.07 ± 0.05	0.80 ± 0.17
K (cm^{-3})	$(2.82 \pm 6.35)10^3$	$(2.4 \pm 1.4)10^3$	$(9.92 \pm 180.4)10^2$
R (cm)	$(1.18 \pm 1.76)10^{15}$	$(1.36 \pm 2.04)10^{16}$	$(6.62\pm\ 3.44)10^{14}$
δ	84.9 ± 59.7	96.7 ± 68.6	25.77 ± 33.78
χ^2/d.o.f	0.70	0.72	1.47
Parameter	**Set D (V)**	**Set D (M)**	**Set E**
γ_b	$(1.71 \pm 0.95)10^4$	$(2.70 \pm 2.37)10^4$	$(2.48 \pm 1.45)10^4$
γ_{max}	$(1.05 \pm 0.17)10^7$	$(7.01 \pm 1.78)10^6$	$(1.65 \pm 0.42)10^7$
n_1	1.29 ± 0.21	1.47 ± 0.27	1.37 ± 0.32
n_2	4.44 ± 0.16	3.79 ± 0.21	4.10 ± 0.09
B (G)	1.14 ± 1.11	0.76 ± 0.93	0.27 ± 0.14
K (cm^{-3})	$(5.46 \pm 9.27)10^2$	$(9.1 \pm 11.4)10^2$	$(1.96 \pm 5.85)10^2$
R (cm)	$(6.5 \pm 10.2)10^{14}$	$(8.49 \pm 10.89)10^{15}$	$(7.49 \pm 9.46)10^{14}$
δ	24.4 ± 32.93	22.64 ± 9.49	75.61 ± 34.06
χ^2/d.o.f	0.54	0.55	1.55

Table 7.2: The obtained parameters and χ^2 from Mkn 421 data sets. Low, med and high labels are used to identify the data sets when a reference contain more than one data set. W, V and M refer to Whipple, Veritas and MAGIC data respectively.

Parameter	Set F	Set G
$\gamma_{\rm b}$	$(1.42\pm\ 1.00)10^4$	$(1.10\pm\ 0.69)10^4$
$\gamma_{\rm max}$	$(1.62\pm\ 0.41)10^7$	$(1.32\pm\ 1.17)10^6$
n_1	$1.38\pm\ 0.64$	$1.55\pm\ 0.59$
n_2	$3.70\pm\ 0.06$	3.68 ± 0.45
B (G)	$0.39\pm\ 0.73$	0.41 ± 0.45
K (cm^{-3})	$(5.62 \pm 30.47)10^2$	$(4.54\pm\ 17.78)10^3$
R (cm)	$(7.92\pm\ 3.10)10^{14}$	$(7.27\pm\ 6.00)10^{14}$
δ	$26.90\pm\ 28.32$	$29.2\pm\ 21.2$
χ^2/d.o.f	0.85	1.43

Table 7.3: The obtained parameters and χ^2 from Mkn 501 data sets.

Parameter	Set H	Set I (low)	Set I (high)	Set J
$\gamma_{\rm b}$	$(3.69\pm\ 1.44)10^4$	$(7.78\pm\ 2.68)10^4$	$(9.34 \pm 6.32)10^4$	$(1.74 \pm 0.4)10^4$
$\gamma_{\rm max}$	$(7.26\pm\ 1.45)10^5$	$(1.58\pm\ 0.39)10^6$	$(1.91 \pm 0.91)10^6$	$(5.93 \pm 1.13)10^5$
n_1	$1.73\pm\ 0.17$	$1.81\pm\ 0.26$	1.8 ± 0.59	1.65 ± 0.14
n_2	$3.81\pm\ 0.38$	4.38 ± 0.14	4.13 ± 0.28	3.72 ± 0.09
B (G)	$0.02\pm\ 0.01$	0.009 ± 0.007	0.01 ± 0.005	0.03 ± 0.006
K (cm^{-3})	$172.26\pm\ 321.51$	$239.71\pm\ 642.58$	388.15 ± 2677.5	116.82 ± 162.97
R (cm)	$(1.64\pm\ 0.65)10^{16}$	$(4.13\pm\ 3.96)10^{16}$	$(3.77 \pm 5.09)10^{16}$	$(1.53 \pm 1.08)10^{16}$
δ	$55.32\pm\ 15.27$	$57.48\pm\ 23.72$	49.73 ± 26.77	70.85 ± 27.3
χ^2/d.o.f	1.22	0.61	0.30	0.34

Table 7.4: The obtained parameters and χ^2 from PKS 2155-304 data sets. Low and high labels are used here to identify the data sets when a reference contain more than one data sets.

8

Estimation of EBL density

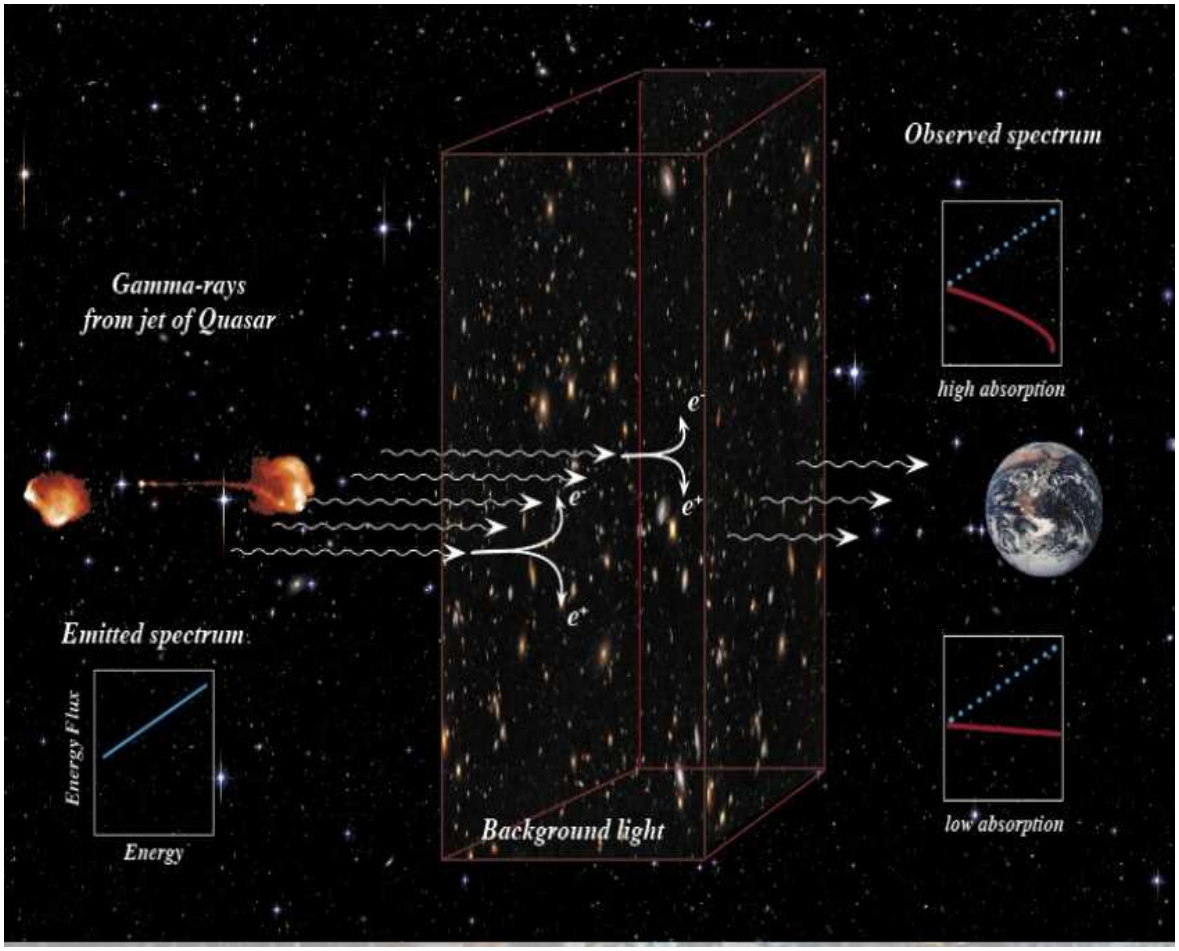

Figure 8.1: An illustration of γ-ray absorption by EBL (taken from [91]).

8.1 Introduction

The EBL, both in its level and degree of cosmic evolution, reflects the time integrated history of light production and re-processing in the Universe, hence the history of cosmological star-formation. Roughly speaking, its shape must reflect the two humps that characterize galaxy SEDs: one arising from warm dust emission and peaking at $\lambda \sim 100\,\mu$m (infrared background), and one arising from starlight and peaking at $\lambda \sim 1\,\mu$m (optical background).

Direct measurements of the EBL are hampered by brighter foreground like night-sky glow, zodiac light from the inter planetary dust, diffuse dust in the Galaxy. So, direct measurements are possible only in energy bands where the contribution of foreground is lower, ie, around 1μm and $100\,\mu$m (Hauser2001 [139]). The Cosmic Background Explorer (COBE) satellite has detected EBL at 140 μm and 240 μm, with two instruments: Diffuse Infrared Background Experiment (DIBRE) and the far Infrared Spectrometer (FIRAS). The FIRAS measurements (Fixsen1998 [102]) shows that a modified blackbody spectrum can well represent the band between 125 μm and 2000 mm. However, the detection at 60 μm and 100 μm are under controversy (Blain2002 [65]). The measurement of optical and NIR region, using IRTS satellite is considerably higher than integrated light from galaxies (Matsumoto2000 [170]), which makes the level of EBL emission uncertain by a factor of several.

Many models have been suggested to derive the EBL spectrum based on theoretical assumptions and observational constraints. These models can be grouped in to three (Hauser2001 [139]). (i) Backward evolution model (ii) Forward evolution model (iii) Semi-analytic Model.

Backward evolution models consider current observations of galactic spectra as a function of luminosity, and extrapolate them backward in time using redshift evolution of galaxy emissivity data. Interactions and merging of galaxies are generally not taken into consideration in these models. A number of authors have used this approach to estimate EBL: Kneiske2002 [149], Kneiske2004 [150], Razzaque2009 [194] use star formation rate, where as Franceschini2008 [107] use luminosity functions. Stecker2006 [219] use local galaxy population, by assuming that the change of luminosity varies with redshift according to a power law.

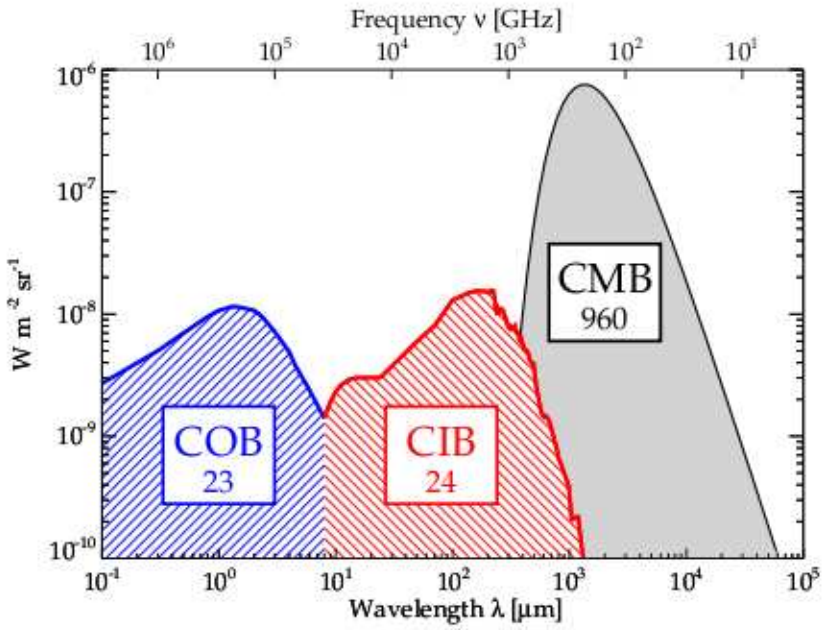

Figure 8.2: A drawing showing the background radiation. the first spike arises mainly from the star light, where as the second peak arises from the absorption and re-emission of light by dust particles. Third peak, cosmic microwave background (CMB) is blackbody radiation from Big Bang. The first two peaks are termed as EBL, which is the second largest background radiation, after CMB.

Forward evolution models are based on the theoretical frameworks of structure formation and evolution, and estimate the luminosity functions forward in time, beginning with cosmological initial conditions. Rocca-Volmerange1996 [198], Franceschini1996 [106] models are a few examples of this approach. These models have been successful in explaining the UV-far IR spectra of various types of galaxies. However, a major draw back of these models are that, they ignore morphological evolution of galaxies, galaxy interactions and stochastic changes in star formation rate.

Semianalytical models are modified approach for forward evolution models. In this approach, some physical processes parameters are also used in addition to the forward evolution parameters, for numerical integration. These physical process involve cooling of gas in star halos, feedback mechanism that retards star formation efficiency, stellar inter magnetic field etc. The approach used in Somerville [212], Gilmore2009 [123] are semi-analytical in nature.

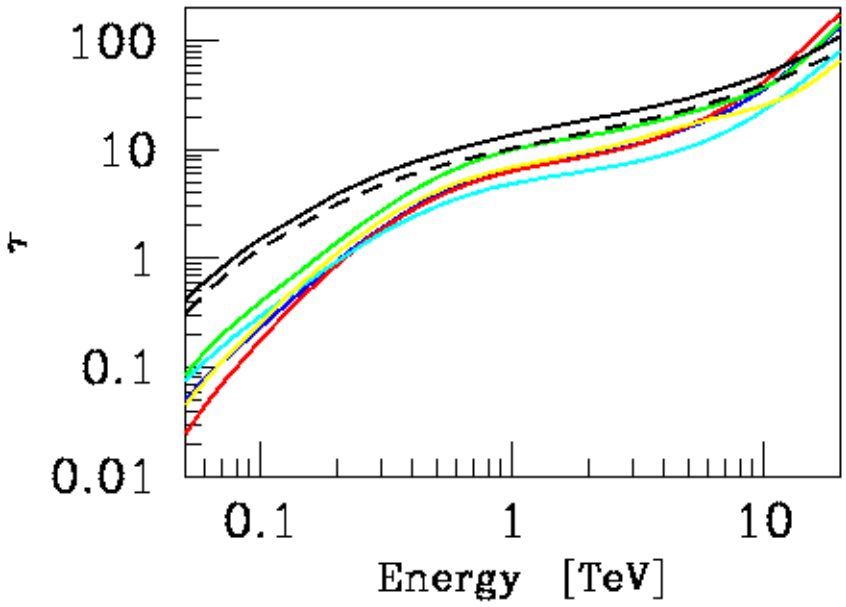

Figure 8.3: Comparison of τ at redshift $z = 0.5$, derived from popular models of EBL. Blue line: Gilmore2009 [123], red line: Franescini2008 [107], green line: Kneiske2004 (star formation rate) [150], cyan line: Raue2008 [193], black line: Fast evolution fit; black doted line: Stecker2006 baseline fit of Stecker2006 [219]. It can be seen that Stecker2006, calculates high EBL density compared to other models.

8.2 EBL absorption

The cross section for the reaction $\gamma\gamma \rightarrow e^+e^-$ is

$$\sigma_{\gamma\gamma}(E,\epsilon) \;=\; \frac{3}{16}\,\sigma_{\rm T}\;(1-\beta^2)\;\times \\ \times\;\left[2\,\beta\,(\beta^2-2)\;+\;(3-\beta^4)\;\ln\frac{1+\beta}{1-\beta}\right] \qquad (8.2.1)$$

(Heitler 1960), where $\sigma_{\rm T}$ is the Thompson cross section and $\beta \equiv \sqrt{1-(m_e c^2)^2/E\epsilon}$.

Purely for analytical demonstration purposes let us assume, following Stecker et al. (1992), that $n(\epsilon) \propto \epsilon^{-2.55}$ is the local number density of EBL photons having energy equal to ϵ (no redshift evolution – as befits the relatively low redshifts currently accessible to IACTs), z_e is the source redshift, and the cosmology is flat no-Λ ($\Omega_0 = 1$). The optical

depth due to pair-creation attenuation between the source and the Earth,

$$\tau_{\gamma\gamma}(E, z_e) = \frac{c}{H_0}\int_0^{z_e}\sqrt{1+z}\,\mathrm{d}z\int_0^2\frac{x}{2}\mathrm{d}x \quad \times$$
$$\times \int_{\frac{2(m_e c^2)^2}{Ex(1+z)^2}}^{\infty} n(\epsilon)\;\; \sigma_{\gamma\gamma}\big(2xE\epsilon(1+z)^2\big)\;\; \mathrm{d}\epsilon \tag{8.2.2}$$

where $x \equiv (1-\cos\theta)$ with θ the angle between the photons, and H_0 the Hubble constant, turns out to be $\tau_{\gamma\gamma}(E, z) \propto E^{1.55} z_s^{\eta}$ with $\eta \sim 1.5$.

This calculation, although it refers to an idealized case, highlights an important property of the VHE flux attenuation by the $\gamma_{\mathrm{VHE}}\gamma_{\mathrm{EBL}} \rightarrow \mathrm{e}^+\mathrm{e}^-$ interaction: $\tau_{\gamma\gamma}$ depends both on the distance traveled by the VHE photon (hence on z) and on the photon's (measured) energy E. So the spectrum measured at Earth is distorted with respect to the emitted spectrum. In detail, the expected VHE γ-ray flux at Earth will be:

$$F(E) = (dI/dE)\, e^{-\tau_{\gamma\gamma}(E)} \text{ (differential)} \tag{8.2.3}$$

and

$$F(>E) = \int_E^{\infty}(dI/dE')\, e^{-\tau_{\gamma\gamma}(E')}\mathrm{d}E' \text{ (integral)}. \tag{8.2.4}$$

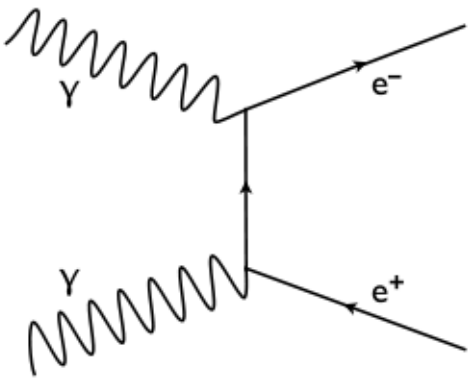

Figure 8.4: Feynman diagram showing the γ-γ pair production.

8.3 EBL absorption as an estimator of EBL density

As proposed by Stecker1992 [218], observation of VHE γ-rays can provide an indirect measurement of EBL, based on the attenuation of the photon flux due to pair-production. According to the relations in the previous section, a typical VHE γ-ray observation can provide an estimation of EBL in $\sim$ 0.1-1.0 μm. A constrain on intrinsic VHE γ-ray spectrum - the spectral slope Γ can not be harder than a theoretical limit - can direct to an estimation of EBL. Applying this idea on 1ES 1011-232 spectrum and assuming an EBL shape, Aharonian2006 [18] calculated the EBL flux (A reverse approach has been performed by Mazin2006 [173], in order to find the redshift of PG 1553+113, assuming a known EBL density). The calculated flux is closer to the EBL lower limit from source counts. A modified attempt was later done by Mazin2007 [174], by fitting the VHE spectrum with different power-laws, over a large grid of EBL shapes to find a possible EBL band. The advantage of this method is that, it does not consider an EBL shape, instead a constrain on VHE spectral slope is used, such that Γ <1.5 (as an extreme case, $\Gamma < 0.67$) and ruled out the possibility of having a rising edge at the higher energy region of the VHE spectrum. Recently, Finke2009 [99] updated the Schroedter2005 [209] method over eight AGNs in different redshifts by assuming the VHE powerlaw Γ <1.5 and $\Gamma < 1.0$. The result obtained was consistent with that of Mazin2007 [174]. However, slope extrapolation of the observed *Fermi*/LAT HE spectrum into the VHE domain exceeds the intrinsic VHE spectrum (Georganopulos2009 [114]), makes the above methods less reliable.

An attempt to measure the EBL used the relatively faraway blazar 3C 279 as a background light source (Stecker1992 [218]) assuming that the intrinsic VHE spectrum was known from modeling and extrapolating the (historical) average broad-band data. However, blazars are highly variable sources, so it is almost impossible to determine with confidence the intrinsic TeV spectrum – which itself can be variable.

In the next session, we propose a method to measure the EBL that improves on Stecker1992 [218] by making a more realistic assumption on the intrinsic TeV spectrum. Simultaneous optical/X-ray/HE/VHE (i.e., eV/keV/GeV/TeV) data are crucial to this method, considering the strong and rapid variability displayed by most blazars.

8.4 The proposed method

The method we are proposing is to estimate the EBL spectrum from the VHE γ-ray spectrum. However this method has to deal with two fundamentally unknown intrinsic VHE spectrum of AGNs. The VHE spectrum has different features in different AGNs. Different spectra can be well described by fundamentally different models, like SSC or EC models. In order to use the AGN VHE spectrum to estimate EBL, one should single out a class of sources that is homogeneous, such that it can described by a single model. This approach will help to minimize biases that may possibly arise from systematically different SED modelings adopted for different classes of sources. So, we propose to choose AGNs whose relativistic jets point towards the observer: Blazars, for three reasons.

1. Most of the observed AGNs belong to the class Blazars

2. Blazars are found to be distributed in a large span of distance

3. Emission model of blazars can be well described by relatively simple emission models.

Within blazars, we suggest to use the sub-class of HBL, because:

1. Their Compton peak can be more readily detected by IACTs than other types of blazar

2. Their HE spectrum can be described as a single unbroken power law in photon energy, unlikely other types of blazar (Lott 2009).

For a given HBL, the method relies on using, a broad-band SED that spans the optical, X-ray, HE γ-ray (from the *Fermi* or AGILE telescope), and VHE γ-ray (from Cherenkov telescopes) bands. However, the HBLs are highly unstable. The variability time scale may range in oder of hours for strong sources like Mkn 421 and Mkn 501, while it is in order of a few days or weeks for most of the other HBLs. In order to avoid the problem arises by using the data of different states for different frequencies, we suggest to use only simultaneous data. A given simultaneous SED will be best-fitted, from optical through HE γ-rays, with a Synchrotron Self-Compton (SSC) model. (Photons with $E < 100\,\mathrm{GeV}$ are largely unaffected by EBL attenuation as long as $z < 1$).

In order to obtain the intrinsic VHE spectrum, we extrapolate the SED into VHE regime, using the same SSC model. Contrasting measured versus intrinsic emission yields a determination of $e^{-\tau_{\gamma\gamma}(E,z)}$, the energy-dependent absorption of the VHE emission coming

from a source located at redshift z due to pair production with intervening EBL photons. Upon assumption of a specific cosmology, the final step is deriving the EBL photon number density.

As blazars are highly variable, they give an advantage of using our method in different variable states. Applying our method on three different states - say, low state, medium state and high state, will improve the accuracy of our method.

Applying the technique on blazars at different redshifts will give us an estimation of τ as a function of z.

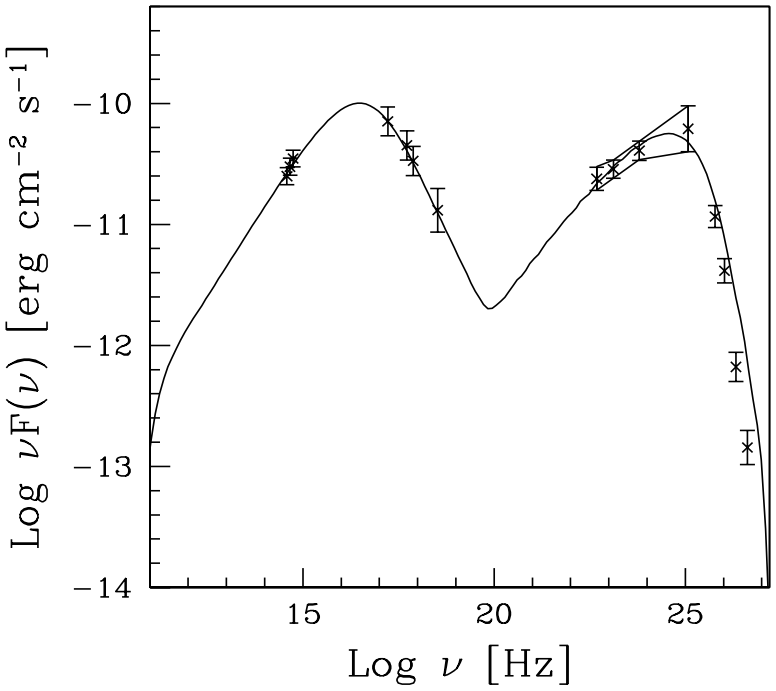

Figure 8.5: Simulated flux points at optical, X-ray HE and VHE γ-ray range, which is the ideal case to use our model, in order to derive the absorption coefficient τ, hence the EBL density. The automatic χ^2 fit is based on the points in optical-HE range. The VHE points fluxes are bellow the SSC fit due to photon absorption by EBL. The degree of absorption increases with energy.

8.4.1 Fitting tecnique: χ^2 minimization

In order to fit the observed optical, X-ray and HE γ-ray flux with the SSC model, a χ^2 minimization is used. In our method, we change the parameters which are described by an 8-dimension vector, in small logarithmic steps. If the variability of the flux is known, the 8-dimension parameters can be reduced to 7-dimension. The γ_{min} of the electron energy population is assumed as 1.

A major problem in this method is, the run time of the χ^2 minimization program, as it deals with 7 parameters over a large span. The recent Fermi 3 months catelogue of bright blazar's emission models are fitted over a large span of parameters (Ghisellini2010 [120]). In order to overcome this problem, two additional features are introduced in the code. The steps of each parameters have been adjusted in each run according to the χ^2 value of the previous run, such that a larger χ^2 results in a larger next step. Pre knowledge of the impact of each parameter is another efficient way to reduce the run time of the program. For example, increasing the value of parameters like magnetic field (B) or radius of emission region (R) always result in increasing the height of synchrotron and compton peak. When the resulting synchrotron/IC peak of the model crosses the roughly estimated synchrotron or IC peak, the program skips next larger parameters of magnetic field or radius, and move in to the next loop.

8.5 Results: application to PKS 2155-304

In order to demonstrate our method, we select the simultaneous observation data of PKS 2155-304, which is currently the only published data match with our requirements (Aharonian2009a [26]). As described in the previous chapter, the first simultaneous braod band γ-ray observation of a blazar, PG 1553+113 does not deliver a HE spectrum, but only an upper limit. Another recent simultaneous observation of Mkn 421 during a flare, could not obtain a HE spectrum as well.

PKS 2155-304 is a blazar at a redshift of $z = 0.12$. It is one of the best studied objects in southern hemisphere. The source was first observed in radio frequency during Parkes survey (Shimmins1974 [211]), and then it was identified as an HBL, from X-ray observation (Schwartz1979 [210]). The VHE regime from PKS 2155-304 was first detected by Mark 6

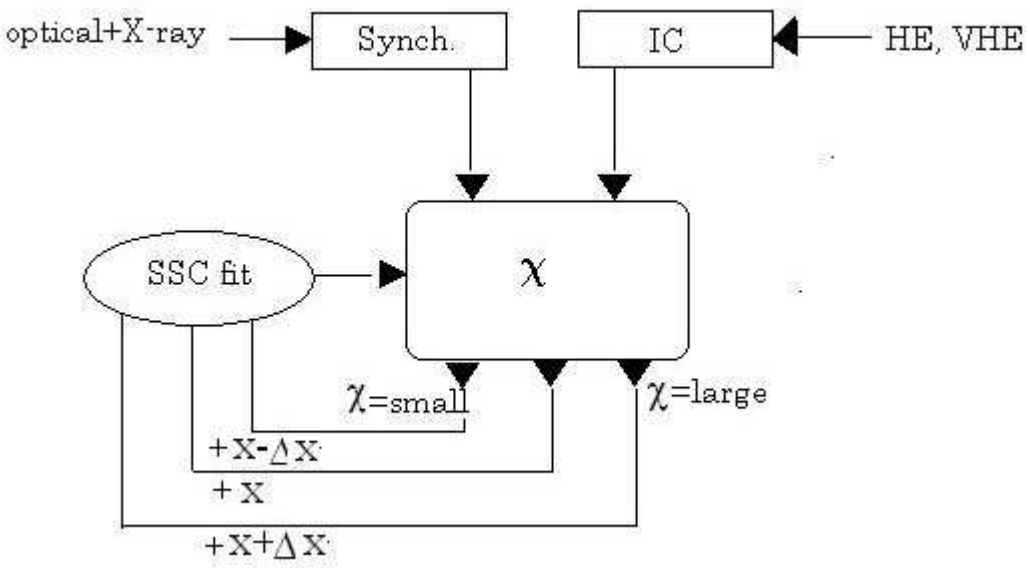

Figure 8.6: Algorithm showing the performance of χ^2 SSC fitting program. The program estimates a very rough synchrotron and IC peak, using the optical, X-ray, HE and VHE data. It calculates the χ^2 value at each run using the SSC code and the observed points, and determine the steps for each parameter in the next loop. If the fit goes above synchrotron or IC estimated peak, the program ignores next values and go to the value in which the fit is lower than the measured points.

Telescope collaboration (Chadwick1999 [75]). It was detected in VHE range, sevaral times by HESS and MAGIC Telescope collaborations.

The simultaneous observation of PKS 2155-304 took place in May 23 - June 9 2008. Optical data was obtained from 0.8 m ATOM optical telescope located in the HESS site. X-ray data was provided by $RXTE$ (with 10 days of coincidence with HESS) ans $Swift$ (towards the end of the campaign). HE data and VHE data were provided by $Fermi$ LAT and HESS respectively. The obtained SED has been fit with SSC model. However in order to reproduce the lower energy component of the SED, a three-component power-law electron distribution is assumed, instead of usual two-component electron distribution.

We apply our procedure in the simultaneous SED data set. However our SSC model uses only two-component electron distribution. Two-component electron distribution is favoured because it is the most commonly used, which will be also used in the data set on

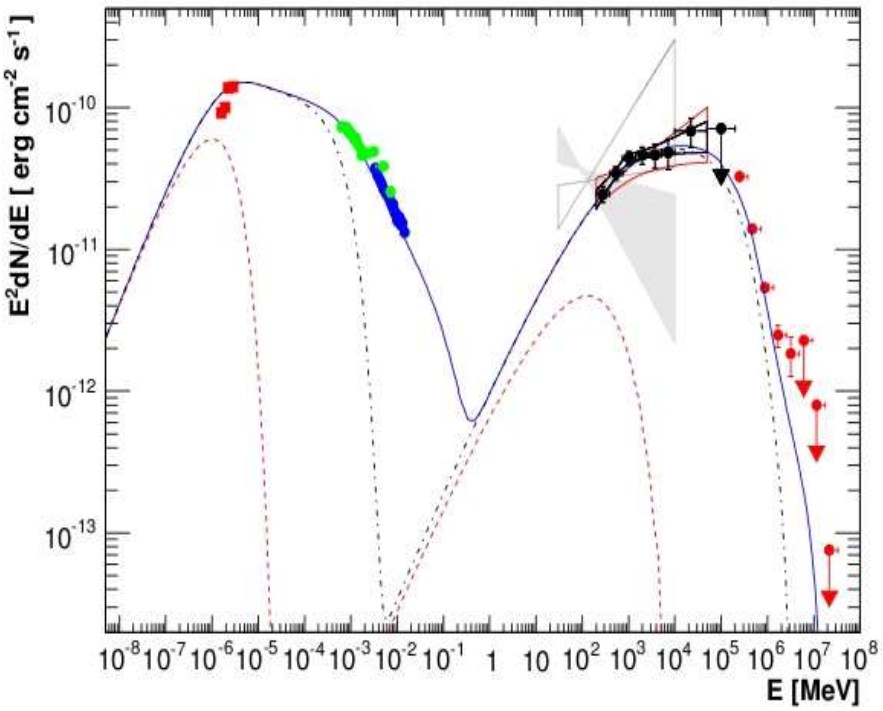

Figure 8.7: Observed flux points from the simultaneous MWL campaign of PKS 2155-304 and corresponding SSC fit used in Aharonian2009a [26]. The optical data are obtained from ATOM telescope, where as X-ray data are from *Swift* (green points) and *R*XTE (blue points). The HE points are from *Fermi* LAT and VHE points are from HESS. The VHE points are observed points where as the fit in VHE part is corrected, considering the EBL attenuation effect.

other blazars simultaneous data also, according to their availability. Another advantage of using a two-component electron distribution is that, the model has two less parameters compared to the parameters of three-component electron distribution model. The parameters, used to model the SSC fit is shown in Table 8.1.

Even though two entirely different SSC models are used Aharonian2009b [27] and this work, the parameters of the models are comparable, except radius of the emission region and the electron number density. While Aharonian et al. using a larger volume of emission region and a smaller electron density, we use a smaller emission region and a larger electron density. However, the total electrons ($\frac{4}{3}\pi R^3 K$) in Aharonian et al 2009 and this work work are 6.8×10^{51} and 36.4×10^{51} respectively.

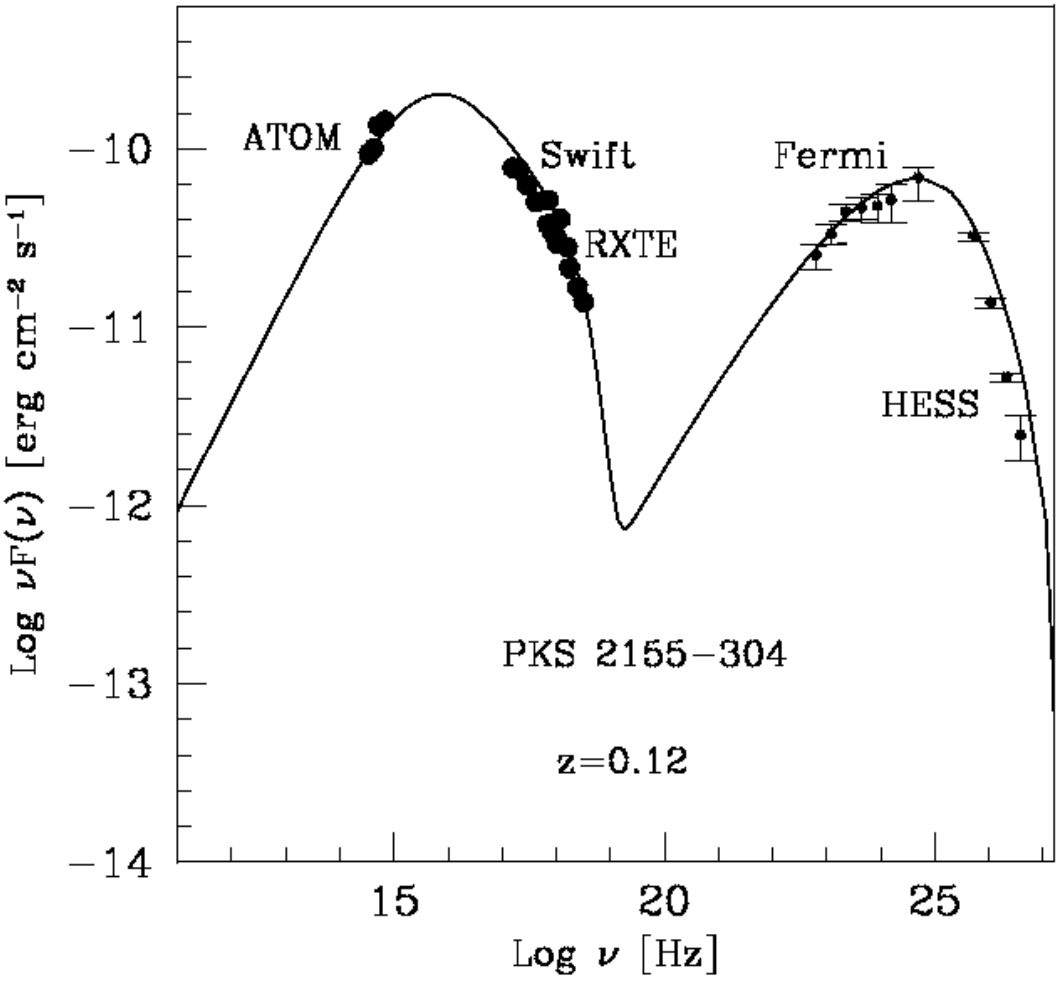

Figure 8.8: The best fit SSC model obtained from the χ^2 fit program. The best fit was estimated from the optical-HE γ-ray flux points. All flux points in the plot are observed

The extrapolation of the model into the VHE γ-ray range clearly lies above the observational H.E.S.S. We attribute this effect to EBL attenuation. By subtracting the flux for each energy points from the corresponding point of the fit give rise to the EBL absorption.

$$log(F_i) - log(F_o) = log(F_i) - log\left(F_i e^{-\tau}\right) = \tau \tag{8.5.5}$$

It is clear that the obtained τ value progressively so with increasing energy. The obtained τ values for each energies is given in Table 8.2. We have used only the first four energy points, and ignored the fifth energy point in the HESS energy spectrum, because it

SSC parameters		
Parameters	Aharonian et al (2009)	This work
$\gamma_{\rm min}$	1	1
$\gamma_{\rm break1}$	1.4×10^4	2.9×10^4
$\gamma_{\rm break2}$	2.3×10^5	NA
$\gamma_{\rm max}$	3×10^6	8×10^5
n_1	1.3	1.8
n_2	3.2	3.8
n_3	4.3	NA
K ($\rm cm^{-3}$)	0.5	150
B (G)	0.018	0.056
R (cm)	$1.5{\times}10^{17}$	3.87×10^{16}
δ	32	29.2

Table 8.1: Comparison of SSC parameters used in Aharonian2009b [27] and our approach. As our approach does not involve a three-component power law, $\gamma_{\rm break2}$ and n_3 are not applicable in it. Every parameters, except the electron population density and the emission region of two models, are comparable.

lies above the energy specctrum, as clearly seen in the SSC fit used in Aharonian2009b [27] (Fig.8.7).

In Fig.8.9, we compare our determination of $\tau_{\gamma\gamma}$ with some recent upper limits or results (Franceschini2008 [107]). Whereas our values are generally compatible with previously published constraints, we note that our values closely agree with the corresponding Franceschini2008 values, which are derived from galaxy number counts and hence represent the light contributed by the stellar populations of galaxies since the epoch corresponding to source redshift $z_{\rm s}$. Our values are also in a good agreement between Gilmore2009 [123] and Finke2009 [99]. However, the values are smaller than the values used in Stecker2006 [219] in both fast evolution fit and baseline fit.

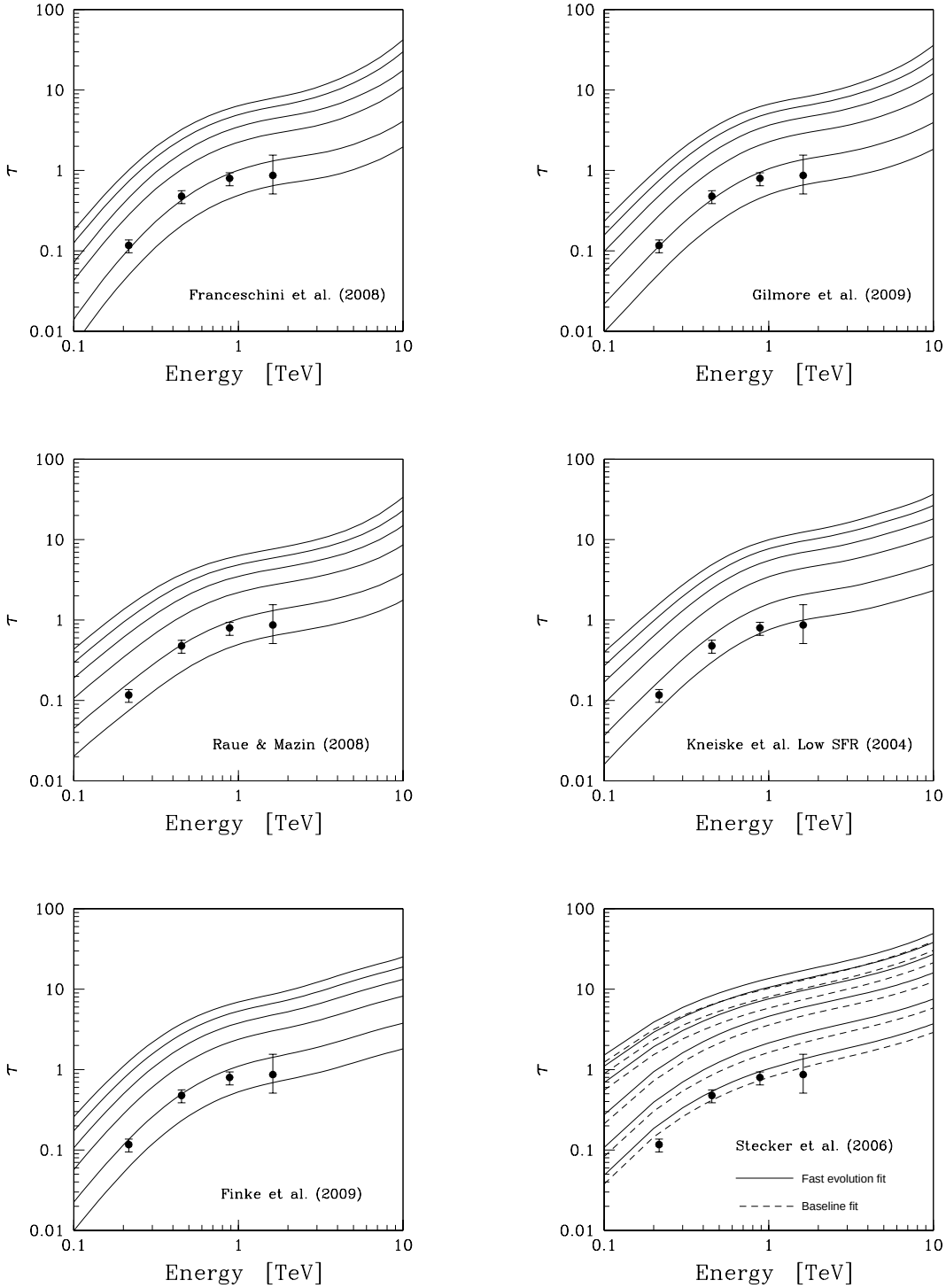

Figure 8.9: Comparison of the obtained τ values with existing models. The lines from bottom to top for each plot corresponds to redshift $Z = 0.05$, 0.1, 0.2, 0.3, 0.4, 0.5.

Energy (TeV)	τ	E_τ
0.23	0.12	0.04
0.44	0.48	0.04
0.88	0.80	0.04
1.70	0.87	0.1

Table 8.2: The obtained optical density τ for each energy points, from our approach. The error (third coloumn) arises from the VHE flux measurement.

8.6 Discussion

The method for measuring the EBL we have proposed in this paper is admittedly depended on the emission model of blazars. However, its only requirement is that all the sources used as background beamlights should have one same emission model. In the application proposed here, we have used a one-zone SSC model where the electron spectrum was a (smoothed) double power law applied to the SED of the HBL blazar PKS 2155-304. While this choice was encouraged by the observational evidence fact that HBLs have, without exception, single-slope *Fermi*-LAT spectra (Lott2009 [163]), we could have as well adopted the choice (Aharonian2009b [27]) of a (broken) triple power law electron spectrum in our search for the best-fit SSC model of PKS 2155-304's SED. Should the latter electron distribution be shown to provide a better fit to HBL *Fermi*-LAT spectra, then it would become our choice. In general, what matters to the application of this method is that all source SEDs be fit with one same SSC model.

Our next goal is to analyze the data of the forthcoming simultanoes MWL campaign on other well-known HBLs in a wide redshift range. Mkn 421 and Mkn 501, being compartively nearer sources would be a good target to apply our approach. The lower energy points are not expected to be far from the SSC fit, as the EBL effect is negligible in lower VHE energy points at lower redshifts.

A

Appendix: Observation of Cassiopeia-A with MAGIC telescope

A.1 Introduction

The analysis details and result of the SNR Cassiopeia (Cas A) data is described here. Cas A is a shell type SNR and a bright source of synchrotron radiation observed at radio frequencies and also in the X-ray band. Its distance is estimated to be 3.4 Kpc. The remnant is seen as a patchy and irregular shell with a diameter of 4' (4 pc at 3.4 Kpc) in optical, X-ray and IR wavelength. The progenitor of Cas A was a Wolf-Rayet star, with an initial mass between 15 and 25 $M_{\odot}$.

A.2 Observation

We observed Cas A between June 2006 and January 2007. After quality cuts the total exposure was 47 hours. The zenith angle ranges from 29° to 45° with an average of 35°. The observation was done in the wobble mode. 86% of the data were taken under moderated Moon light illumination. Anode currents of photomultipliers vary between 1 and 6 μA, due of the Moon light illumination (being 1 μA the anode current for dark observations). The trigger discriminator threshold (DT) was accordingly modified to keep a low accidental trigger rate. The DT level affects the relative γ-ray detection efficiency, decreasing to 0.84 times the efficiency for dark observations, as well as the relative sensitivity, which went to 2.7% of Crab (for dark observation it is 2.5%). The energy threshold rise ($\approx$ 5 GeV) is negligible compared to the rise induced by the intermediate zenith angle observations. Therefore the effects of the moderate Moon light illumination did not reduce substantially the telescope performances.

A.3 Analysis

Dark and moon data were analysed using standard analysis and calibration programs of the MAGIC collaboration. For the cleaning of images absolute tail and boundary cuts of 10 and 5 phe were used respectively. For γ/hadron separation, the shower images were parameterized using the Hillas parameters, and the Random Forest (RF) classification algorithm was used. The RF was trained with a sample of pure γ-ray showers (MC), and a sample of hadron showers (OFF data).

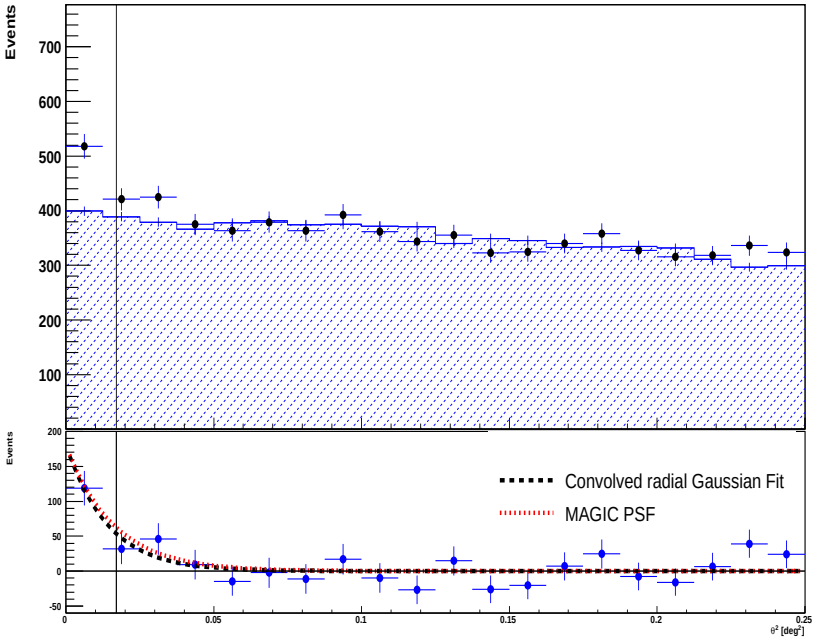

Figure A.1: The θ^2 diagram showing the statistical significance of the γ-like images.

The distribution of θ^2 values is shown in Fig.A.1, where θ is the angular distance between the source position in the sky and the reconstructed arrival position of the air shower. The later position is determined for each shower image by means of the so-called DISP method. In order to determine anti-sources, five symmetrically distributed regions are chosen for each wobble position w.r.t the camera center. Dark Crab data in the same observation conditions of Cas A were used to get an optimum HADRONESS and angular cut. The lower size cut is 400 phe where the MAGIC signal to noise ratio optimizes. The on source events histogram is shown with black points while the off events one in blue shaded. The subtraction of the later from the former shows the excess in the direction of Cas A. The excess $N_{\rm excess}$=157 leads to a significance of 5.2 σ in the region bellow 0.13°.

Skymap shows a background subtracted distribution of reconstructed shower origin centered at the position of Cas A with a lower size cut of 400 phe. The map is smoothened with a Gaussian of σ=0.07^o. By fitting the non-smoothened sky map to a bi-dimensional Gaussian function, the source position is found to be at RA = $23.386\pm0.003_{stat}\pm0.001_{sys}$ h and DEC = $58.81\pm0.03_{stat}\pm0.02^{\circ}_{sys}$.

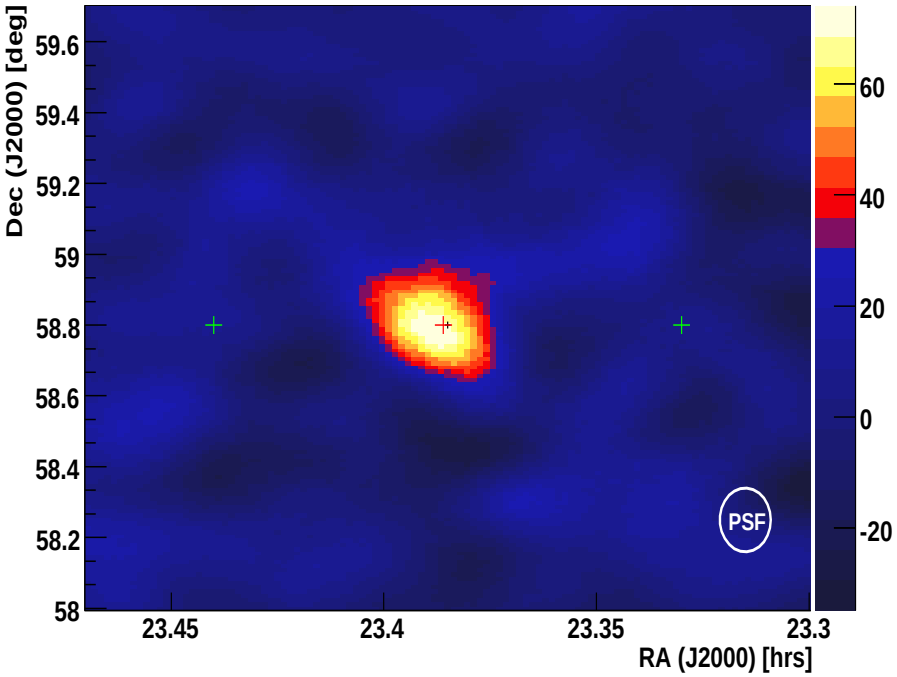

Figure A.2: Sky Map of Cas A region. A cut in SIZE of 400 phe. was applied: the green crosses are the 2 wobble positions; the black cross is the HEGRA c.o.g.; the red cross is the MAGIC c.o.g.

The X-rays and radio diameter of Cas A is 0.08°, which is close to the MAGIC angular resolution. The MAGIC PSF is σ_{psf}=0.090±0.002°. This value was obtained with MC simulations and validated with experimental data (Mkn 421 and Crab Nebula data). The events excess was fitted with a Gaussian function convolved with the PSF (F=$P_1 + P_2 exp(-0.5\ \theta^2/(\sigma^2_{src} + \sigma^2_{psf}))$. The obtained source extension σ_{src} is consistent with a point like source. In Figure A.2 the telescope PSF and the result of the Gaussian fit are shown.

Figure A.3 shows the measured differential energy spectrum. It is well described with a power-law with differential flux at 1 TeV, dN / (dE dA dt) = $(1.0\pm0.1_{stat}\pm0.3_{sys} \times 10^{-12})TeV^{-1}cm^{-2}s^{-1}$ and a photon index of Γ=2.37±0.27$_{stat}$. The spectrum was unfolded using a χ^2 minimization by Gauss-Newton method, with a χ^2/d.o.f of 2.83/3. The systematic error is dominated by the uncertainty in the absolute energy determination and is 30%. For energies above 1 TeV the MAGIC results are consistent with the previous

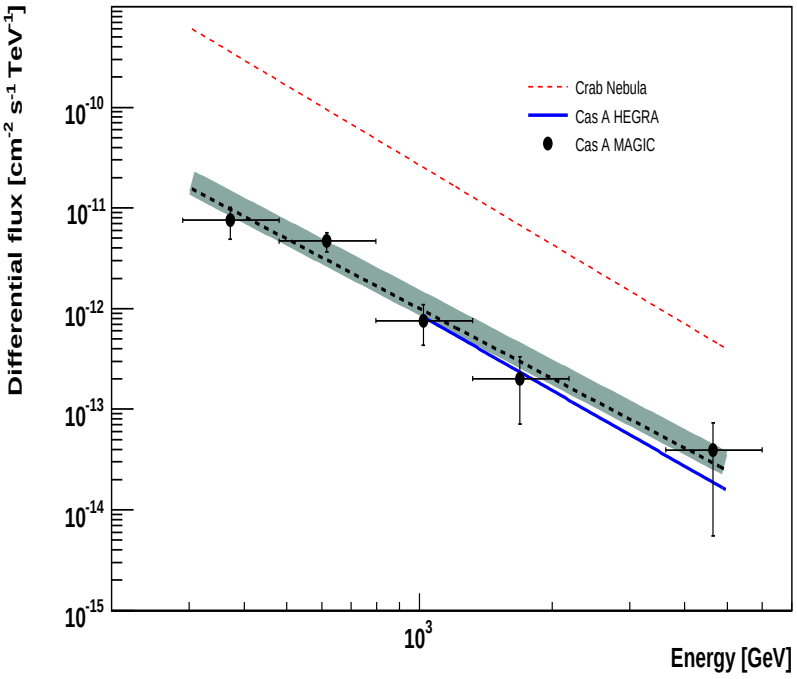

Figure A.3: Cas A spectrum above 250 GeV. The blue line represents the earlier measurement by HEGRA. The red line represents the Crab nebula spectrum. The shaded area is the 1σ statistical error of the fit.

of HEGRA.

This analysis and results have been published in Albert2007a [38].

B

Appendix: Dailycheck software

B.1 Automatic Daily check

Automatic Daily Check software (Autocheck) uses classes of ROOT and MARS. The main duties of the software is to check:

1. subsystems
2. DAQ

The dailycheck has to be performed only at the time of data taking. However, the subsystem information is reported even outside the data taking time. So Autocheck has to filter out these information. The start and end time are obtained by the Daq status: either the daq is in normal run or in calibration run. The subsystem reports are stored in many bins. In order autocheck to check these bins, the time check of each bin is compared with the first and last run time of Daq. This step is performed on almost every subsystem check, as the binning in different subsystem plots can be different. Once the Autocheck finds the starting and end bins, another loop is run over these bins to extract the information, and averaged. These values are later compared with the limits which is defined by experts of each subsystems. In case the values are outside for some runs, it calculates the total time it was outside the limits, and warn the user.

Daq Camera plots has to be treated differently. The camera plots are projected on a histogram. The previously explained procedure is repeated on these plots also.

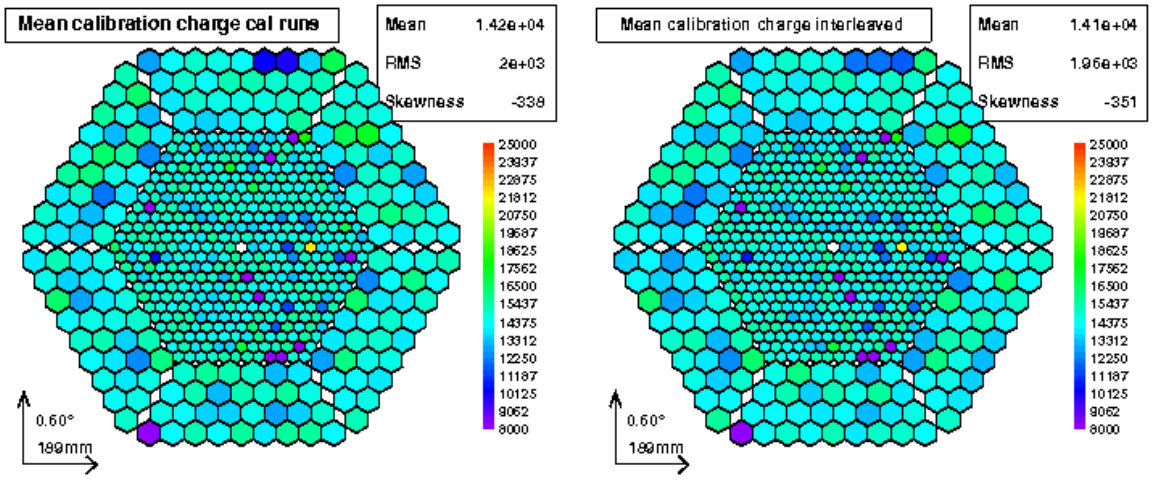

Figure B.1: An example of a Camera plot.

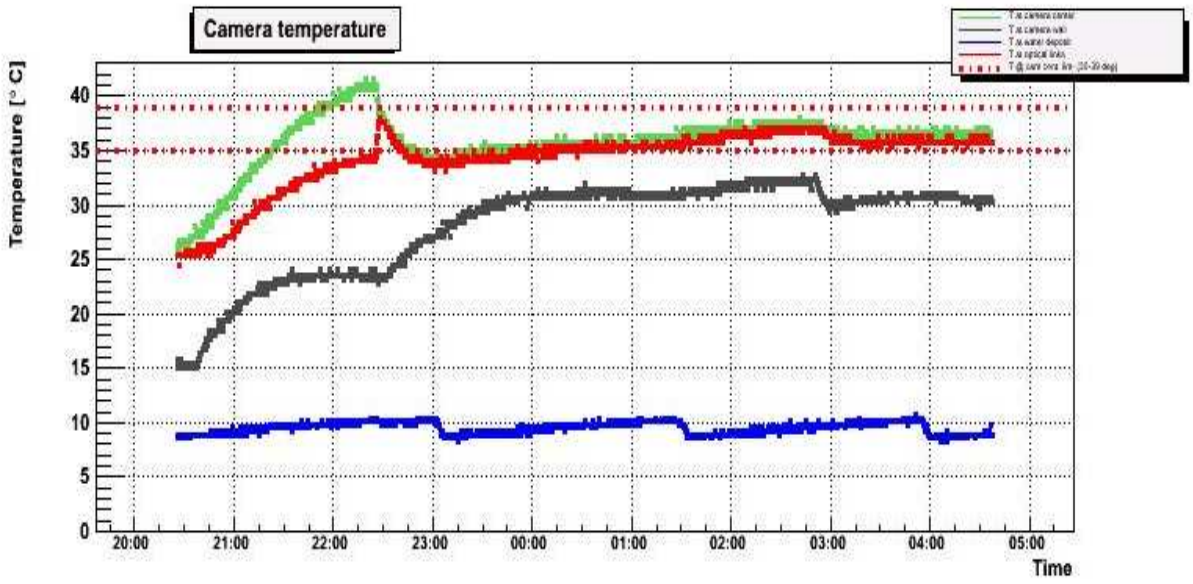

Figure B.2: An example of the Camera temperature.

There are some minor things has to be checked in order to make the Autocheck more precise. For example, during the beginning of data taking, the temperature of the camera increases and then decreases in a few minutes (Fig.B.2); which means the temperature is above limits at least for a few minutes every day. In order not to complain about this daily feature, autocheck has been adjusted such that it performes two different checks: one for the beginning of data taking time and one for the rest.

The autocheck has being running successfully every next day of data taking, for the last two years.

C

Appendix: Fux extrapolator in VHE range

C.1 Flux extrapolator

Flux extrapolator is a software which extrapolates the HE flux from $Fermi$/AGILE satellites into VHE range by considering the EBL absorption. The software is made in user friendly way, which has also a web interface (Figure C.1)

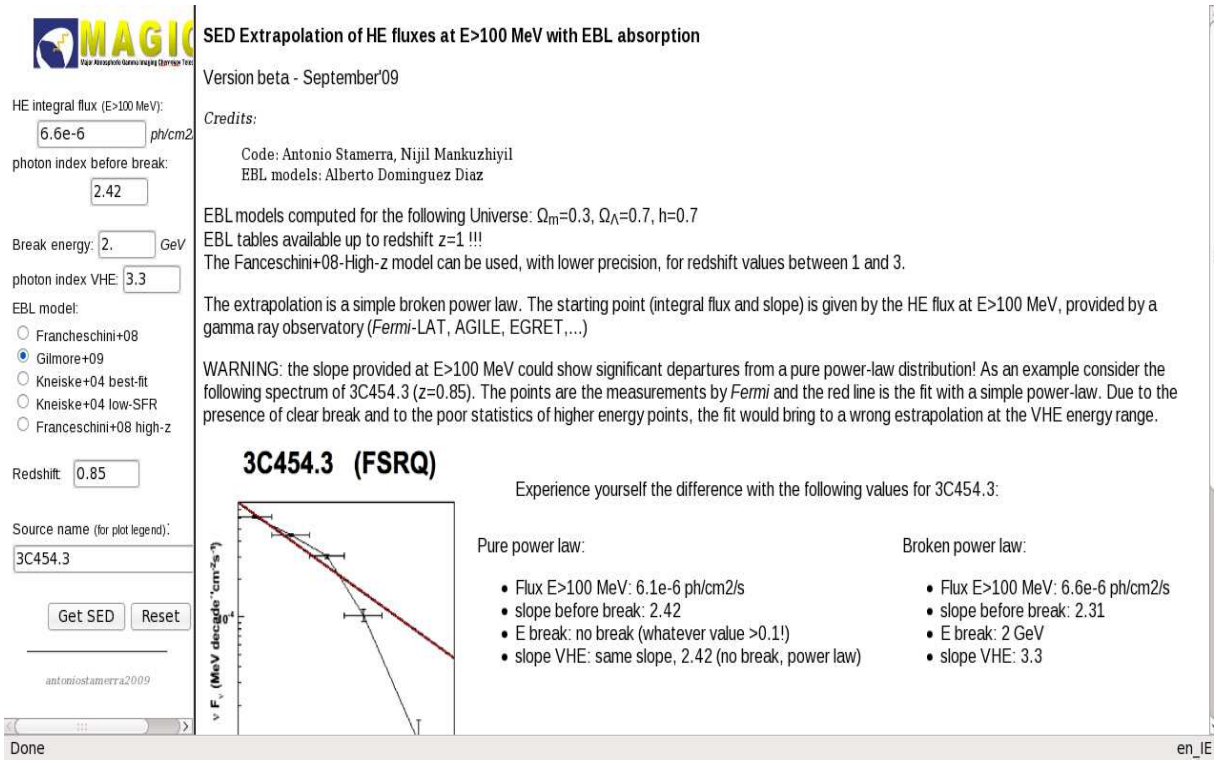

Figure C.1: The web interface of the extrapolator software.

The input values require are: the photon flux above $100\,MeV$ and the slope $s1$ (which can be obtained from $Fermi$/AGILE), slope after the break $s2$ ($\simeq s1+1$) and break energy point ($\sim 100\,GeV$ for HBLs, $\sim 5\,Gev$ for quasars etc.). The software then extrapolates the spectrum into VHE range. EBL attenuation has to be taken care above $100\,GevV$. The program has four options (Frenceschini2008 [107], Glimore2009 [123], Kneiske2004 best-fit and low SFR [150]). It can be selected according to the user's preference. The software then compares the estimated spectrum with the sensitivity of the major IACTs: MAGIC, HESS and Veritas. The output of the program is available in root, pdf and ps format.

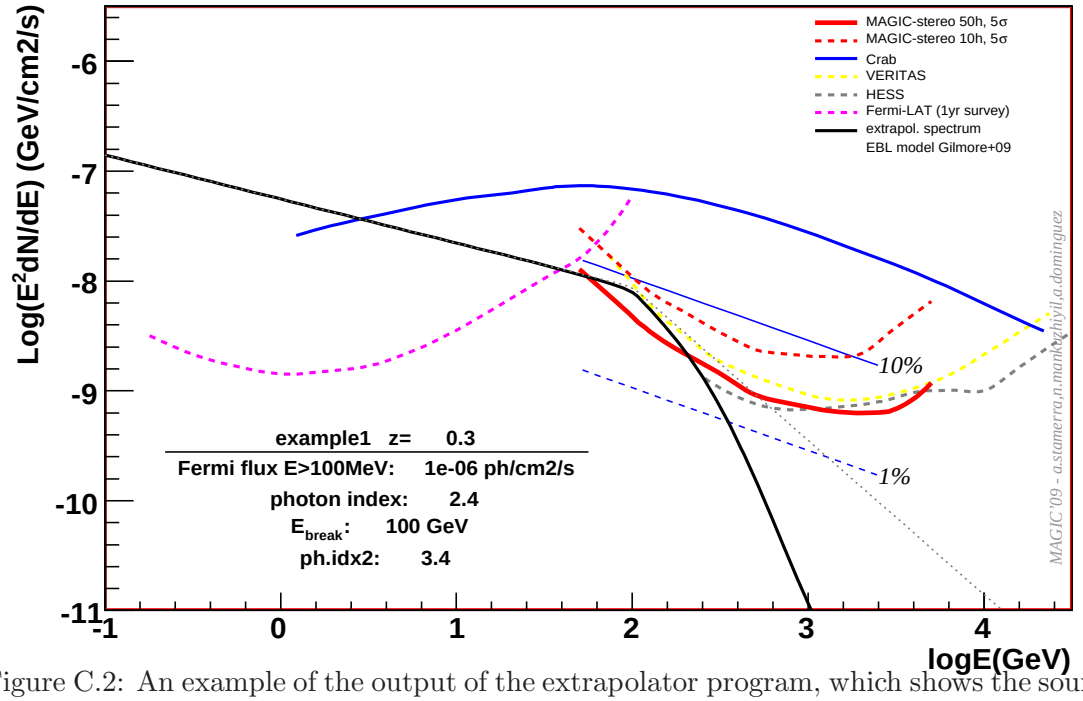

Figure C.2: An example of the output of the extrapolator program, which shows the source is observable in 50 hours with the MAGIC telescope in VHE range.

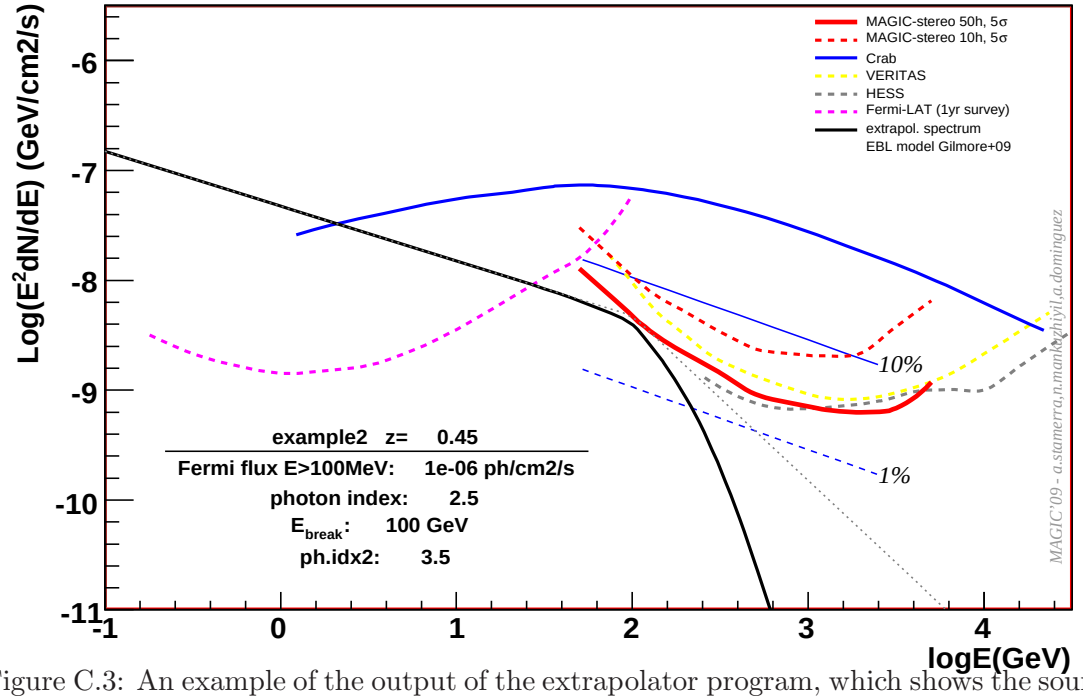

Figure C.3: An example of the output of the extrapolator program, which shows the source is not observable in 50 hours in VHE range with current sensitivity instruments.

Bibliography

[1] A. A. Abdo et al. (Fermi Coll.), Astrophys. J., 700, 597 (2009a)

[2] A. A. Abdo et al. (Fermi Coll.), Astrophys. J., 699, 817 (2009b)

[3] R. U. Abbasi et al. (HiRes Coll.), Phys. Rev. Lett., 100, 101101 (2008)

[4] J. Abraham et al. (Auger Coll.), Phys. Rev. Lett., 101, 061101 (2008a)

[5] J. Abraham et al. (Auger Coll.), Phys. Rev. Lett., 100, 211101 (2008b)

[6] V. Acciari et al. (VERITAS Coll.), Astrophys. J., 685, 73 (2008)

[7] V. Acciari et al. (VERITAS Coll., MAGIC coll.), Astrophys. J., 703, 169 (2009)

[8] V. Acciari et al. (VERITAS Coll.), Astrophys. J., 690, 126 (2009)

[9] F. Aharonian et al. (HEGRA Coll.), Astron. Astrophys., 349, 11 (1999)

[10] F. Aharonian et al. (HESS Coll.), Astron. Astrophys., 393, 89 (2002)

[11] F. Aharonian et al. (HESS Coll.), Astron. Astrophys., 421, 529 (2004a)

[12] F. Aharonian et al. (HESS Coll.), Astron. Astrophys., 425, 13 (2004b)

[13] F. Aharonian et al. (HESS Coll.), Astron. Astrophys., 436, 17 (2005a)

[14] F. Aharonian et al. (HESS coll.), Science, 309, 746 (2005b)

[15] F. Aharonian et al. (HESS Coll.), Aston. Astrophys, 442, 895 (2005c)

[16] F. Aharonian et al. (HESS Coll.), Astron. Astrophys., 449, 223 (2006a)

[17] F. Aharonian et al. (HESS Coll.), Astron. Astrophys., 457, 899 (2006b)

[18] F. Aharonian et al. (HESS Coll.), Nature, 440, 1018 (2006c)

[19] F. Aharonian et al. (HESS Coll.), Astron. Astrophys., 448, 19 (2006d)

[20] F. Aharonian et al. (HESS Coll.), Astron. Astrophys., 473, 25 (2007a)

[21] F. Aharonian et al. (HESS Coll.), Astophys. J., 664, 71 (2007b)

[22] F. Aharonian et al. (HESS Coll.), Astron. Astrophys., 475, 9 (2007c)

[23] F. Aharonian et al. (HESS Coll.), Astron. Astrophys., 470, 475 (2007d)

[24] F. Aharonian et al. (HESS Coll.), Astron. Astrophys., 481, 103 (2008a)

[25] F. Aharonian et al. (HESS Coll.), Astron. Astrophys., 477, 481 (2008b)

[26] F. Aharonian et al. (HESS Coll.), Astophys. J., 695, 40 (2009a)

[27] F. Aharonian et al. (HESS Coll.), Astophys. J., 696, 150 (2009b)

[28] F. Aharonian et al. (HESS Coll.), Aston. Astrophys., 502, 749 (2009c)

[29] J. Ahrens et al. (IceCube Coll.), Astropart. Phys., 20, 507 (2004)

[30] J. Albert et al. (MAGIC Coll.), Science, 312, 1771 (2006a)

[31] J. Albert et al. (MAGIC Coll.), Astrophys. J., 638, 101 (2006b)

[32] J. Albert et al. (MAGIC Coll.), Astrophys. J., 642, 119 (2006c)

[33] J. Albert et al. (MAGIC Coll.), Astrophys. J., 648, 105 (2006d)

[34] J. Albert et al. (MAGIC Coll.), Astron. Astrophys., 654, 119 (2007a)

[35] J. Albert et al. (MAGIC Coll.), Astrophys. J. L., 666, 17 (2007b)

[36] J. Albert et al. (MAGIC Coll.), Astrophys. J. L., 667, 21 (2007c)

[37] J. Albert et al. (MAGIC Coll.), Astrophys. J., 669, 862 (2007d)

[38] J. Albert et al. (MAGIC Coll.), Astron. Astrophys., 474, 937 (2007e)

[39] J. Albert et al. (MAGIC Coll.), Astrophys. J. , 667, 358 (2007f)

[40] J. Albert et al. (MAGIC Coll.), Science, 320, 1752 (2008a)

[41] J. Albert et al. (MAGIC Coll.), Nucl. Instr. and Math. in Phys. Res. A, 594, 407(2008)

[42] J. Albert et al. (MAGIC Coll.), Astrophys. J. L., 668, 253 (2008c)

[43] J. Albert et al. (MAGIC Coll.), Astron. Astrophys., 493, 467 (2009)

[44] J. Aleksic et al. (MAGIC Coll.), Astron. Astrophys., Submitted (2009)

[45] E. Aliu et al. (MAGIC Coll.), Science, 322, 1221 (2008)

[46] E. Aliu et al. (MAGIC Coll.), Astrophys. J., 692, 29 (2009)

[47] H. Anderhub et al. (MAGIC Coll.), Astron. Astrophys., 498, 83 (2009)

[48] H. Anderhub et al. (MAGIC Coll.), Astrophys. J., 705, 1624 (2009)

[49] H. Anderhub et al. (MAGIC Coll.), Astrophys. J. L. (submitted) (2009)

[50] T. Antoni et al. (Kascade Coll.), Astropart. Phys., 24, 1 (2005)

[51] M. G. Baring, Adv. Space Research, 33, 552 (2004)

[52] http://wwwmagic.mppmu.mpg.de/publications/proposals/ (Design report)

[53] M. Begelman, R. Blandford and M. J. Rees, Rev. Mod. Phys., 256, 255 (1984)

[54] M. Begelman, Astrophysics in Active Galaxies and Quasi-Stellar Objects, ed. J.S.Miller (University Science Books), p411 (1985)

[55] V. Berezinsky, Nucl. Phys. B, 188, 227 (2009)

[56] M. Bertero, Adv. in Electronic and Electron Phys., 75, 1 (1989)

[57] R. L. Biermann et al., Proc. 7eme Colloqium Cosmologie, High energy astrophysics from and for space arXiv:astro-ph/0211503 (2003)

[58] D. J. Bird et al., Astrophys. J., 424, 494 (1994)

[59] R. D. Blandford and A. Konigl, Astrophys. J., 232, 34 (1979)

[60] R. D. Blandford and D. G. Payne, Mon. Not. R. Astron. Soc., 199, 883 (1982)

[61] R. D. Blandford, Active Galactic Nucle, ed. J.E. Dayson (Machester Univ. Press), 281 (1985)

[62] R. D. Blandford and R. L Znajek, Mon. Not. R. Astron. Soc., 179, 433 (1977)

[63] R. D. Blandford and M. J. Rees Publ. Astron. Soc., Pac. 54, 23 (1991)

[64] R. D. Blandford, Publ. Astron. Soc. Pac., 160, 265 (1999)

[65] A.W. Blain and T.G.Phillips, Mon. Not. R. Astron. Soc. 333, 222 (2002)

[66] M. Blazejowski et al. Astrophys. J., 630, 130 (2005)

[67] M. Blazejowski et al. Astrophys. J., 545, 107 (2000)

[68] P. Bhattacharjee, Phys. Rep., 327, 109 (2000)

[69] M. Böttcher, PhD thesis, Universitat Bonn (1997)

[70] T. Bretz, D. Dorner, D. Hone, Proc. of ICRC, 4, 311 (2005)

[71] V.S. Brezinsky and S.I. Gregor'eva, Astron. Astrophys.,199,1 (1988)

[72] J. Buckley et al. (Whipple Coll.), Astrophys. J., 472, 9 (1996)

[73] M. Catanese et al. (Whipple Coll.) Astrophys. J., 487, 143 (1997)

[74] M. Catanese et al. (Whipple Coll.), Astrophys. J., 501, 616 (1998)

[75] P. M. Chadwick et al. (Univ. of Durham Mark 6 Gamma Ray Telescope Coll.), Astrophys. J., 513, 161 (1999)

[76] A. Chen. et al., The Astronomer's Telegram, 1278, 1 (2007)

[77] P. Cherenkov, Dokl. Akad. Nauk, SSSR, 2, 451 (1934)

[78] E. Costa et al. (Bepposax coll.), Nature, 387, 783 (1997)

[79] L. Costamante and G. Ghisellini, Astron. Astrophys., 384, 56 (2002)

[80] G. Cusumano et al., To be published in Astron. Astroph. [arXiv:0906.4788] (2010)

[81] A. Dar and A. Laor, Astrophys. J., 478,5 (1997)

[82] J. K. Daughetry and A. K. Harding, Astrophys. J., 252,337 (1982)

[83] C. D. Dermer, Invited talk at 30 th ICRC (arXiv:0711.2804) (2007)

[84] C. D. Dermer and A. Schlickeiser, Astrophys. J., 416, 458 (1993)

[85] A. Dolcini et al., Astron. Astrophys., 443, 33 (2005)

[86] I. Donnarumma et al., Astrophys. J.,691,13 (2009)

[87] M. Dopita, Publ. Astron. Soc. of Australia. 14, 230 (1997)

[88] D. Dorner et al., Proc. 29th ICRC, 5, 175 (2005)

[89] D. Dorner, PhD thesis, Universitat W*ü*rzburg (2008)

[90] D. Dorner et al., Astron. Astrophys. arxiv:0808.0279 (2009)

[91] www.mpi-hd.mpg.de/hfm/HESS/pages/press/old/PressRelease/EBLPress/

[92] R. Engel, D.Seckel and T. Satnev, Phys. Rev. D, 64, 09310 (2001)

[93] A. D. Erlykin and A. W. Wolfendale, Astropart. Phys., 22, 47 (2004)

[94] B. L. Fanaroff and J. M. Riley Mon. Not. R. Astron. Soc., 167, 31 (1974)

[95] G.J.Ferland et al., PASP, 110,761 (1998)

[96] R. Falomo and A. Treves, PASP , 102, 1120 (1990)

[97] E. A. Fath, Lick Observatory Bulletin, 5, 71 (1909)

[98] J. D. Finke, C. D. Dermer, M. B*ö*ttcher, Astrophys. J., 686, 181 (2008)

[99] J.D. Finke and S. Razzaque, ApJ, 698, 1761 (2009)

[100] A. V. Filippenko and J. P. Halpern, Astrophys. J., 285, 458 (1984)

[101] A. V. Filippenko and R. Terlevich, Astrophys. J., 397, 79 (1992)

[102] D. J. Fixsen et al. Astropjys. J., 299, 433 (1998)

[103] G. Fossati et al, Mon. Not. R. Astron. Soc., 677, 906 (2008)

[104] G. Fossati et al. Astropjys. J., 508, 123 (1998)

[105] I. Frank and I. Tamm, Dokl. Akad. Nauk, SSSR, 14, 109 (1937)

[106] A. Francescini et al. AIP Conf. Proc. 348, 159 (1996)

[107] A. Franceschini, A. Rodighiero and M. Vaccari, Astron. Astrophys., 487, 837 (2008)

[108] J. A. Gaidos et al., Nature, 383, 319 (1998)

[109] D. Gall, Proc. of the Fermi Symposium, Washington (2009)

[110] M. Gaug, PhD Thesis, Univ. Astronoma de Barcelona (2006)

[111] M. Garczarczyk et al. Proc. of 29 th ICRC (2005)

[112] T. K. Gaisser and T. Stanev, Cosmic rays, Particle Data Group (2009)

[113] W.K. Gear, et al., Mon. Not. R. Astron. Soc, 267, 167 (1994)

[114] M. Georganopulos, J. Finke and L. Reyes, Proc. Fermi Sympossium, Washington DC (2009)

[115] A. Ghez et al., Astrophys. J., 586, 127 (2003)

[116] G. Ghisellini and P. Madau, Mon. Not. R. Astron. Soc., 208, 67 (1996)

[117] G. Ghisellini et al., Mon. Not. R. Astron. Soc., 301, 451 (1998)

[118] G.Ghisellini et al., Mon. Not. R. Astron. Soc, 382, 82 (2007)

[119] G. Ghisellini et al., Mon. Not. R. Astron. Soc., 393, 16 (2009)

[120] G. Ghisellini et al., Mon. Not. R. Astron. Soc., 402, 497 (2010)

[121] R. Giacconi, Phys. Rev. Lett., 9, 439 (1962)

[122] M. Giller, Astron. Astrophys., 449, 223 (2006)

[123] R.C Gilmore 2009, Mon. Not. R. Astron. Soc. , 399, 1694 (2009)

[124] P. Giommi et al. (BeppoSAX Coll.), www.asdc.asi.it/blazars/ (2002)

[125] P. Giommi et al., Astron. Astrophys., 456, 911 (2006)

[126] M. Gliozzi et al., Astrophys. J., 646, 61 (2006)

[127] F. Goebel et al., Proc. of ICRC, 5, 179 (2005)

[128] F. Goebel et al., Proc. of ICRC, 3, 1481 (2007)

[129] P. Gorham et al. (Anita Coll.), Phys. Rev. Lett., 103, 051103 (2009)

[130] K. Greisen, Phys. Rev. Lett., 16, 748 (1966)

[131] J. L. Greenstein and M.Schmidt, Astrophys. J., 140, 1 (1964)

[132] L. Greenhill et al. , Astron. Astrophys., 304, 21 (1995)

[133] D. Hadasch et al. (MAGIC collaboration), Proc. of 31 st ICRC, Poland (2009)

[134] F. Halzen, Science, 315, 66 (2007)

[135] R. C. Hartman et al. (EGRET Coll.), Astrophys. J. Suppl. Ser., 123, 79 (1999)

[136] N. Hayashida et al., Astrophys. J., 504, 71 (2000)

[137] N. Hayashida et al. (AGASA Coll.), Astrophys. J., 120, 2190 (2000)

[138] A.M.Hillas, Proc. 19 th ICRC, 3, 445 (1985)

[139] M.G. Hauser and E. Dwek, Annu. Rev. Astron. Astrophys, 39, 249 (2001)

[140] W. Heitler, The Quantum Theory Of Radiation", Oxford University Press (1960)

[141] D. Horan et al. (Whipple Coll.), Astrophys. J., 695, 596 (2009)

[142] D. Horan et al. (Whipple Coll.), Astrophys. J., 571, 753 (2002)

[143] E. P. Hubble, Astrophys. J., 64, 321 (1926)

[144] C.D. Impey and G. Neugebauer, Astron. J., 95, 307 (1988)

[145] Z. Ivezić at al. Astron. J., 124, 2364 (2002)

[146] K. G. Jansky, Nature, 132, 66 (1933)

[147] K. Katarzynski, H. Sol and A. Kus, Astron. Astrophys.,367, 809 (2001)

[148] R. C. Kennicut, Annu. Rev. Astron. Astrophys., 36, 189 (1998)

[149] T.M. Kneiske, K. Mannheim and D. H. Hartman, Astron. Astrophys., 386, 1 (2002)

[150] T.M. Kneiske et al., Astron. Astrophys., 413, 807 (2004)

[151] H. Kuehr et al, Astron. J., 86, 854 (1981)

[152] M. Kino, F. Takahara and M. Kusunose Astrophys. J., 509, 608 (2001)

[153] A. Koratkar et al. Astrophys. J., 492, 173 (1998)

[154] K. Kosack and VERITAS Coll. Bull. Am. Astron. Soc., 36, 927 (2004)

[155] H. Krawczynski et al. Astrophys. J., 601, 151 (2004)

[156] I. Kravchenko et al. (RICE collaboration), Phys. Rev. D, 73, 082002 (2006)

[157] W. L. Kraushaar et al. Astrophys. J., 177, 341 (1972)

[158] R. Landau et al., Astrophys. J., 308, 78 (1986)

[159] A. M. Levine et al., Astrophys. J., 469, 33 (1996)

[160] T.P. Li and Y.Q. Ma, Analysis methods for results in gamma-ray astronomy., 272, 317 (1983)

[161] E. Lindfors et al. (MAGIC collab.), Proc. of 31 st ICRC (arXiv:0907.0550) (2009)

[162] A. P. Lobanov et al., Astron. Astrophys., 364, 391 (2000)

[163] B. Lott, Proc. Fermi Symposium, Washington D.C. (2009)

[164] K. Mannheim, Astron. Astrophys., 269, 67 (1993)

[165] N. Mankuzhiyil, M. Persic and F. Tavecchio Astrophys. J. Lett., 715, 16 (2010)

[166] H.L. Marshall et al., Astrophys. J., 156, 13 (2005)

[167] L. Maraschi, G. Ghisellini and A. Celotti, Astrophys. J., 397, 5 (1992)

[168] L. Maraschi and F. Tavecchio Astrophys. J., 593, 667 (2003)

[169] M. Matsuoka et al. (MAXI Collab.) Astron. Soc. Japan (to be published) arXv:0906.0631 (2010)

[170] T. Matusmoto, The Institute of Space and Astronomical Science Report No.14, 179, 14 (2000)

[171] T. A. Matthews and A. R. Sadage Astrophys. J., 138, 30 (1963)

[172] D. Mazin and F. Goebel, Astrophys. J. Lett., 655, 13 (2007)

[173] D. Mazin and F. Goebel, Astrophys. J. Lett., 655, 13 (2006)

[174] D. Mazin and M. Raue, Astron. Astrophys., 471, 439 (2007)

[175] I. F. Mirabel and L. F. Rodriguez, Nature, 371, 46 (1994)

[176] R. Moderski et al., Mon. Not. R. Astron. Soc. 363, 954 (2005)

[177] D. Monet et al. 1998, The PMM USNO-A2.0 Catalog (http://adsabs.harvard.edu/abs/1998USNO2.C.....0M)

[178] M. Catanese et al. (Whipple Coll.) Astrophys. J., 487, 143 (1997)

[179] T. Nishiyama et al. (Utah Seven Telescope Array Coll.) Proc. of the 26 th ICRC, 3, 370 (1999)

[180] P. Padovani, Astrophysics and Space Science, 309, 63 (2007)

[181] D. Paneque et al. Nucl. Inst. and Meth. 504, 109 (2003)

[182] D. Paneque, PhD Thesis, Technical University, Munchen (2004)

[183] A. A. Penzias and R. W. Wilson, Astrophys. J., 142, 419 (1965)

[184] E. Pian et al. Astrophys. J., 521, 112 (1999)

[185] E. Pian. et al., Astron. Astrophys., 429, 427 (2005)

[186] E. Pian. et al., Astron. Astrophys. , 449, 21 (2006)

[187] T. A. Porter et al. Astrophys. J., 648, 29 (2006)

[188] C. Pittori et al. (AGILE Coll.), Astron. Astrophys. ,506, 1563 (2009)

[189] W. H. Press et al., Numerical recipes in C, second edition, Cambridge university press (1993)

[190] M. Punch et al. (Whipple Coll.), Nature, 358, 477 (1992)

[191] J. Quinn et al. (Whipple Coll.), Astrophys. J. L., 456, 83 (1966)

[192] B. Punsly and F. V. Coroniti, Astrophys. J., 350, 518 (1990)

[193] M. Raue and D. Mazin, Int. J. Mod. Phys. D., 17, 1515 (2008)

[194] S. Razzaque, C.D Dermer and J.D. Finke Astrophys. J.,697, 483 (2009)

[195] P. Rebillot et al., Astrophys. J.,641, 740 (2006)

[196] M. Rees and P. Mezaros, Mon. Not. R. Astron. Soc., 251, 48 (1992)

[197] A. Reimer, Astropphys. J., 665, 1023 (2007)

[198] B. Rocca-Volmerange and M. Fioc, AIP Conf. Proc. 348, 132 (1996)

[199] W.A. Rolke., A.M. López, and J.Conrad, Nucl. Instrum. and Meth., A551, 493 (2005)

[200] http://root.cern.ch

[201] E. E. Salpeter, Astrophys. J., 140, 796 (1964)

[202] R. M. Sambruna et al. Astrophys. J., 463, 444 (1996)

[203] R. M. Sambruna et al. Astrophys. J., 652, 146 (2006)

[204] R. M. Sambruna et al. Astrophys. J., 669, 884 (2007)

[205] B. Sbarufatti. et al., Astrophys. J., 132, 1 (2006)

[206] M. Schmelling et al., Nucl. Instrum. Methods, 340, 400 (1994)

[207] P.S. Smith et al., Astrophys. J., 326, 39 (1988)

[208] D. J. Schlegel Astrophys. J., 500, 525 (1998)

[209] M. Schroedter et al., Astrophys. J., 634, 947 (2005)

[210] D. A. schwartz et al., Astrophys. J., 229, 53 (1979)

[211] A. J. Shmmins and J. G. Bolton, Australian journal of Physics suppliment 32, 1 (1974)

[212] R.S. Somerville and J.S. Primack, Mon. Not. R. Astron. Soc., 310, 1087 (1999)

[213] L. G. Sveshnikova, Astron. Astrophys., 409, 799 (2003)

[214] M. Sikora, M. C. Begelman and M. J. Rees, Astron. Astrophys., 421, 153 (1994)

[215] S. M. Simkin, H. J. Su and M. P. Schwarz, Astrophys. J., 237, 404 (1980)

[216] G. Sinnis, New J. Phys., 11, 34 (2009)

[217] H. J. Smith and D. Hoffleit, Nature, 198, 650 (1963)

[218] F. W. Stecker, O. C. de Jager and M. H. Salamon Astrophys. J., 390, 49 (1992)

[219] F. W. Stecker, M. A. Malkan and S. T. Scully, Astrophys. J., 648, 774 (2006)

[220] J.A. Stevens et al., Astrophys. J, 437, 91 (1994)

[221] G. Superina et al. (HESS coll.), Proc.of 30 th ICRC, 3, 913 (2007)

[222] M. Takeda et al. (AGASA coll.), Astropart. Phys., 19, 447 (2003)

[223] A. P. S. Tang et al., Astrophys. J., 676, 562 (2008)

[224] F. Tavecchio, L. Maraschi and G. Ghisellini., Astrophys. J., 509, 608 (1998)

[225] F. Tavecchio et al., Astrophys. J., 554, 725 (2001)

[226] F. Tavecchio et al., Astrophys. J., 575, 137 (2002)

[227] F. Tavecchio et al., Astrophys. J., 662, 900 (2007)

[228] F. Tavecchio, G. Ghisellini, Mon. Not. R. Astron. Soc., 386, 945 (2008)

[229] A.N. Tikhonov and V. J. Arsenin, Methods of Solution of III-posed Problems - M.Nauka (1979)

[230] A. Treves et al., Astron. Astrophys., 473, 17 (2007)

[231] K. Tsuchiya et al. (CANGAROO Coll.), Astrophys. J. Lett., 606, 115 (2004)

[232] C. M. Urry and P. Padovani, Publ. Astron. Soc. Pac., 107, 83 (1995)

[233] M. J. Valtonen et al., Nature, 452, 851 (2008)

[234] D. Varies et al Astron. J., 129, 615 (2005)

[235] S. Vercellone., et al, Astrophys. J., 676, 13 (2008)

[236] M. Villata et al. Astron. Astrophys. Supp. Ser. , 130, 305 (1998)

[237] M. Villata et al., Astron. Astrophys., 453, 817 (2006)

[238] W. Voges et al. (ROSAT Coll.), Astron. Astrophys., 349, 389 (1999)

[239] R.M. Wagner, PhD thesis, Max-Plank institute for Physics (2006)

[240] S. J. Wagner, HEAD conference, Hawai (2010)

[241] E. Waxman and J.Bahcall, Phys. Rev. D, 59, 023002 (1999)

[242] http://www.mpp.mpg.de/ rwagner/sources

[243] T. Weekes et al. (VERITAS Coll.), Astrophys. J., 342, 375 (1989)

[244] T. Weekes et al. (VERITAS Coll.), Astropart. Phys., 17, 221 (2002)

[245] A. S. Wilson and E. J. M. Colbert, Astrophys. J., 438, 62 (1995)

[246] D.M. Worrall and B.J. Wilkes. Astrophys. J., 360, 396 (1990)

[247] http://vega.bac.pku.edu.cn/ wuxb/agn/text.html

[248] W. M. Yao et al., J. Phys. G, 33, 1 (2006)

[249] G. T. Zatsepin and V. A. Kuzmin, JETP Lett., 4, 78 (1966)

[250] S. Zhang, W. Collamar and S. Schonfelder, Astron. Astrophys., 444, 767 (2005)